TU Delft

Delft University of Technology

Infrasonic Interferometry

Probing the atmosphere with acoustic noise from the oceans

Fricke, Julius

DOI
10.4233/uuid:6d23ede7-8f1f-494e-930c-e2ecc6546160

Publication date
2016

Document Version
Final published version

Citation (APA)
Fricke, J. (2016). *Infrasonic Interferometry: Probing the atmosphere with acoustic noise from the oceans*. [Dissertation (TU Delft), Delft University of Technology]. https://doi.org/10.4233/uuid:6d23ede7-8f1f-494e-930c-e2ecc6546160

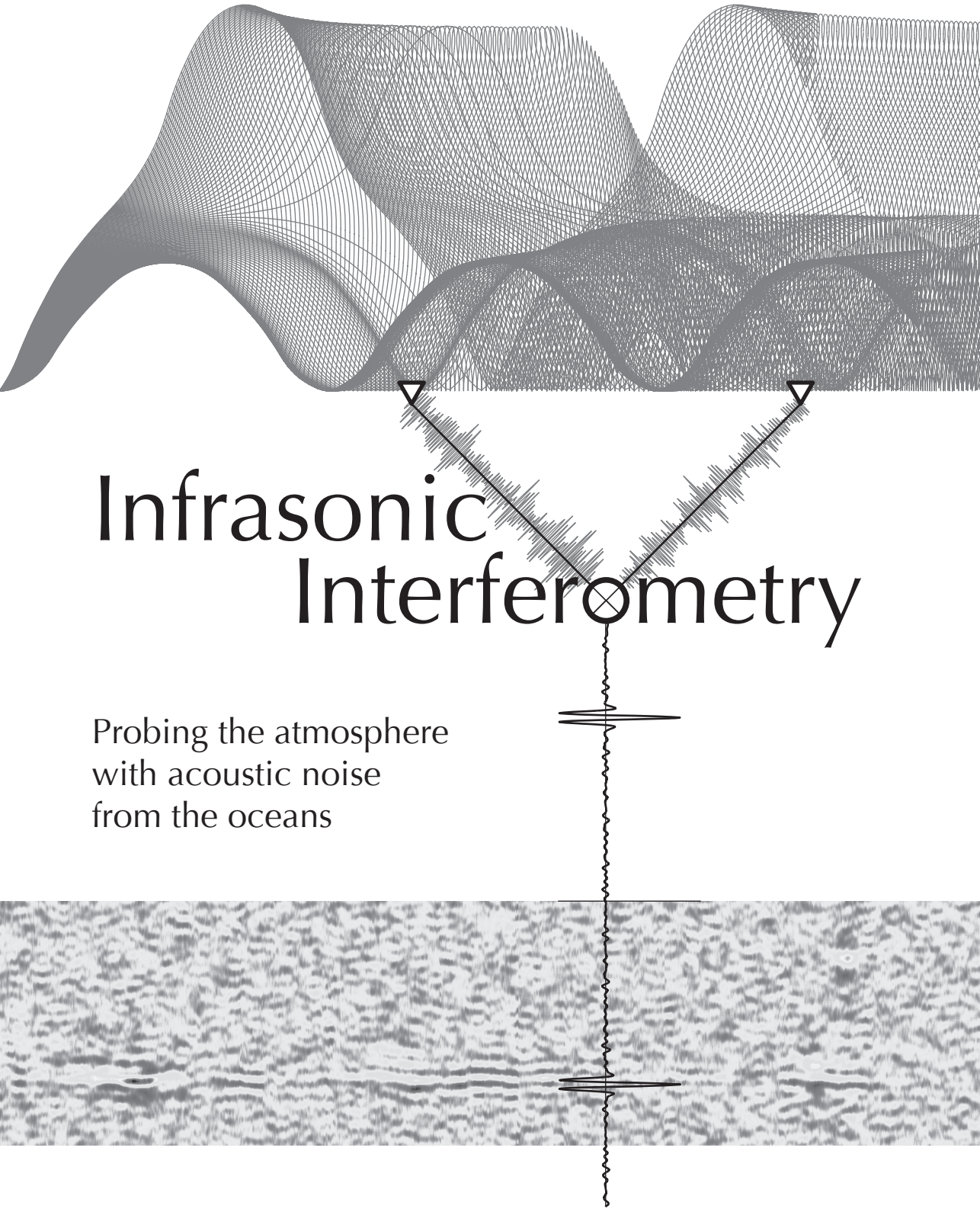
Important note
To cite this publication, please use the final published version (if applicable).
Please check the document version above.

Copyright
Other than for strictly personal use, it is not permitted to download, forward or distribute the text or part of it, without the consent of the author(s) and/or copyright holder(s), unless the work is under an open content license such as Creative Commons.

Takedown policy
Please contact us and provide details if you believe this document breaches copyrights.
We will remove access to the work immediately and investigate your claim.

This work is downloaded from Delft University of Technology.
For technical reasons the number of authors shown on this cover page is limited to a maximum of 10.

Julius T. Fricke



Infrasonic Interferometry

Probing the atmosphere with acoustic noise from the oceans

Infrasonic Interferometry

Probing the atmosphere with acoustic noise from the oceans

Infrasonic Interferometry

Probing the atmosphere with acoustic noise from the oceans

Proefschrift

ter verkrijging van de graad van doctor
aan de Technische Universiteit Delft,
op gezag van de Rector Magnificus prof. ir. K. C. A. M. Luyben,
voorzitter van het College voor Promoties,
in het openbaar te verdedigen op

door

Julius Tobias Fricke

Diplom–Ingenieur der Medientechnologie Technische Universität Ilmenau,
Deutschland
geboren te Lemgo, Duitsland.

Dit proefschrift is goedgekeurd door de promotoren:

Prof. dr. D. G. Simons
Prof. dr. ir. C. P. A. Wapenaar
Prof. dr. L. G. Evers

Samenstelling promotiecommissie:

Rector Magnificus,	voorzitter
Prof. dr. D. G. Simons,	Technische Universiteit Delft, promotor
Prof. dr. ir. C. P. A. Wapenaar,	Technische Universiteit Delft, promotor
Prof. dr. L. G. Evers,	Technische Universiteit Delft, promotor

Onafhankelijke leden:

Prof. dr. ir. H. W. J. Russchenberg,	Technische Universiteit Delft
Prof. dr. L. L. A. Vermeersen,	Technische Universiteit Delft
Prof. dr. L. Ottemøller,	University of Bergen, Norway
Dr. D. N. Green,	Atomic Weapons Establishment Blacknest, UK





Royal Netherlands
Meteorological Institute
Ministry of Infrastructure and the Environment



Printed by: Ridderprint BV

Front & Back: Julius T. Fricke

Copyright © 2016 by J. T. Fricke

ISBN 978-94-6186-736-0

An electronic version of this dissertation is available at
`http://repository.tudelft.nl/`.

Contents

1 Introduction **1**
- 1.1 Infrasound and atmosphere . . . 1
- 1.2 Infrasound as atmospheric probe . . . 4
- 1.3 Application of a new interferometric technique . . . 5
- 1.4 Structure of the thesis . . . 9

2 Theory **11**
- 2.1 Modeling of the infrasound propagation . . . 11
  - 2.1.1 From the general wave equation to the ray path . . . 11
  - 2.1.2 Attenuation of Infrasound . . . 18
- 2.2 Infrasonic Interferometry . . . 25
  - 2.2.1 Interferometry general . . . 25
  - 2.2.2 Interferometry in a moving medium: Nonreciprocal Green's function . . . 33

3 Infrasonic Interferometry of Stratospherically Refracted Microbaroms – A Numerical Study **41**
- 3.1 Introduction . . . 42
- 3.2 Infrasonic Interferometry . . . 43
- 3.3 Modeling of the Infrasound Propagation . . . 46
- 3.4 Numerical Experiments . . . 49
  - 3.4.1 Numerical Experiment with Blast Waves . . . 51
  - 3.4.2 Numerical Experiment with Microbaroms . . . 53
- 3.5 Conclusions . . . 56
- 3.6 Acknowledgments . . . 59

4 Infrasonic interferometry applied to microbaroms observed at LAIA in the Netherlands 61
4.1 Introduction . . . 62
4.2 The Large Aperture Infrasound Array . . . 64
4.3 Processing of Microbaroms and Crosscorrelations . . . 66
4.4 State of the Atmosphere and Microbarom Sources . . . 69
4.4.1 Atmospheric Conditions . . . 69
4.4.2 Microbarom Sources . . . 69
4.5 Retrieving Parameters of Infrasound Propagation and the Atmosphere 72
4.5.1 Crosscorrelation and Coherence as a Function of Distance . . 72
4.5.2 Crosscorrelation and Atmospheric Variability as a Function of Time . . . 76
4.6 Conclusions . . . 81
4.7 Acknowledgments . . . 81
4.8 Supplemental material . . . 82

5 Interferometry applied to stratospherically refracted microbaroms 87
5.1 Introduction . . . 87
5.2 Recordings of the Alaskan deployment of the USArray . . . 87
5.3 Results of the crosscorrelations . . . 91
5.3.1 Crosscorrelations of tropospherically propagating microbaroms 91
5.3.2 Crosscorrelations of stratospherically propagating microbaroms 99
5.4 Discussion . . . 113
5.4.1 Tropospheric crosscorrelations . . . 113
5.4.2 Stratospheric crosscorrelations . . . 115
5.5 Conclusions . . . 116

6 Conclusions and outlook 119
6.1 Conclusions . . . 119
6.1.1 Introduction . . . 119
6.1.2 Conclusions from Chapter 2 . . . 119
6.1.3 Conclusions from Chapter 3 on the feasibility . . . 120
6.1.4 Conclusions from Chapter 4 on the tropospheric application . 120
6.1.5 Conclusions from Chapter 5 on the stratospheric application 121
6.2 Outlook . . . 122
6.2.1 Improvement of the signal–to–noise–ratio . . . 122
6.2.2 Tropospheric applications of infrasonic interferometry . . . 123

A List of Symbols and Abbreviations 125
A.1 Symbols . . . 125
A.2 Abbreviations . . . 130

B Appendix Absorption 131

Bibliography 137

Summary **147**

Samenvatting **151**

Zusammenfassung **155**

Curriculum Vitæ **159**

Acknowledgements **163**

1

Introduction

1.1 Infrasound and atmosphere

Imagine a world full of sounds you are not able hear. There is a rich world of sounds humans cannot hear below a frequency of 20 Hz. It is called infrasound. The frequencies of infrasound usually reach down to the acoustic cut–off frequency, $N_A = 3.3\,\mathrm{mHz}$. The frequency range of infrasound is shown in Figure 1.1.

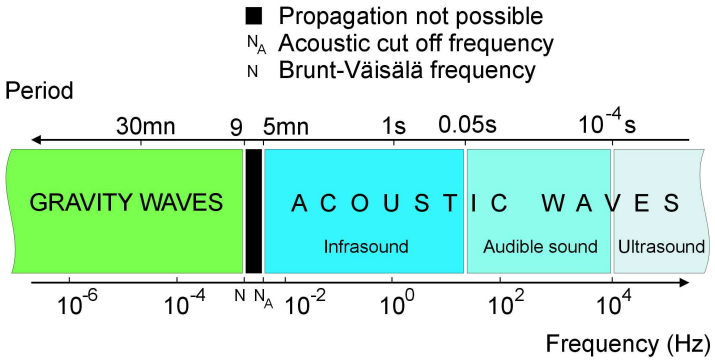


Figure 1.1: *The audible sound has a frequency range from 20 Hz up to 20 kHz. The inaudible sound below 20 Hz is called infrasound.*

Although infrasound cannot be heard, it can be measured. The first time infrasound was recorded was in 1883. The volcano Krakatoa in Indonesia had erupted and the explosion caused air waves which traveled around the world several times with the speed of sound. On their journey, they were recorded by 53 barographs around the world [*Symons*, 1888]. To measure small pressure fluctuations of low frequencies *Shaw and Dines* [1904] developed and deployed the more sensitive microbarograph. These microbarographs in UK measured a large infrasonic wave, which was caused by the Siberian Tunguska meteor in 1908 [*Whipple*, 1930].

These early examples of infrasound measurements show, that infrasound propagates very far through the atmosphere, much further than audible sound. Due to its low frequencies, infrasound is much less attenuated by the atmosphere than audible sound, since the attenuation by absorption decreases with the square of the frequency [*Sutherland and Bass*, 2004]. The low absorption allows infrasound to propagate over distances of hundreds to thousands of kilometers.

On the one hand infrasound can be measured at distances of hundreds to thousands of kilometers, but on the other hand it often seems to disappear closer to the sources. On which paths does it reach the distant locations, while it seems to skip other locations in between? Nowadays, these so called shadow zones are well known, but in the early 1900's, this behavior asked the question: how does infrasound propagate?

The study of sound propagation through the atmosphere began with audible sounds. *Reynolds* [1873] found patterns in the propagation of sound depending on the wind. As sound sources he used bells, pistol shots and rockets, which either were audible at certain locations or not [*Reynolds*, 1873, 1876]. A propagation pattern observed by Reynolds is shown in Figure 1.2. Reynolds concluded that the sound is refracted upwards against the wind or if the temperature decreases with altitude. He also observed that the sound refracted downward by temperature increases with altitude.

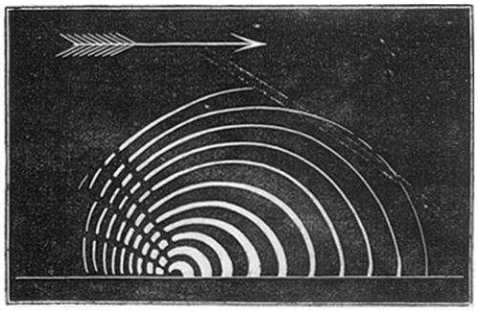


Figure 1.2: *Propagation of audible sound through the atmosphere observed by Reynolds [1873]. The arrow indicates the wind direction (source: Reynolds [1873]).*

All of Reynolds experiments took place in the lowest layer of the atmosphere: the troposphere. Several years later, *Lindemann and Dobson* [1923] discovered that the temperature above 60 km is higher than it had been expected before. *Whipple* [1923] realized that the higher temperature leads to a higher sound speed in the upper atmosphere, which has consequences for the propagation path of sound back to the ground. Whipple concluded that a higher sound speed in the upper atmosphere can cause the refraction of sound. The refractions gave a possible explanation of the shadow zones in which the sound cannot be heard or measured. Whipple's explanation of the sound propagation in the stratosphere was confirmed by studies of *Gutenberg* [1939]. Gutenberg observed the sound propagation of navy gun fires offshore southern California. Next to the zones in which the sound was audible he also found the shadow zones. By the travel times of the sound in the zones of audibility he concluded that the sound was refracted in the stratosphere. It still took a few years before this hypothesis was proven. Figure 1.3 shows an example of sound propagation north and southwards through the atmosphere, simulated by a raytracer. The corresponding sound speed profiles depend on temperature and wind and are shown on the left and on the right. The direction in which the sound is emitted is described by the elevation angle (see color bar).

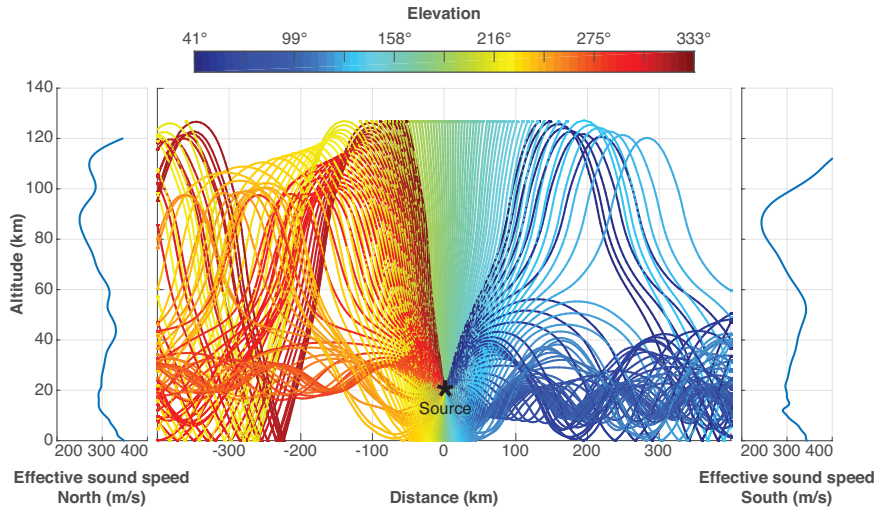


Figure 1.3: *The sound propagation north and southwards through the atmosphere, simulated by a raytracer. The corresponding sound speed profiles depend on temperature and wind and are shown on the left and on the right. The elevation angle will be defined in Chapter 2 (cf. Figure 2.3).*

In the cold war, a new kind of infrasonic events occurred caused by the atmospheric nuclear tests. The nuclear tests moved the focus of the research to the propagation of low frequent waves like infrasound and gravity waves. In this era, the research of infrasound was mainly directed on the monitoring and the localization of the nuclear tests [*Hedlin et al.*, 2002]. For these purposes, the understanding and modeling of the atmospheric infrasound propagation was essential.

The ability to monitor atmospheric nuclear tests became even more important, when the Partial Test Ban Treaty (PTBT) was signed by the Soviet Union, the United Kingdom, and the United States in 1963. The PTBT banned all nuclear tests in the atmosphere, oceans and space, but did not make use of infrasound technology. Plans for an infrasonic monitoring network existed, but they were never realized [*Bedard and Georges*, 2000].

This changed 30 years later, when infrasound was chosen as a verification technique for the Comprehensive Nuclear–Test–Ban Treaty (CTBT), in 1996. Ever since, the study of infrasound has experienced a renaissance [*Dahlman et al.*, 2009]. The world-wide "International Monitoring System" (IMS) was installed to verify the CTBT. Next to other techniques the IMS includes 60 infrasound stations. Each infrasound station consist of four to eight microbarometers, i.e., an array. By putting the records of several microbarometers of an array in relation to each other, the arrival direction of infrasound can be determined. Using the direction of arrival (DOA) and the temperature and wind structure of the atmosphere, the propagation path of the sound can be traced back to its source. This tracing of sound waves is called ray tracing. *Kornhauser* [1953] published the first acoustic ray equations to calculate the ray path in a two–dimensional moving medium [*Havelock et al.*, 2008]. The ray equations were extended by *Thompson* [1972] for a three–dimensional moving medium. *Georges* [1972] implemented the ray equations in a computer program to trace the propagation of atmospheric gravity waves.

1.2 Infrasound as atmospheric probe

Already the first studies of acoustic propagation in the atmosphere showed the strong dependency on the temperature and wind structure of the atmosphere. Infrasound propagates over distances of hundred to thousand kilometers and each crossed atmospheric layer leaves a certain signature in the infrasonic signal. If this signature can be extracted in an inversion process, the temperature and wind structure of the atmosphere might be revealed.

Most of the current knowledge about the stratosphere is obtained from models. Infrasound offers the opportunity to gain advanced information about this atmospheric layer. Infrasound recordings carry this information in frequency, amplitude, phase, and travel time. Nuclear explosions, other explosions, meteors etc. cause infrasonic blasts, which can be measured as deterministic transient signals (DTS). These DTS may be used to probe the atmosphere.

Also *Gutenberg* [1939] used DTS to probe the atmosphere, when he tried to find a reasonable propagation path of the sound waves and assumed an increased temperature at 30 km to 40 km height with infrasound from navy guns.

Donn and Shaw [1967] suggested to explore the atmospheric wind and temperature structure with the recorded infrasonic waves of nuclear explosions by adopting the methods known from seismology.

This source of infrasound diminished, when the PTBT was signed and except for a few researchers in Australia, Sweden, the US, the Netherlands and France the research in this field stopped [*Haak and Evers*, 2002].

When infrasound was chosen as one of the verification techniques for the CTBT in 1996, more continuous infrasonic recordings became available. Remote sensing of the atmosphere by using theses data became one of the scientific challenges.

Le Pichon et al. [2005] analyzed the recordings of the IMS station IS22 situated 650 km southwards from the Lopevi volcano. The fine-scale wind fluctuations of the upper stratospheric and mesosphere were probed by using the continuous infrasound observations of the volcanic activities. Two years later, *Antier et al.* [2007] used the recordings of the same IMS station, to investigate the infrasonic signals from the Yasur volcano. In the study it became possible to probe the small temporal wind fluctuations from the ground to the stratosphere.

In numerical experiments, *Drob et al.* [2010] and *Lalande et al.* [2012] improved the knowledge about the inversion process by using Empirical Orthogonal Functions (EOF) of the wind structure. A raytracer was used to calculate simulated travel times for several possible combinations of EOF. By comparing the simulated with the known travel time the most likely combinations of EOFs were determined. These best fitting combination of EOF defines the retrieved wind profiles.

Assink et al. [2012] focused on the inversion of infrasound recordings from the Tungurahua volcano in Ecuador. The study showed that the wind in the upper atmosphere can be probed with the impulsive infrasonic waves of the volcano. In the following study of *Assink et al.* [2013] the inversion was improved by using EOF as mentioned before and showed the uncertainties of this approach.

Also studies of our research group were able to confirm the potential of infrasound as a remote sensing technique. By studying infrasound propagation of explosions and ambient noise during a sudden stratospheric warming in 2009, the drastic temperature and wind variations in the stratosphere and thermosphere were probed [*Evers and Siegmund*, 2009; *Evers et al.*, 2012].

Next to temperature and wind, also other atmospheric inhomogeneities in the atmosphere leave their signature in the infrasound signals. *Drob et al.* [2013] explained frequently observed infrasound signal variations by small-scale atmospheric fluctuations due to gravity waves.

Marcillo and Johnson [2010] deployed infrasound as a remote sensing technique of the troposphere by determining the wind vector with three infrasound sensors in the near-field of a volcano.

1.3 Application of a new interferometric technique

All the previously described studies impressively proved the possibilities of infrasonic DTS as remote-sensing techniques for the atmosphere, but DTS have crucial disadvantages. For instance explosive events, which cause a DTS are rare. There

are no explosions, volcanic eruptions, or meteor impacts every day. Furthermore it is difficult to predict such sources, because usually it is unknown, when and where an explosion will occur. Even if the exact position of an erupting volcano is known, the exact time of the eruption is hard to predict. Another disadvantage lies in the nature of impulsive signals like DTS. Impulses have only a very short duration, but for remote-sensing a continuous infrasonic signal would be required in order to probe the atmosphere over a longer time window.

The question is what kind of signal can be continuously measured. Infrasound sensors measure continuously random noise, generated by different sources. For a long time, noise was considered a disturbance and neglected. The ambient noise measured by microbarometers mostly consists of microbaroms. The so called "voice of the sea" is radiated by the oceans in case of marine storms, hurricanes, and high-amplitude, long-period ocean swells. A part of the acoustic energy is radiated in the atmosphere and the other part into the ocean [*Longuet-Higgins*, 1950; *Brekhovskikh et al.*, 1973], where it couples with the ocean floor and causes microseisms [*Gutenberg*, 1939; *Donn and Naini*, 1973]. The atmospheric component are the microbaroms, which can almost continuously be measured at a nearly monochromatic frequency of 0.2 Hz, which is twice the ocean surface wave frequency of 0.1 Hz (i.e., an ocean wave period of ten seconds) [*Longuet-Higgins*, 1950; *Hasselmann*, 1963].

For the first time, microbaroms were observed by *Benioff and Gutenberg* [1939] on their newly developed microbarograph. In the sixties and seventies of the last century a very productive research institute in the field of infrasound and microbaroms was the Lamont-Doherty Geological Observatory of the Columbia University in Palisades, New York. The group of researchers around William L. Donn, Eric S. Posmentier, and David Rind carried out many studies about microbaroms. *Posmentier* [1967] published the theory that microbaroms are associated with storms and generated by surface waves of the oceans. The atmospheric model of microbaroms radiation by the ocean surface was developed by *Brekhovskikh et al.* [1973]. This model was improved by taking the compressibility of the atmosphere and resonance of the water column into account [*Waxler and Gilbert*, 2006; *Waxler et al.*, 2007; *Smets and Evers*, 2014]. The resonance depends on the bathymetry.

The research group of the Lamont-Doherty Geological Observatory recognized early the potential of microbaroms as an infrasonic probe. In 1968, Eric S. Posmentier stated on the Scientific Meetings of the Panel on Remote Atmospheric Probing:

> *"Microbaroms are applicable to the problem of acoustic probing of the atmosphere through the study of their long-range propagation."*
>
> – *Posmentier and Donn* [1969]

In several studies of the following years, the group tried to gain information about the atmospheric conditions by using microbaroms as probe [*Donn and Rind*, 1971, 1972; *Rind*, 1979].

Smets and Evers [2014] probed the stratosphere and thermosphere by using observed microbaroms during the previously mentioned sudden stratospheric warming

in 2009. By employing wind and temperature data obtained from the European Centre for Medium–Range Weather Forecasts (ECMWF), a simulation of microbarom sources on the ocean and microbarom propagation was implemented. This way the observed microbaroms were traced back to their origin and the most likely stratospheric conditions were determined. In some cases the results of this remote sensing study provide more detail about the atmosphere when compared to the model outputs of the ECMWF [*Smets and Evers*, 2014].

The described efforts to trace back the origin of the microbaroms show the general challenge of using ground–truth sources for probing the atmosphere. All the previous mentioned studies rely on knowledge about the source. For these studies it was crucial to know the location and the time of the source.

In this thesis an approach is presented which makes use of microbaroms without the need of ground–truth information. The approach is called infrasonic interferometry. Infrasonic interferometry retrieves the Green's function (impulse response) of the atmosphere by crosscorrelating the infrasound records of two locations.

"By crosscorrelating noise (...) recorded at two locations on the surface, we can construct the wave field that would be recorded at one of the locations if there was a source at the other"

– *Cole* [1995]; *Rickett and Claerbout* [1999]

Rickett and Claerbout [1999] adopted this hypothesis from *Cole* [1995] and retrieved an image of the interior of the sun by using interferometry. Also in several other fields interferometry by crosscorrelating noise was successfully applied.

Weaver and Lobkis [2001] argued that acoustic thermal fluctuations contain substantial ultrasonic information and used ultrasonic noise to image the inside of an aluminum block. In oceanography *Roux et al.* [2004] retrieved the Green's function by crosscorrelating the ambient noise in the ocean measured with hydrophones.

Also in seismology ambient noise interferometry is established. *Shapiro and Campillo* [2004] crosscorrelated the microseisms recorded by seismic stations. The station pairs were separated by distances from around hundred to more than two thousand kilometers. This way a tomographic map of the velocities of the subsurface was generated. *Sabra et al.* [2005] estimated the surface wave components of the Green's function by crosscorrelating the recordings of 150 seismic stations. *Bensen et al.* [2007] discussed an inventory of established processing procedures of the ambient noise data for seismic interferometry. The basic principles of seismic interferometry were described in a tutorial by *Wapenaar et al.* [2010].

A first step to adapt these methods for atmospheric remote sensing was realized by *Haney* [2009]. The theory of the atmospheric application of interferometry was described by *Wapenaar* [2006] and *Godin* [2006]. *Haney* [2009] applied interferometry by crosscorrelating tropospherically propagating microbaroms recorded at two infrasound stations located in Alaska, separated by a distance of 13.5 km. At this scale the microbaroms have traveled through the troposphere. The crosscorrelation yielded the delay time of the microbaroms between the stations. By comparing the

obtained delay times with the tropospheric temperature and wind, Haney showed the influence of the atmospheric conditions on the delay time (see Figure 1.4). The approach to apply interferometry to infrasound is called infrasonic interferometry.

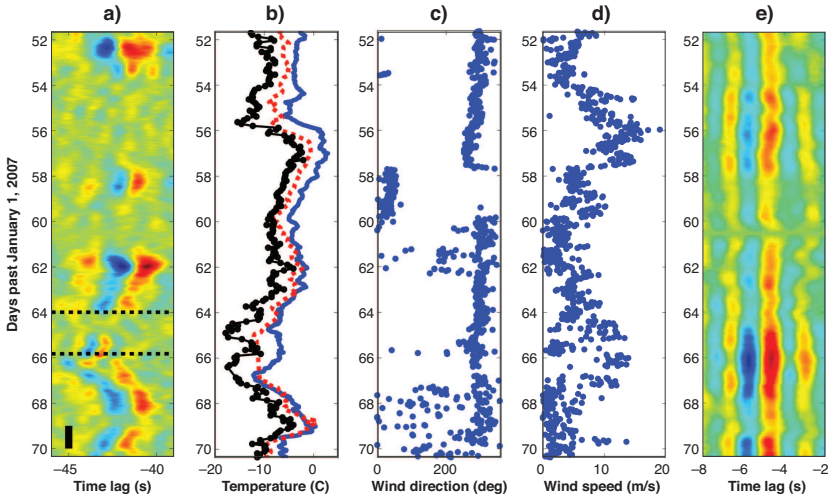


Figure 1.4: *Haney [2009] applied infrasonic interferometry to the troposphere.* ***a)*** *Crosscorrelation of microbaroms recorded at two infrasound stations in Alaska (FONW and FOSS).* ***b)*** *Temperature measured nearby the stations.* ***c)*** *and* ***d)*** *Wind speed and direction measured nearby the stations.* ***e)*** *Crosscorrelation of microseisms recorded at the same location as the infrasound.*

In this thesis, infrasonic interferometry is applied to microbaroms on a larger scale. The new research field of infrasonic interferometry is explored from the theoretical basics, via numerical experiments with synthetic data, up to the application to tropospheric and stratospheric microbaroms.

The theory of infrasound propagation through the atmosphere is discussed and how interferometry can be applied to microbaroms propagating through this moving medium. Using numerical experiments, the feasibility of infrasonic interferometry is confirmed. In the next step, infrasonic interferometry is applied to microbaroms measured by the "Large Aperture Infrasound Array" (LAIA). At this stage, the inter–station coherence, depending on the orientation of the station pair, is studied. Furthermore, the change of tropospheric wind and effective sound speed are estimated, based on the change of the crosscorrelation peaks with time. After the successful application to tropospheric microbaroms, infrasonic interferometry is applied to stratospheric microbaroms measured by the transportable USArray and the Alaskan regional array.

1.4 Structure of the thesis

The theoretical basics of infrasonic interferometry are discussed in Chapter 2. The theory chapter is divided in two parts. The first part describes the theory of infrasound propagation in the atmosphere and how the propagation can be implemented in a model by taking into account the geometrical spreading, atmospheric absorption and phase shifts. In the second part of Chapter 2 the theory of interferometry is developed from a simple one–dimensional case to the application of interferometry to waves in a nonreciprocal moving medium like the atmosphere.

In Chapter 3, the feasibility of infrasonic interferometry is studied in numerical experiments. For this purpose, synthetic recordings are generated using the model described in Chapter 2. In this numerical study it is shown that the delay times of stratospheric refracted blast waves and microbaroms can accurately be retrieved by crosscorrelation.

Chapter 4 addresses the application of infrasonic interferometry to tropospherically propagating microbaroms. The microbaroms are recorded at the "Large Aperture Infrasound Array" (LAIA). In the first part of this chapter, the inter–station coherence dependence on the orientation of the station pair is studied. The second part of Chapter 4 focusses on the estimation of tropospheric temperature and wind by using the crosscorrelation peaks.

In Chapter 5, we explore the application of infrasonic interferometry to stratospherically propagating microbaroms. The microbaroms are measured by the US-Array and the Alaskan regional array.

In Chapter 6, the conclusions of this thesis are drawn. Furthermore, an outlook for potential future research is given.

2

Theory

2.1 Modeling of the infrasound propagation

■ 2.1.1 From the general wave equation to the ray path

A wave field can be defined by the equation of motion:

$$\rho \left(\frac{\partial}{\partial t} + \vec{u} \cdot \nabla \right) \vec{v} + \nabla p \; = \; 0, \tag{2.1}$$

and the stress strain relation:

$$\kappa \left(\frac{\partial}{\partial t} + \vec{u} \cdot \nabla \right) p + \nabla \cdot \vec{v} \; = \; q, \tag{2.2}$$

where $\vec{v}(\mathbf{x}, t)$ is the particle velocity, and $p(\mathbf{x}, t)$ is the pressure, both are dependent on space ($\mathbf{x} = [x, y, z]$) and time t. $\nabla = \left(\frac{\partial}{\partial x}, \frac{\partial}{\partial y}, \frac{\partial}{\partial z} \right)$ is the nabla operator. $\vec{u}(\mathbf{x})$ is the wind, $q(\mathbf{x}, t)$ is the source distribution, $\rho(\mathbf{x})$ is the density, $\kappa(\mathbf{x}) = 1/(\rho {c_T}^2)$ is the compressibility with $c_T(\mathbf{x})$ as adiabatic sound speed. The adiabatic speed of sound $c_T(\mathbf{x}) = \sqrt{\gamma R_s T}$ depends mostly on the temperature $T(\mathbf{x})$ in Kelvin, but depends also on the ratio of specific heats γ, and the specific gas constant R_s. We are interested in the propagation direction of the sound, therefore, we can assume a source free wave field, hence $q = 0$. If we neglect also the wind ($|\vec{u}| = 0$) and assume that density ρ is constant, we can combine Equation 2.1 and Equation 2.2 to:

$$\Delta p \; = \; \frac{1}{{c_T}^2} \frac{\partial^2 p}{\partial t^2} \; , \tag{2.3}$$

where $\Delta = \nabla^2$ is the Laplace operator. This partial differential equation is called the general wave equation [*Gossard and Hooke*, 1975; *Pierce*, 1989]. Figure 2.1a shows an example of a two dimensional wave field. Red represents high pressure

level and dark blue low pressure level. The figure shows a snapshot of a continuously in all directions equally emitting point source (red peak) and the wave fronts (bright blue circles) propagating through space. The example assumes an isotropic medium, i.e., the sound propagates in all directions equally, because there are no temperature or wind gradients.

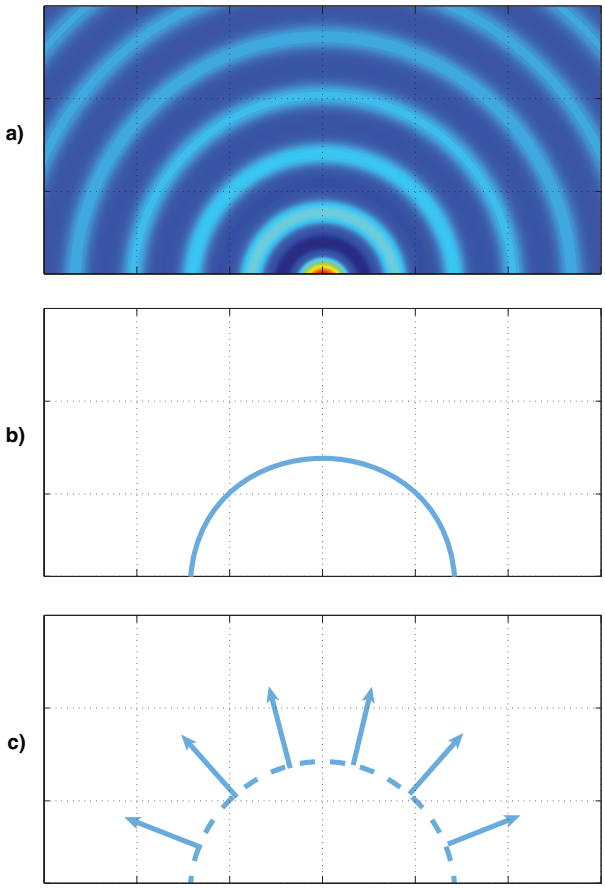


Figure 2.1: ***a)*** *Example of a two dimensional wave field. The color indicates the pressure: red is a high pressure level and dark blue a low pressure level. The figure shows a snapshot of the wave fronts (bright blue circles) propagating through space.* ***b)*** *A single wave front of the two dimensional wave field. The propagation of the wavefront is described in the Eikonal equation (Equation 2.5).* ***c)*** *The normal vectors of the wave front in b). The normal vectors are described by the Hamiltonian equation (Equation 2.8).*

If we take also the wind $\vec{u}$ into account, we obtain the following equation:

$$\Delta p \;=\; \frac{1}{{c_T}^2}\left(\frac{\partial}{\partial t} + \vec{u}\cdot\nabla\right)^2 p\;, \tag{2.4}$$

In our model we neglect the horizontal change of adiabatic sound speed $c_T(\mathbf{x}) = c_T(z)$ and of the wind $\vec{u}(\mathbf{x}) = \vec{u}(z)$. Furthermore, we only take the two horizontal components of the wind vector $\vec{u}(z) = [u_x(z), u_y(z), 0]$ into account, because the vertical wind is generally about 1% of the horizontal wind. Figure 2.2 shows an example of an adiabatic sound speed profile in a) and the wind profiles in b).

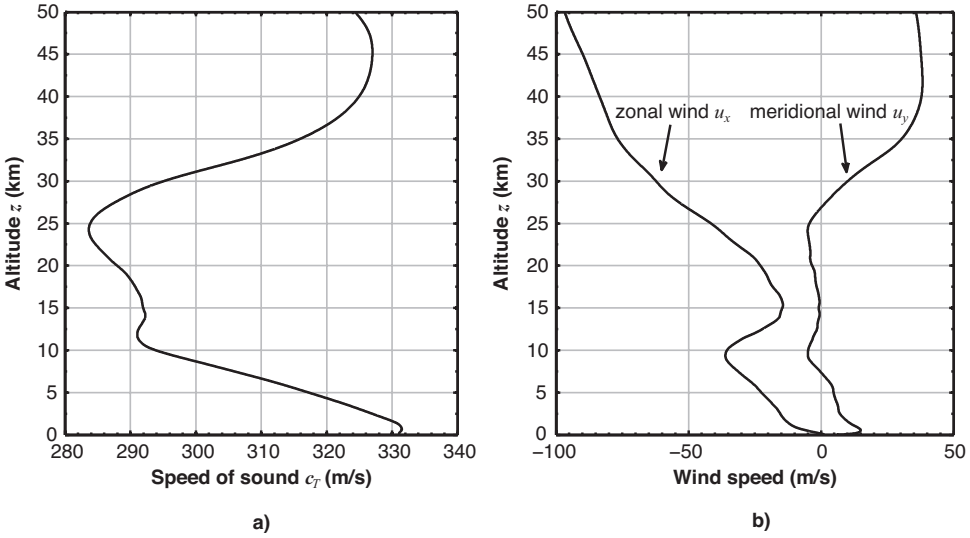


Figure 2.2: ***a)*** *The adiabatic speed of sound c_T versus altitude z.* ***b)*** *The zonal wind u_x and the meridional wind u_y versus altitude z. The wind vector $\vec{u} = (u_x, u_y)$ consists of these two components. The vertical component u_z of the wind is neglected.*

The wave equation describes the entire space–time dependent pressure of the wave field. As we are only interested in the direction in which infrasound propagates, we reduce the wave field in the first step to a single wave front which propagates through the medium. Figure 2.1b shows a snapshot of a single wave front (blue semi circle) of the example in Figure 2.1a. For this simplification it is assumed that the examined wave lengths are much smaller than the spatial change of the temperature structure, wind structure, and the reflecting surfaces [*Blom and Waxler*, 2012].

Under this high frequency assumption, the single wave front of a wave field is described by the Eikonal equation [*Virieux et al.*, 2004]:

$$(1 - \vec{u} \cdot \nabla\tau)^2 \; - \; {c_T}^2 \, (\nabla\tau)^2 \; = \; 0, \tag{2.5}$$

where $\tau(\mathbf{x}, t)$ is the travel time of the wave front. The gradient of the travel time is identical to the slowness vector $\nabla\tau = \vec{s}\,(\mathbf{x}, t)$. The slowness describes the number of seconds the sound needs to propagate a meter and points in the direction in which the sound propagates. In other words the slowness vector is parallel to the normal vector $\hat{n}$ of the wave front and its length is reciprocal to the effective sound speed c_{ef}:

$$\vec{s} = \frac{\hat{n}}{c_{ef}} \tag{2.6}$$

The effective speed of sound is an addition of adiabatic sound speed c_T with the wind $\vec{u}$ projected in the direction of sound propagation $\hat{n}$:

$$c_{ef} = c_T + \hat{n} \cdot \vec{u} \tag{2.7}$$

We are able to trace the path of the infrasound through the atmosphere by using the positions $\mathbf{x}$ of the slowness vectors, i.e., $\mathbf{x}(t)$ describes the position of the wave front dependent on the time t. In order to obtain the slowness vectors $\vec{s}(\mathbf{x}, t)$ and their positions $\mathbf{x} = (x, y, z)$, we derive the following differential equations from the Eikonal equation (Eq. 2.5):

$$\frac{dx}{dt} \; = \; s_x {c_T}^2 \; + \; u_x \, (1 - \vec{s} \cdot \vec{u}) \, , \tag{2.8a}$$

$$\frac{dy}{dt} \; = \; s_y {c_T}^2 \; + \; u_y \, (1 - \vec{s} \cdot \vec{u}) \, , \tag{2.8b}$$

$$\frac{dz}{dt} \; = \; s_z {c_T}^2 , \tag{2.8c}$$

$$\frac{ds_x}{dt} \; = \; 0, \tag{2.8d}$$

$$\frac{ds_y}{dt} \; = \; 0, \tag{2.8e}$$

$$\frac{ds_z}{dt} \; = \; - \; \vec{s} \cdot \vec{s} \, c_T \frac{\partial c_T}{\partial z} \; - \; \left(\vec{s} \cdot \frac{\partial \vec{u}}{\partial z} \right) (1 - \vec{s} \cdot \vec{u}) \tag{2.8f}$$

where $x(t)$, $y(t)$, and $z(t)$ are the spatial coordinates of the slowness vectors and $s_x(\mathbf{x}, t)$, $s_y(\mathbf{x}, t)$, and $s_z(\mathbf{x}, t)$ are the components of the slowness vectors. These ordinary differential equations are called Hamiltonian equations and are solved numerically [*Cowling et al.*, 1971; *Georges*, 1971]. The Hamiltonian equations have many possible solutions. Each solution defines a ray path. Which ray path is

obtained depends on the start position $\mathbf{x}_0$ where the calculation of the sound propagation should start and on the initial direction of the sound propagation, hence the slowness $\vec{s}_0$. Assuming the sound propagation starts at a source at the position x_0, y_0, z_0 at which the sound is emitted with the angles azimuth θ and elevation ϕ, a certain initial slowness vector $\vec{s}_0$ of the ray path can be calculated. In Figure 2.3 the definition of elevation ϕ and azimuth θ can be found.

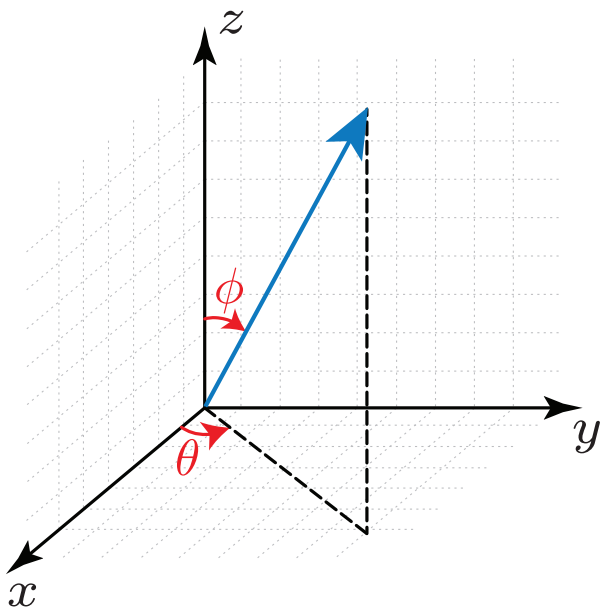


Figure 2.3: *The initial direction of the ray is defined by the emitting angles azimuth θ and elevation ϕ.*

The initial slowness vector $\vec{s}_0$ at the source is pointing in the direction of the emitting angles, but its length is the reciprocal of the effective sound speed at the source. Since the effective sound speed is an addition of adiabatic sound speed $c_{T,0}$ and the projection of the wind vector $\vec{u}_0$ at the source on the initial direction (ϕ, θ), the slowness components $s_{x,0}$, $s_{y,0}$, $s_{z,0}$ are calculated by:

$$s_{x,0} = \frac{\sin\phi\cos\theta}{c_{T,0} + u_{x,0}\sin\phi\cos\theta + u_{y,0}\sin\phi\sin\theta}, \tag{2.9a}$$

$$s_{y,0} = \frac{\sin\phi\sin\theta}{c_{T,0} + u_{x,0}\sin\phi\cos\theta + u_{y,0}\sin\phi\sin\theta}, \tag{2.9b}$$

$$s_{z,0} = \frac{\cos\phi}{c_{T,0} + u_{x,0}\sin\phi\cos\theta + u_{y,0}\sin\phi\sin\theta}. \tag{2.9c}$$

If temperature and wind at the source are assumed to be constant for a certain time, then the initial conditions only change with the emitting angles ϕ and θ. The dependency on the elevation angle ϕ can be seen in the two–dimensional example in Figure 2.4. Figure 2.4a shows the wave front in the elevation range from 55° to 90°. Figure 2.4b shows the corresponding ray paths to the wave fronts. The color of the rays indicates the elevation angle. The rays of the example are refracted in the stratosphere (ca. 40 km altitude) and in the thermosphere (> 80 km altitude). According to Snell's law, a refraction occurs, if an atmospheric layer has a different sound speed than the next layer. In other words, a sound speed contrast between two neighboring layers leads to a change of sound direction, which can cause an upward or downward refraction.

The differential equations in Equation 2.8 are solved by a Runge–Kutta–algorithm. The algorithm stops if a ray hits the ground and restarts with the last values for x, y, z, s_x, and s_y as new initial values (s_z turns direction due to the reflection at the ground and the new initial value is the negative last value of s_z), i.e., it is assumed that the ground is rigid, which means that the acoustic impedance of the ground is much bigger than acoustic impedance of the air above it. Therefore the absorption of the ground is neglected.

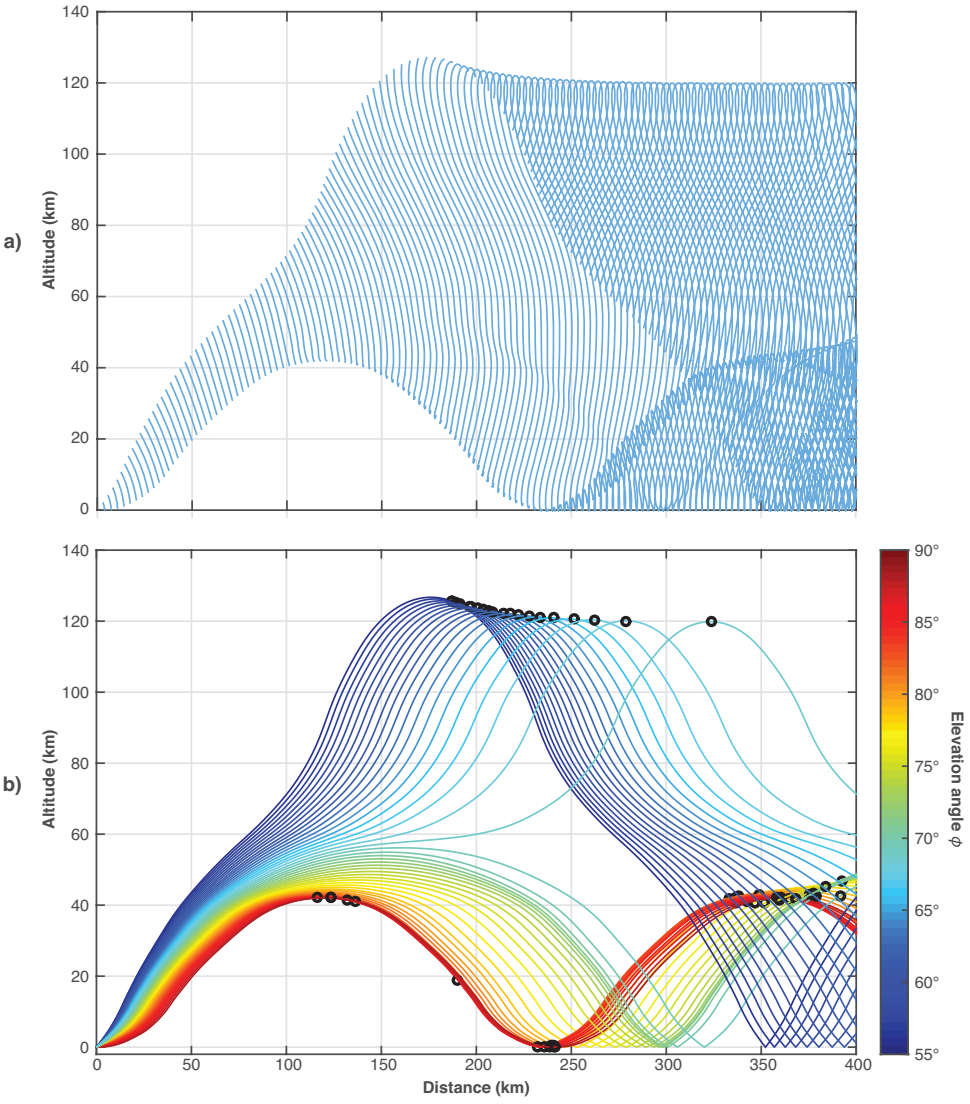


Figure 2.4: *A two–dimensional example of infrasound propagation through the atmosphere.* ***a)*** *The wave fronts in a range of elevation angles ϕ form 55° to 90° and the azimuth angle θ is kept constant.* ***b)*** *The corresponding rays show the paths of the infrasound propagation through the atmosphere. They are obtained by solving the Hamiltonian equations (Equation 2.8a – f). The color indicates the elevation angle ϕ. The black circles indicate the position of caustics (see Section 2.1.2).*

■ 2.1.2 Attenuation of Infrasound

While propagating through the atmosphere the infrasound is attenuated. There is no loss of energy due to the conservation of energy, but the kinetic energy of sound is spread over a wider area, and converted to heat by interaction with the medium. The geometrical spreading is described by the coefficient β_{spr}, which depends on the ray path. The attenuation due absorption (conversion to heat) is described by α_{abs}, which depends on the composition of the atmospheric layer.

$$|p| = \beta_{spr} e^{-\int \alpha_{abs} dr} |S| \tag{2.10}$$

where S is the source wavelet, p is the pressure along the ray. The integral over dr integrates the absorption by the crossed atmospheric layers along the ray path r. The following two sections explain how the spreading and the attenuation due to absorption are calculated.

Attenuation caused by Spreading

In order to simulate the signal, we need to determine how much energy of the source actually reaches the receiver. In a homogenous medium the energy of a point source would be equally distributed over the surface of a sphere, but in our case we assume an inhomogeneous medium, i.e., the surface over which energy is distributed depends on the ray path. The size of the surface over which the energy is spread can be found by three neighboring rays: the core ray for which the spreading is calculated, a neighbor ray with an infinitesimal different elevation ($+d\phi$), and a ray with an infinitesimal different azimuth ($+d\theta$). The differences between rays with neighboring azimuths is neglected, because their propagation path is similar. Figure 2.5a shows the three neighboring rays and the spanned surface.

By relating two surfaces $A_{\mathbf{x_0}}$ and $A_{\mathbf{x}}$ at different positions $\mathbf{x_0}$ and $\mathbf{x}$ along the ray, the amplitudes at these positions can be related [*Pierce*, 1989]:

$$|p_{\mathbf{x}}| = \sqrt{\frac{(A/\rho c_{ef})_{\mathbf{x_0}}}{(A/\rho c_{ef})_{\mathbf{x}}}} \; |p_{\mathbf{x_0}}| \;, \tag{2.11}$$

where p is the pressure amplitude, ρ is the density, and c_{ef} is the effective sound speed. The indices $\mathbf{x}$ and $\mathbf{x_0}$ mark the locations $\mathbf{x}$, and $\mathbf{x_0}$ of the two surfaces.

If we assume $p_{\mathbf{x_0}}$ to be the pressure amplitude close to the source and $p_{\mathbf{x}}$ at an arbitrary position $\mathbf{x}$ along the ray, then the square root of Equation 2.11 is the spreading coefficient β_{spr} along the ray. By using the distance from the source $r_{\mathbf{x_0}}$ and the elevation ϕ, the reference surface $A_{\mathbf{x_0}} = \left(r^2_{\mathbf{x_0}} \sin\phi \, c_{ef}\right)_{\mathbf{x_0}}$ close to the source ($r_{\mathbf{x_0}} \approx 1\,\mathrm{m}$) is calculated. The surface $A_{\mathbf{x}}$ at an arbitrary location along the ray is calculated with the Jacobian determinant $D(\mathbf{x})$ at the coordinates $\mathbf{x}$ of the ray:

$$\beta_{spr} = \sqrt{\left| \frac{\left(r^2_{\mathbf{x_0}} \sin\phi \, c_{ef} \,/\, \rho c_{ef}\right)_{\mathbf{x_0}}}{\left(D \,/\, \rho c_{ef}\right)_{\mathbf{x}}} \right|} \;, \tag{2.12}$$

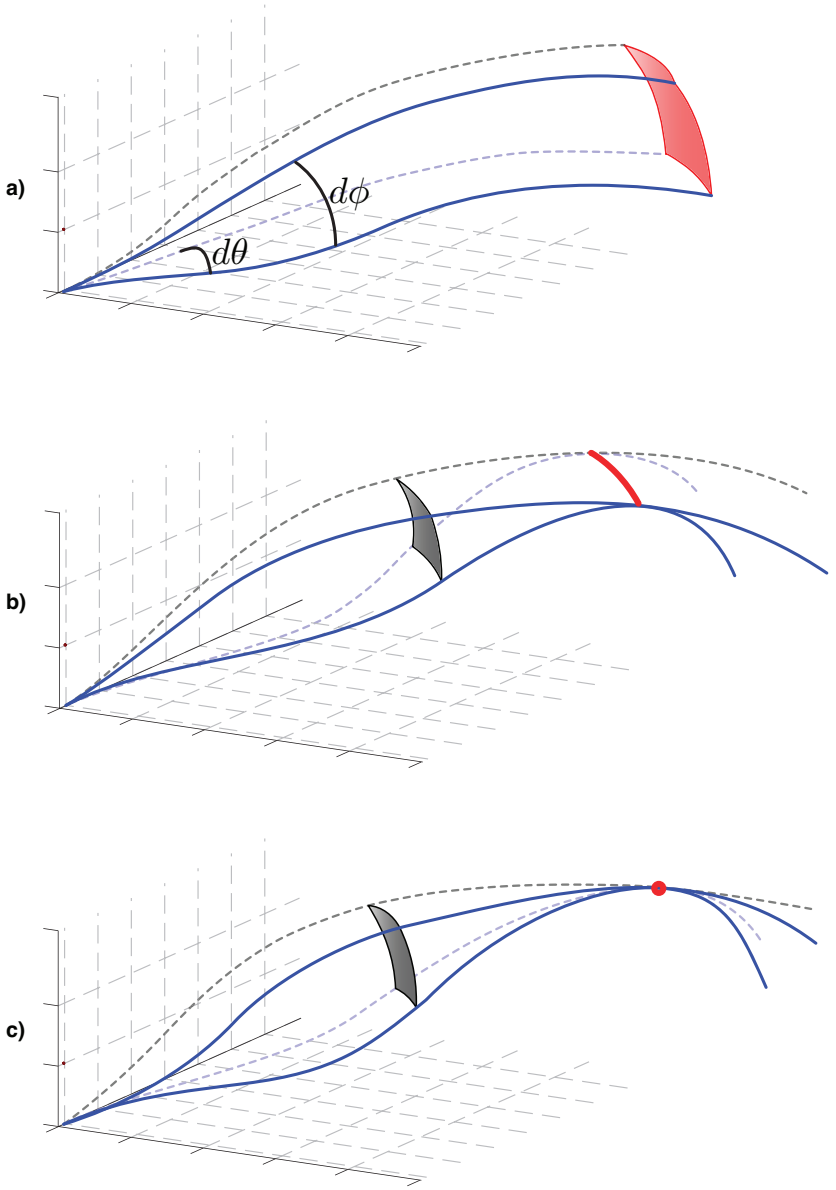


Figure 2.5: ***a)*** *The surface (red square) spanned by three neighboring rays (blue lines) can be used as a measure for the spreading of the rays. Caustics occur if the spreading of the rays shrinks to zero.* ***b)*** *First order caustics occur if the surface spanned by neighboring rays shrinks to an elementary arc (red line).* ***c)*** *Second order caustics occur if the surface spanned by neighboring rays shrinks to a point (red circle).*

Note that $r_{\mathbf{x}_0}$ is only the distance of the reference surface to the source, if the ray path between source and reference surface is assumed to be a straight line. The Jacobian determinant $D_{\mathbf{x}}$ of coordinates $\mathbf{x}(t)$ of the ray is:

$$\begin{aligned} D(\mathbf{x}(t)) &= \det\left(\frac{\partial \mathbf{x}}{\partial \phi} \quad \frac{\partial \mathbf{x}}{\partial \theta} \quad \frac{\partial \mathbf{x}}{\partial t}\right) \\ &= x\frac{\partial z}{\partial \phi}\frac{\partial x}{\partial t} + y\frac{\partial z}{\partial \phi}\frac{\partial y}{\partial t} - \left(x\frac{\partial x}{\partial \phi} + y\frac{\partial y}{\partial \phi}\right)\frac{\partial z}{\partial t}\,, \end{aligned} \tag{2.13}$$

where $\frac{\partial \mathbf{x}}{\partial \phi} = \left(\frac{\partial x}{\partial \phi}, \frac{\partial y}{\partial \phi}, \frac{\partial z}{\partial \phi}\right)$ is the change of the ray path with changing emitting angle ϕ. $\frac{\partial \mathbf{x}}{\partial \theta} = \left(\frac{\partial x}{\partial \theta}, \frac{\partial y}{\partial \theta}, \frac{\partial z}{\partial \theta}\right)$ is the change of the ray path with changing emitting angle θ. $\frac{\partial \mathbf{x}}{\partial t} = \left(\frac{\partial x}{\partial t}, \frac{\partial y}{\partial t}, \frac{\partial z}{\partial t}\right)$ is the change of the ray path with time t.

Since the differences between ray paths with neighboring azimuths is neglected, $\left(\frac{\partial x}{\partial \theta}, \frac{\partial y}{\partial \theta}, \frac{\partial z}{\partial \theta}\right)$ can be replaced by $\frac{\partial \mathbf{x}}{\partial \theta} = (y, -x, 0))$. $\frac{\partial x}{\partial t}$, $\frac{\partial y}{\partial t}$, and $\frac{\partial z}{\partial t}$ can be replaced by the differential equations (Eq. 2.8a – Eq. 2.8c):

$$\begin{aligned} D(\mathbf{x}(t)) &= x\frac{\partial z}{\partial \phi}\left({c_T}^2 s_x + u_x\left[1 - \vec{s}\cdot\vec{u}\right]\right) + y\frac{\partial z}{\partial \phi}\left({c_T}^2 s_y + u_y\left[1 - \vec{s}\cdot\vec{u}\right]\right) \\ &\quad - \left(x\frac{\partial x}{\partial \phi} + y\frac{\partial y}{\partial \phi}\right){c_T}^2 s_z\,, \end{aligned} \tag{2.14}$$

The components of the slowness vector s_x, s_y, s_z are obtained by solving the differential equations (Eq. 2.8). The derivatives $\frac{\partial x}{\partial \phi}$, $\frac{\partial y}{\partial \phi}$, and $\frac{\partial z}{\partial \phi}$ can be found by deriving the differential equations (Eq. 2.8) with respect to ϕ.

The order of the derivations is interchangeable, therefore these additional differential equations can be obtained:

$$\frac{d}{dt}\left(\frac{\partial x}{\partial \phi}\right) = \frac{\partial s_x}{\partial \phi} {c_T}^2 + s_x 2 c_T \frac{\partial c_T}{\partial z}\frac{\partial z}{\partial \phi} + \frac{\partial u_x}{\partial z}\frac{\partial z}{\partial \phi}\left(1 - \vec{s}\cdot\vec{u}\right) - u_x\left(\frac{\partial \vec{s}}{\partial \phi}\cdot\vec{u} + \vec{s}\cdot\frac{\partial \vec{u}}{\partial z}\frac{\partial z}{\partial \phi}\right), \tag{2.15a}$$

$$\frac{d}{dt}\left(\frac{\partial y}{\partial \phi}\right) = \frac{\partial s_y}{\partial \phi} {c_T}^2 + s_y 2 c_T \frac{\partial c_T}{\partial z}\frac{\partial z}{\partial \phi} + \frac{\partial u_y}{\partial z}\frac{\partial z}{\partial \phi}\left(1 - \vec{s}\cdot\vec{u}\right) - u_y\left(\frac{\partial \vec{s}}{\partial \phi}\cdot\vec{u} + \vec{s}\cdot\frac{\partial \vec{u}}{\partial z}\frac{\partial z}{\partial \phi}\right), \tag{2.15b}$$

$$\frac{d}{dt}\left(\frac{\partial z}{\partial \phi}\right) = \frac{\partial s_z}{\partial \phi} {c_T}^2 + s_z 2 c_T \frac{\partial c_T}{\partial z}\frac{\partial z}{\partial \phi}, \tag{2.15c}$$

$$\frac{d}{dt}\left(\frac{\partial s_x}{\partial \phi}\right) = 0, \tag{2.15d}$$

$$\frac{d}{dt}\left(\frac{\partial s_y}{\partial \phi}\right) = 0, \tag{2.15e}$$

$$\frac{d}{dt}\left(\frac{\partial s_z}{\partial \phi}\right) = -2\left(\vec{s}\cdot\frac{\partial \vec{s}}{\partial \phi}\right) c_T \frac{\partial c_T}{\partial z} - \vec{s}\cdot\vec{s}\left(\frac{\partial c_T}{\partial z}\right)^2 \frac{\partial z}{\partial \phi} - \vec{s}\cdot\vec{s}\, c_T \frac{\partial^2 c_T}{\partial z^2}\frac{\partial z}{\partial \phi} - \left(\frac{\partial \vec{s}}{\partial \phi}\cdot\frac{\partial \vec{u}}{\partial z}\right)\left(1 - \vec{s}\cdot\vec{u}\right) - \left(\vec{s}\cdot\frac{\partial^2 \vec{u}}{\partial z^2}\right)\frac{\partial z}{\partial \phi}\left(1 - \vec{s}\cdot\vec{u}\right) + \left(\vec{s}\cdot\frac{\partial \vec{u}}{\partial z}\right)\left(\frac{\partial \vec{s}}{\partial \phi}\cdot\vec{u}\right) + \left(\vec{s}\cdot\frac{\partial \vec{u}}{\partial z}\right)^2 \frac{\partial z}{\partial \phi}, \tag{2.15f}$$

where $\frac{\partial \vec{u}}{\partial \phi} = \left(\frac{\partial u_x}{\partial \phi}, \frac{\partial u_y}{\partial \phi}, 0\right)$ is the change of the wind vector with the emitting angle ϕ, and $\frac{\partial \vec{s}}{\partial \phi} = \left(\frac{\partial s_x}{\partial \phi}, \frac{\partial s_y}{\partial \phi}, \frac{\partial s_z}{\partial \phi}\right)$ is the change of the slowness vector with the emitting angle ϕ. These differential equations are solved together with the Hamilton equations (Eq. 2.8) by the Runge–Kutta–solver.

Figure 2.6 shows an example of the spreading coefficient of the ray paths in Figure 2.4 versus the distance from the source. In order to find the solution of these differential equations for the rays we are looking at, the correct initial conditions are required. The initial coordinates of the ray x_0, y_0, and z_0 do not change with the emitting angle ϕ. Hence the derivatives $\frac{\partial x_0}{\partial \phi}$, $\frac{\partial y_0}{\partial \phi}$, and $\frac{\partial z_0}{\partial \phi}$ are equal zero. The

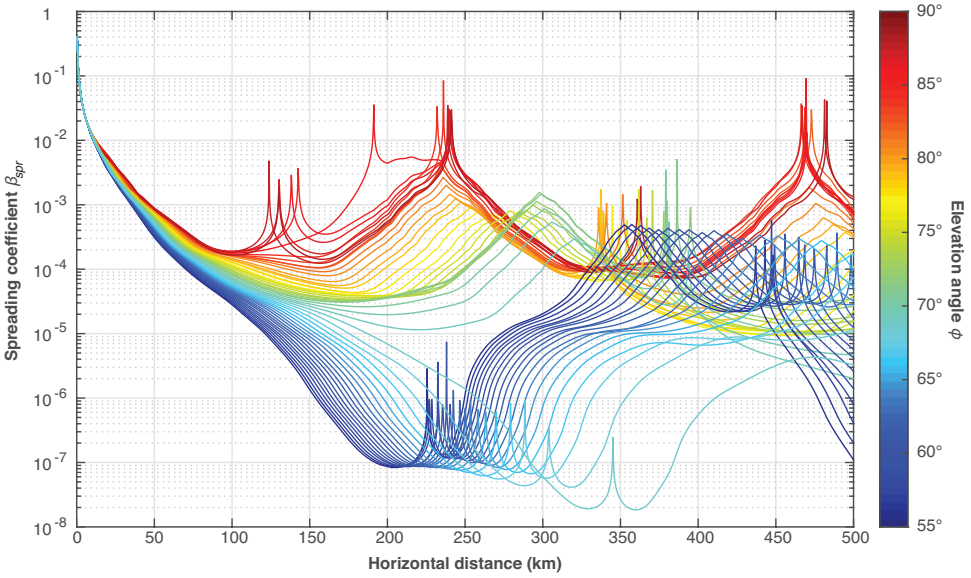


Figure 2.6: *The geometrical spreading (cf. Eq. 2.14) along the ray paths in Figure 2.4 versus the horizontal distance. It shows that thermospheric ray paths (blue curves) have significant higher geometric attenuation than stratospheric ray paths (red and yellow curves). The caustics (black circles in Figure 2.4) show as peaks in the spreading coefficient.*

derivative of the initial slowness vector $\vec{s}$ with respect to ϕ is calculated by the following equations:

$$\frac{\partial s_{x,0}}{\partial \phi} = \frac{c_{T,0}\cos\phi\cos\theta}{\left(u_{x,0}\sin\phi\cos\theta + u_{y,0}\sin\phi\sin\theta + c_{T,0}\right)^2}, \tag{2.16a}$$

$$\frac{\partial s_{y,0}}{\partial \phi} = \frac{c_{T,0}\cos\phi\sin\theta}{\left(u_{x,0}\sin\phi\cos\theta + u_{y,0}\sin\phi\sin\theta + c_{T,0}\right)^2}, \tag{2.16b}$$

$$\frac{\partial s_{z,0}}{\partial \phi} = \frac{-\left(c_{T,0}\sin\phi + u_{x,0}\cos\theta + u_{y,0}\sin\theta\right)}{\left(u_{x,0}\sin\phi\cos\theta + u_{y,0}\sin\phi\sin\theta + c_{T,0}\right)^2}, \tag{2.16c}$$

As mentioned before, the algorithm stops if a ray hits the ground and restarts with the last values for $\frac{\partial x}{\partial \phi}$, $\frac{\partial y}{\partial \phi}$, $\frac{\partial s_x}{\partial \phi}$, $\frac{\partial s_y}{\partial \phi}$, and $\frac{\partial s_z}{\partial \phi}$ as new initial values ($\frac{\partial z}{\partial \phi}$ changes direction due to the reflection and the new initial value is the negative last value of $\frac{\partial z}{\partial \phi}$).

If the spreading of the rays becomes zero the attenuation by the spreading can not be calculated. These areas are called caustics and cause a phase shift in the amplitude. A distinction can be made between first order and second order caustics. First order caustics occur if the surface spanned by three neighboring rays shrinks to an elementary arc (see Figure 2.5b). Second order caustics occur, if the three

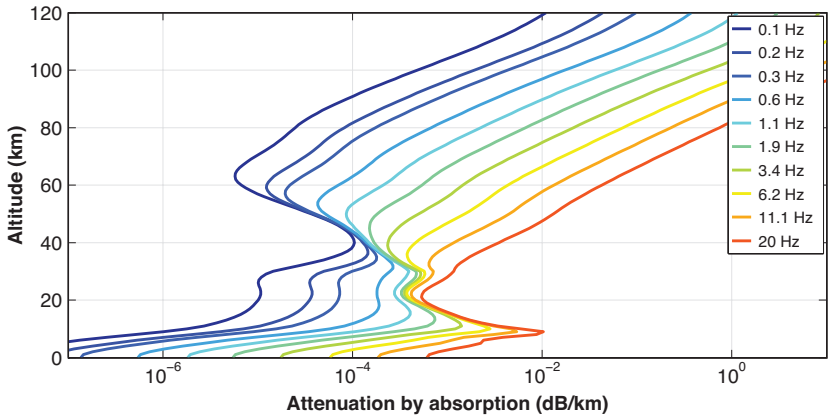


Figure 2.7: *The dependence of atmospheric absorption of acoustic waves on altitude and frequency.*

neighboring rays focus in a point (see Figure 2.5c) and are less likely. In the example in Figure 2.4 the black circles indicate the locations of the caustics. The crossing of a first order caustic causes a 90° phase shift in pressure. A second order caustic results in a phase shift of 180°. Each additional crossing of a caustic leads to an additional phase shift.

Attenuation caused by Atmospheric Absorption

Propagating sound waves are attenuated by the absorption of the atmosphere. The lower frequencies of infrasound are less attenuated than higher frequencies. Figure 2.7 shows the attenuation by atmospheric absorption α_{abs} of infrasound between 0.1 Hz and 20 Hz for altitudes up to 120 km. These absorption values were calculated according to an estimation of *Sutherland and Bass* [2004].

Sutherland and Bass [2004] showed that the absorption consists of the energy loss of viscosity (classical) α_{cl}, rotation α_{rot}, thermal diffusion α_{dif}, and vibrational relaxation α_{vb}:

$$\alpha_{abs} = \alpha_{cl} + \alpha_{rot} + \alpha_{dif} + \alpha_{vb}. \tag{2.17}$$

These absorption coefficients depend mostly on the frequency. The frequency as non–dimensional frequency ν, as the modified non–dimensional frequency $\varkappa$ and as regular frequency f in Hz:

$$\alpha_{cl} = \frac{2\pi f}{c_T} \sqrt{\frac{1}{2} \frac{\left(\sqrt{1+\nu^2}-1\right)\left(1+2.36\varkappa\right)^2}{\left(1+\nu^2\right)\left(1+\sigma 2.36\varkappa\right)^2}} , \tag{2.18a}$$

$$\alpha_{rot} = \frac{2\pi f}{c_T} \frac{\left(\sigma^2-1\right)\varkappa}{2\sigma} \chi_{O,N} \sqrt{\frac{1}{2} \frac{\left(\sqrt{1+\nu^2}+1\right)}{\left(1+\nu^2\right)\left(1+2.36\varkappa\right)^2\left(1+\sigma 2.36\varkappa\right)^2}} , \tag{2.18b}$$

$$\alpha_{dif} = 0.003\, \alpha_{cl} , \tag{2.18c}$$

$$\begin{aligned} \alpha_{vb} = & \frac{2f^2\alpha_{max,O_2}}{c_T f_{vb,O_2}\left(1+\left[\frac{f}{f_{vb,O_2}}\right]^2\right)} + \frac{2f^2\alpha_{max,N_2}}{c_T f_{vb,N_2}\left(1+\left[\frac{f}{f_{vb,N_2}}\right]^2\right)} \\ & + \frac{2f^2\alpha_{max,CO_2}}{c_T f_{vb,CO_2}\left(1+\left[\frac{f}{f_{vb,CO_2}}\right]^2\right)} + \frac{2f^2\alpha_{max,O_3}}{c_T f_{vb,O_3}\left(1+\left[\frac{f}{f_{vb,O_3}}\right]^2\right)} , \end{aligned} \tag{2.18d}$$

where c_T is the adiabatic speed of sound, σ characterizes the structure of the gas (see Equation B.3 in Appendix B), the non–dimensional frequency ν is proportional to the regular frequency f and takes the viscosity $\mu = (1.4866\times10^{-6}\sqrt{T}^3)/(T+117)$ [*NOAA et al.*, 1976] and the atmospheric pressure p into account:

$$\nu = \frac{4\mu}{3p_b} 2\pi f , \tag{2.19}$$

where the atmospheric background pressure is assumed to be $p_b = p_r \frac{\rho}{\rho_0}\frac{T}{T_0}$, with the altitude dependent density ρ, the altitude dependent temperature T, and the reference pressure $p_r = 1\times10^5$ Pa at 293.15 K (20°C). The index 0 indicates a value at the ground (sea level).

The modified non–dimensional frequency $\varkappa$ is also proportional to the regular frequency f, since $\varkappa$ is a modification of the non–dimensional frequency ν:

$$\varkappa = \frac{3}{5}\sqrt{\frac{3}{7}}\, Z_{rot}\, \nu \tag{2.20}$$

where Z_{rot} is the rotational collision number of air. The rotational collision number of air and all other parameters of Equations 2.18 – 2.20 are explained in Appendix B.

2.2 Infrasonic Interferometry

■ 2.2.1 Interferometry general

The acoustic delay time between two receivers depends on the acoustic velocity structure. This velocity structure is a function of wind and temperature in the atmosphere. By resolving the delay time from infrasonic measurements, an estimate of the wind and temperature between the two receivers can be obtained. Such a retrieval can be realized with deterministic transient sources or random noise. By using a deterministic transient source, the delay time is obtained from the known source–receiver locations. Alternatively, random ambient noise can be used to retrieve the delay time. This approach does not need ground truth events.

A possibility to gain information from the ambient noise field is to combine the recordings of two receivers located in the wave field. A feasible combination of the two recordings is to calculate the crosscorrelation between the recordings.

"Crosscorrelation functions give a measure of how well one signal correlates with another as a function of the time displacement between them."

–[*Havelock et al.*, 2008]

In this function the actual delay time between the two receivers appears as a peak. This method is called interferometry, because it takes advantage of the constructive and destructive interferences between the two recordings. The crosscorrelation of two recordings is identical to a temporal convolution of the first recording with a time reversed version of the second recording.

This section is based on the tutorial about seismic interferometry by *Wapenaar et al.* [2010]. It starts with simplified assumptions and increases the complexity stepwise. In the first step a one–dimensional scenario is examined, i.e., a plane wave is assumed, which propagates on a straight line from an impulsive source via receiver A to receiver B (see Figure 2.8a). The source is located at $x_{S,1}$, receiver A is located at x_A, and receiver B is located at x_B. The plane wave propagates with sound speed c_T and first reaches receiver A at the time $t_A = \frac{x_A - x_{S,1}}{c_T}$ (cf. Figure 2.8b) and afterwards receiver B at the time $t_B = \frac{x_B - x_{S,1}}{c_T}$ (cf. Figure 2.8c).

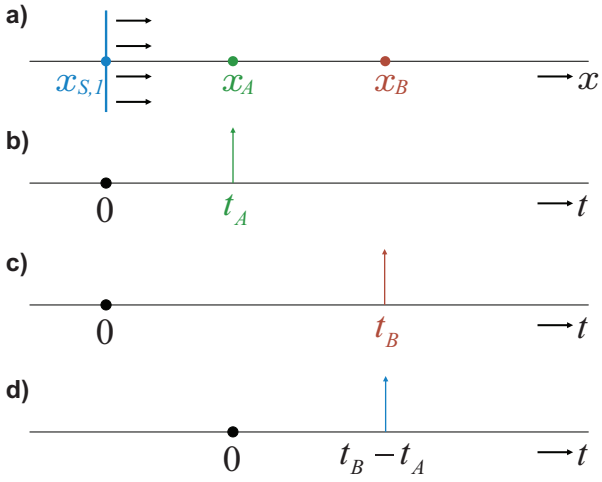


Figure 2.8: ***a)*** *The impulsive plane wave source situated at $x_{S,1}$ and the two receivers situated at x_A and x_B are considered to be located on a line.* ***b)*** *The plane wave reaches x_A first at the time t_A.* ***c)*** *The plane wave reaches x_B later at t_B.* ***d)*** *Crosscorrelation of the impulse response at receiver A ($\delta(t - t_A)$) with the impulse response at receiver B ($\delta(t - t_B)$) yields the impulse response $\delta(t - [t_B - t_A])$, which is identical to a response at x_B to an impulsive source at x_A. Figure adapted from Wapenaar et al. [2010]*

In case of an impulsive source, the receiver measures the impulse response of the medium. The impulse response is the same as the Green's function. At receiver A we retrieve the Green's function $G(x_A, x_{S,1}, t)$. The equivalent Green's function from $x_{S,1}$ to x_B is $G(x_B, x_{S,1}, t)$. The crosscorrelation of the two impulse responses is identically to a convolution of an impulse response with a second time–reversed impulse response:

$$G(x_B, x_{S,1}, t) \otimes G(x_A, x_{S,1}, t) = G(x_B, x_{S,1}, t) * G(x_A, x_{S,1}, -t), \qquad (2.21)$$

where the $\otimes$ denotes the crosscorrelation and the asterisk $*$ denotes the temporal convolution. Therefore, in the following the term crosscorrelation often refers to the temporal convolution of a Green's function with a second time–reversed Green's function:

$$G(x_B, x_{S,1}, t) * G(x_A, x_{S,1}, -t) = \int G(x_B, x_{S,1}, t + t')\, G(x_A, x_{S,1}, t')\, dt' \,. \qquad (2.22)$$

Assuming that the sound propagation is lossless, the impulse response at receiver A is $G(x_A, x_{S,1}, t) = \delta(t - t_A)$ and the impulse response at receiver B is $G(x_B, x_{S,1}, t) = \delta(t - t_B)$. Using this assumption we can write for Equation 2.22:

$$\begin{aligned} G(x_B, x_{S,1}, t) * G(x_A, x_{S,1}, -t) &= \int \delta(t + t' - t_B)\, \delta(t' - t_A)\, dt' \\ &= \delta(t - [t_B - t_A]) \\ &= \delta\left(t - \left[\frac{x_B - x_A}{c_T}\right]\right) \\ &= G(x_B, x_A, t)\,, \end{aligned} \tag{2.23}$$

i.e., the crosscorrelation between the two receiver responses to an impulsive source is the same as the impulse response at receiver B to an impulsive source at the location of receiver A. Hence, by crosscorrelating the impulse responses of two receivers we are able to obtain the Green's function between the two receivers. Therefore this approach is also called Green's function retrieval. Figure 2.8d shows the impulse response of the crosscorrelation in Equation 2.23.

Equation 2.23 is also valid for a source located at the opposite side of the two receivers, but with the difference that the time is reversed:

$$G(x_B, x_{S,2}, t) * G(x_A, x_{S,2}, -t) = G(x_B, x_A, -t)\,, \tag{2.24}$$

where $x_{S,2}$ is the location of the second source, situated on the opposite side of the receivers. Figure 2.9a shows the second source.

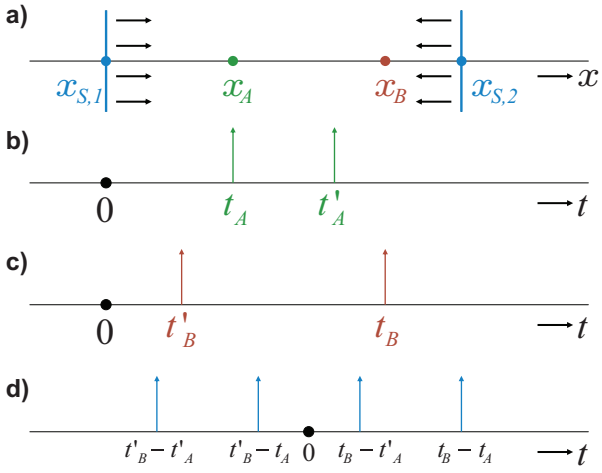


Figure 2.9: ***a)*** *A second impulsive plane wave source is located on the opposite side of the receivers at $x_{S,2}$.* ***b)*** *The leftwards propagating waves of the second source at $x_{S,2}$ reach x_A at the time t'_A, which is later than the rightwards propagating waves of the source at $x_{S,1}$.* ***c)*** *The waves of the source at $x_{S,2}$ reach x_B at the time t_B, which is earlier than the rightwards propagating waves of the source at $x_{S,1}$.* ***d)*** *Crosscorrelation between the responses at x_A and x_B. The crosscorrelation contains the impulse responses $G(x_B, x_A, t)$ at the time $t_B - t_A$ and $G(x_B, x_A, -t)$ at the time $t'_B - t'_A$. Furthermore it contains the crossterms at $t_B - t'_A$ and $t'_B - t_A$, which occur if the two sources are correlated. Figure adapted from Wapenaar et al. [2010].*

In order to combine the two impulse responses (Eq. 2.23 and Eq. 2.24) they can be added up:

$$G(x_B, x_A, t) \; + \; G(x_B, x_A, -t) \;\; = \;\; \sum_{i=1}^{2} G(x_B, x_{S,i}, t) \; * \; G(x_A, x_{S,i}, -t) \; . \qquad (2.25)$$

I.e., that the Green's function between x_A and x_B plus it's time–reversed version is the same as the crosscorrelation of two observed fields at x_A and x_B, of which each is the superposition of rightward– and leftward–propagating plane waves (cf. Figure 2.9d). Note that the impulses of the two sources are correlated. Therefore, the impulse responses of the sources must convolved separately before the summation takes place, otherwise the crossterms at $t_B - t'_A$ and $t'_B - t_A$ occur (cf. Figure 2.9d).

In the next step two uncorrelated noise sources $N_1(t)$ and $N_2(t)$ are assumed. In this case the response $p(x_A, t)$ at the receiver A is the crosscorrelation of the noise wavelet $N_i(t)$ with the corresponding Green's function $G(x_A, x_{S,i}, t)$:

$$p(x_A, t) \;\; = \;\; \sum_{i=1}^{2} G(x_A, x_{S,i}, t) \; * \; N_i(t) \qquad (2.26)$$

and the response $p(x_B, t)$ at receiver B is a similar crosscorrelation:

$$p(x_B, t) \;=\; \sum_{j=1}^{2} G(x_B, x_{S,j}, t) \;*\; N_j(t) \tag{2.27}$$

Figure 2.10a illustrates the response of receiver A and Figure 2.10b illustrates the response of receiver B.

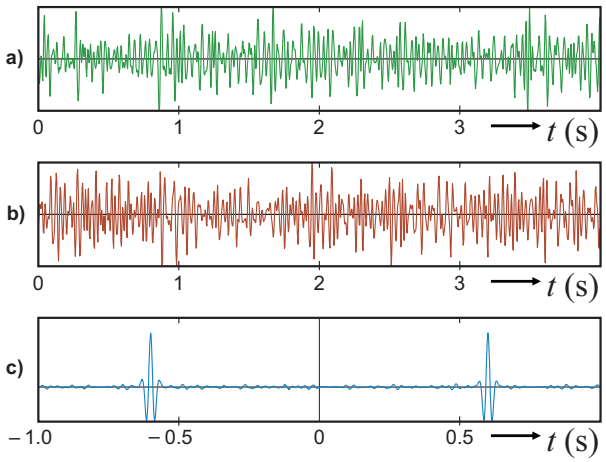


Figure 2.10: ***a)*** *The response $p(x_A, t)$ at receiver A to two uncorrelated noise sources at $x_{S,1}$ and $x_{S,2}$ (cf. Eq. 2.26).* ***b)*** *The response $p(x_B, t)$ at receiver B to the same noise sources (cf. Eq. 2.27).* ***c)*** *The result of the crosscorrelation of the two receiver responses. The two peaks are the autocorrelation of the noise S_N convolved with the impulse responses $G(x_B, x_A, t)$ and $G(x_B, x_A, -t)$ (cf. Eq. 2.31). Figure adapted from Wapenaar et al. [2010].*

The crosscorrelation of these two receiver responses yields:

$$\begin{aligned} &\Big\langle p(x_B, t) \;*\; p(x_A, -t) \Big\rangle \\ &\quad = \left\langle \sum_{j=1}^{2} \sum_{i=1}^{2} G(x_B, x_{S,j}, t) \;*\; N_j(t) \;*\; G(x_A, x_{S,i}, -t) \;*\; N_i(-t) \right\rangle , \end{aligned} \tag{2.28}$$

where $\langle ... \rangle$ denote the ensemble average. In this case the ensemble average is an average over time, but in other cases it could be also an average over several sources distributed at different locations. The idea behind the ensemble average is the assumption that different noise sources are uncorrelated and coincidentally occurring similarities between different sources cancel out by the averaging. Hence, if the two receiver responses in Equation 2.28 are convolved then the source components of the

same source measured at both receivers add up and result in the autocorrelation of the source wavelet. Mathematically this relation is expressed in the following equation:

$$\left\langle N_j(t) \ * \ N_i(-t) \right\rangle \ = \ \delta_{ij} S_N(t) \ , \tag{2.29}$$

where $S_N(t)$ is the the autocorrelation of the noise, and $\delta_{ij} = \left\{ \begin{smallmatrix} 1 \text{ if } i{=}j \\ 0 \text{ if } i{\neq}j \end{smallmatrix} \right.$ is the Kronecker delta function. Assuming the two noise sources are uncorrelated (Eq. 2.29), the crosscorrelation of the two receiver responses (Eq. 2.28) becomes:

$$\left\langle p(x_B,t) \ * \ p(x_A,-t) \right\rangle \ = \ \sum_{i=1}^{2} G(x_B, x_{S,i}, t) \ * \ G(x_A, x_{S,i}, -t) \ * \ S_N(t) \ , \tag{2.30}$$

Right hand side the crosscorrelation of the Green's function can be replaced by Equation 2.25:

$$\left\langle p(x_B,t) \ * \ p(x_A,-t) \right\rangle \ = \ \Big[G(x_B, x_A, t) \ + \ G(x_B, x_A, -t) \Big] \ * \ S_N(t) \ , \tag{2.31}$$

i.e., the crosscorrelation of the two responses to two opposite located noise sources is the same as the impulse response at receiver B to a source at the location of receiver A plus its time–reversed version convolved with the autocorrelation of the noise.

Only if the sources are situated on the the same line with the two receivers (cf. Figure 2.9a) the crosscorrelation will yield the traveltime of the direct path between the receivers, but as soon as a source is not located on this line the obtained traveltime will be too short for the direct path.

In the following section the two–dimensional distribution of sources is discussed. Figure 2.11a shows a possible random circular distribution of sources at varying distances around the two receivers. The source positions can either be described in Cartesian coordinate vectors by $\mathbf{x} = (x, y, z)$ or in polar coordinates by azimuth angle θ_S and distance from the origin r_S. In Figure 2.11a the origin of the coordinate system is located in the middle between the two receivers. Each of the sources causes a different receiver response, dependent on the source location. The source distribution in Figure 2.11a results in impulse responses at $\mathbf{x}_A$ and $\mathbf{x}_B$ shown in Figure 2.11b and c. The vertical axis shows the arrival time of the impulse at the receiver and the horizontal axis indicates the source location in polar coordinates θ_S. If the impulse responses of the two receivers are crosscorrelated separately, then each source yields a different crosscorrelation, which are shown in Figure 2.11d. The crosscorrelations show clear peaks at different delay times. The obtained delay times as a function of θ_S vary gradually, although the arrival times at the receivers (cf. Figure 2.11b and c) vary considerably with θ_S. The crosscorrelation between the two receiver responses yields the shortest delay time if the source is situated at $\theta_S = +90°$ or $\theta_S = -90°$, since the waves of the sources on this vertical axis

reach both receivers at the same time. The sources between the dashed lines yield the correct delay time of a wave propagating directly from one receiver to the other. In Figure 2.11a these sources are also marked by dashed lines. The gray area between the dashed lines is called the Fresnel zone. Figure 2.11a shows that the sources in the Fresnel zone are grouped around the horizontal axis ($\theta_S = 0°$ and $\theta_S = 180°$), where also $\mathbf{x}_{S,1}$ and $\mathbf{x}_{S,2}$ of the one–dimensional example are located (cf. Figure 2.9a). Because of the finite frequencies of the sources, not only the sources on the horizontal axis yield the correct delay time, but all sources in the gray Fresnel zone. Figure 2.11e shows the summation of all crosscorrelations in Figure 2.11d. This figure shows that the crosscorrelations of the sources located in the Fresnel zone interfere constructively and the sources outside of the Fresnel zone interfere destructively. The peaks in 2.11e occur exactly at (plus and minus) the traveltime from $\mathbf{x}_A$ to $\mathbf{x}_B$. Hence, Figure 2.11e is interpreted as the superposition of the Green's function and its time–reversed version.

By assuming uncorrelated noise sources, which superpose to the wave field, the crosscorrelation of the two receiver responses yields the autocorrelation of the noise, shown in Figure 2.11f.

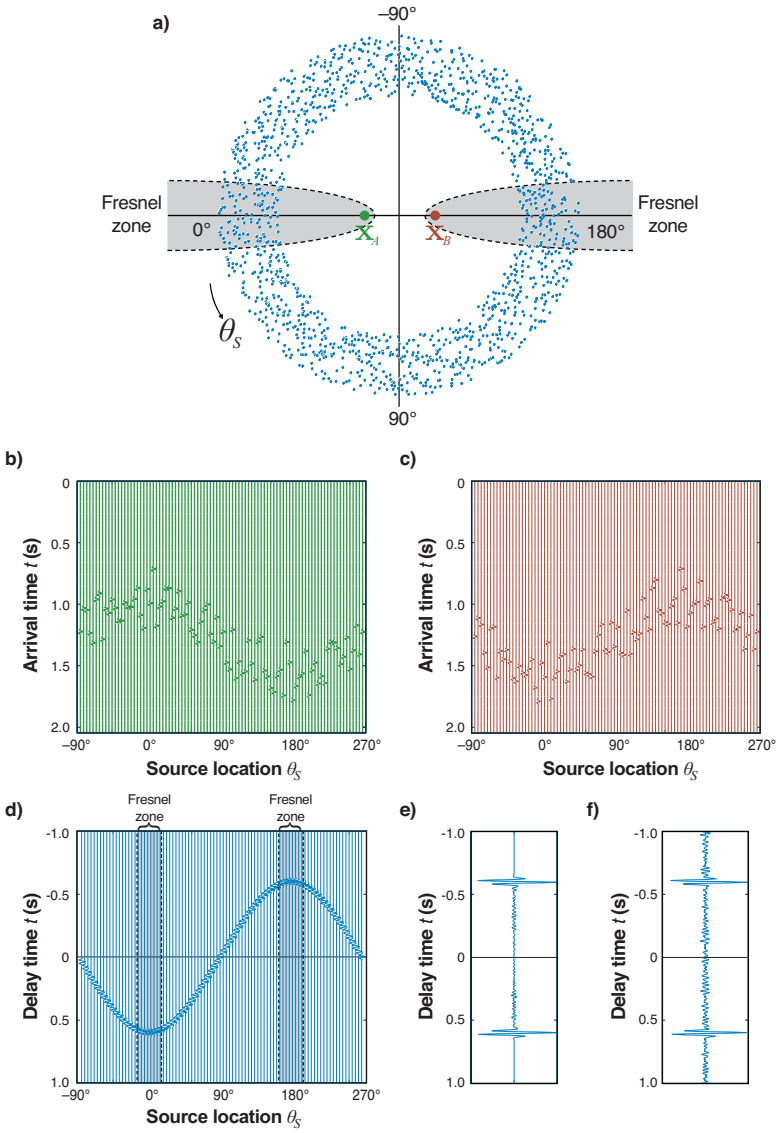


Figure 2.11: ***a)*** *Two–dimensional distribution of sources. The sources are randomly distributed in a certain range of distances from the origin of the coordinate system. The gray area between the dashed lines mark the Fresnel zone.* ***b)*** *Impulse responses at* $\mathbf{x}_A$ *to the sources with different azimuth* θ_S*.* ***c)*** *Impulse responses at* $\mathbf{x}_B$ *to the sources with different azimuth* θ_S*.* ***d)*** *Source wise crosscorrelations between the responses at* $\mathbf{x}_A$ *and* $\mathbf{x}_B$*. The gray area between the dashed lines mark the Fresnel zone.* ***e)*** *Summation of the source wise crosscorrelations. The crosscorrelations of the sources in the Fresnel zone interfere constructively and the others destructively.* ***f)*** *Crosscorrelation between the responses at* $\mathbf{x}_A$ *and* $\mathbf{x}_B$ *to noise field caused by superposition of noise sources situated at the locations in a). Figure adapted from Wapenaar et al. [2010].*

2.2.2 Interferometry in a moving medium: Nonreciprocal Green's function

This section describes the application of interferometry to an inhomogeneous moving medium and is based on *Wapenaar* [2006]. In an inhomogeneous moving medium the sound propagation is nonreciprocal. A strong wind for example leads to a faster propagation of the sound in the same direction as the wind than in the opposite direction.

In the first step, an acoustic wave field in such an inhomogeneous medium is defined. For this purpose the Fourier transform of the equation of motion (cf. Equation 2.1) and of the stress strain relation (cf. Equation 2.2) are used:

$$\frac{1}{\sqrt{2\pi}} \int_{-\infty}^{\infty} \left[\rho \left(\frac{\partial}{\partial t} + \vec{u} \cdot \nabla \right) \vec{v} \; + \; \nabla p \right] \; e^{-j\omega t} \, dt \; = \; 0 \tag{2.32a}$$

$$\rho \left(j\omega \hat{\vec{v}} + [\vec{u} \cdot \nabla] \, \hat{\vec{v}} \right) + \; \nabla \hat{p} \; = \; 0 \tag{2.32b}$$

$$\nabla \hat{p} \; = \; -\rho \left(j\omega \hat{\vec{v}} + [\vec{u} \cdot \nabla] \, \hat{\vec{v}} \right) \; , \tag{2.32c}$$

where $\vec{v}(\mathbf{x}, t)$ is the particle velocity, and $p(\mathbf{x}, t)$ is the pressure, both in time domain. In the frequency domain, $\hat{\vec{v}}(\mathbf{x}, \omega)$ is the particle velocity, and $\hat{p}(\mathbf{x}, \omega)$ is the pressure. The density of the medium $\rho(\mathbf{x})$ and the wind $\vec{u}(\mathbf{x})$ are assumed to be independent of time t and of frequency ω. $\mathbf{x} = (x, y, z)$ are the coordinates in space.

The Fourier transform of the stress strain relation (cf. Equation 2.2) is:

$$\frac{1}{\sqrt{2\pi}} \int_{-\infty}^{\infty} \left[\kappa \left(\frac{\partial}{\partial t} + \vec{u} \cdot \nabla \right) p \; + \; \nabla \cdot \vec{v} \right] \; e^{-j\omega t} \, dt \; = \; \frac{1}{\sqrt{2\pi}} \int_{-\infty}^{\infty} q \, e^{-j\omega t} \, dt \tag{2.33a}$$

$$\kappa \left(j\omega \hat{p} + \vec{u} \cdot \nabla \hat{p} \right) + \; \nabla \cdot \hat{\vec{v}} \; = \; \hat{q} \tag{2.33b}$$

$$\nabla \cdot \hat{\vec{v}} \; = \; \hat{q} - \kappa \left(j\omega \hat{p} + \vec{u} \cdot \nabla \hat{p} \right) \tag{2.33c}$$

where $\kappa(\mathbf{x})$ is the compressibility, $q(\mathbf{x}, t)$ is the spatial distribution of sources in time domain, and $\hat{q}(\mathbf{x}, \omega)$ is the spatial distribution of sources in frequency domain. For the other variables the same connotation like in Equation 2.32 is used.

For our purpose it is useful to assume an acoustic wave field caused by two independent sources, which are labeled A and B. Source A is located at position $\mathbf{x}_A$ and causes the pressure field $\hat{p}_A(\mathbf{x}, \omega)$ and the particle velocity field $\hat{\vec{v}}_A(\mathbf{x}, \omega)$. The pressure and particle velocity field are taken to be complex conjugated, to obtain a more convenient result in the end of this section (Equation 2.59, and Equation 2.60). A complex conjugation in the frequency domain is in the time domain a reversion of time.

By using Equation 2.32c $\nabla\hat{p}_A^*$ is calculated, and $\nabla\cdot\hat{\vec{v}}_A^*$ by using Equation 2.33c:

$$\nabla\hat{p}_A^* \;=\; -\rho\left(-j\omega\hat{\vec{v}}_A^* + [\vec{u}\cdot\nabla]\,\hat{\vec{v}}_A^*\right)\;, \tag{2.34a}$$

$$\nabla\cdot\hat{\vec{v}}_A^* \;=\; \hat{q}_A^* - \kappa\left(-j\omega\hat{p}_A^* + \vec{u}\cdot\nabla\hat{p}_A^*\right)\;. \tag{2.34b}$$

Source B at $\mathbf{x}_B$ contributes the pressure field $\hat{p}_B(\mathbf{x},\omega)$ and the particle velocity field $\hat{\vec{v}}_B(\mathbf{x},\omega)$. We consider a combination of the pressure and the particle velocity fields in the following manner:

$$\nabla\cdot\left(\hat{p}_A^*\hat{\vec{v}}_B \;+\; \hat{\vec{v}}_A^*\hat{p}_B\right) \tag{2.35}$$

To this derivative the product rule of Leibniz can be applied:

$$\nabla\cdot\left(\hat{p}_A^*\hat{\vec{v}}_B + \hat{\vec{v}}_A^*\hat{p}_B\right) \;=\; \left[\nabla\hat{p}_A^*\right]\cdot\hat{\vec{v}}_B + \hat{p}_A^*\left[\nabla\cdot\hat{\vec{v}}_B\right] \;+\; \left[\nabla\cdot\hat{\vec{v}}_A^*\right]\hat{p}_B + \hat{\vec{v}}_A^*\cdot\left[\nabla\hat{p}_B\right]\;. \tag{2.36}$$

In the next step the derivatives of the pressure $\nabla\hat{p}_A^*$ and $\nabla\hat{p}_B$ are substituted by Equation 2.34a respectively Equation 2.32c. The derivatives of the particle velocity $\nabla\cdot\hat{\vec{v}}_A^*$ and $\nabla\cdot\hat{\vec{v}}_B$ are substituted by Equation 2.34b respectively Equation 2.33c:

$$\begin{aligned}
\nabla\cdot\left(\hat{p}_A^*\hat{\vec{v}}_B + \hat{\vec{v}}_A^*\hat{p}_B\right) \;=\;& \left[-\rho\left(-j\omega\hat{\vec{v}}_A^* + [\vec{u}\cdot\nabla]\,\hat{\vec{v}}_A^*\right)\right]\cdot\hat{\vec{v}}_B \\
&+\; \hat{p}_A^*\left[\hat{q}_B - \kappa\left(j\omega\hat{p}_B + [\vec{u}\cdot\nabla]\,\hat{p}_B\right)\right] \\
&+\; \left[\hat{q}_A^* - \kappa\left(-j\omega\hat{p}_A^* + [\vec{u}\cdot\nabla]\,\hat{p}_A^*\right)\right]\hat{p}_B \\
&+\; \hat{\vec{v}}_A^*\cdot\left[-\rho\left(j\omega\hat{\vec{v}}_B + [\vec{u}\cdot\nabla]\,\hat{\vec{v}}_B\right)\right]\;.
\end{aligned} \tag{2.37}$$

The terms containing $j\omega$ cancel out:

$$\begin{aligned}
\nabla\cdot\left(\hat{p}_A^*\hat{\vec{v}}_B + \hat{\vec{v}}_A^*\hat{p}_B\right) =& -\rho\left([\vec{u}\cdot\nabla]\,\hat{\vec{v}}_A^*\right)\cdot\hat{\vec{v}}_B \;+\; \hat{p}_A^*\hat{q}_B \;-\; \hat{p}_A^*\kappa\left(\vec{u}\cdot\nabla\hat{p}_B\right) \\
&+\; \hat{q}_A^*\hat{p}_B \;-\; \kappa\left(\vec{u}\cdot\nabla\hat{p}_A^*\right)\hat{p}_B \;-\; \rho\hat{\vec{v}}_A^*\cdot\left([\vec{u}\cdot\nabla]\,\hat{\vec{v}}_B\right)\;,
\end{aligned} \tag{2.38}$$

where the inverse product rule of Leibniz is applied:

$$\begin{aligned}
&\nabla\cdot\left(\hat{p}_A^*\hat{\vec{v}}_B + \hat{\vec{v}}_A^*\hat{p}_B\right) \\
&=\; -\rho\,\vec{u}\cdot\nabla\left(\hat{\vec{v}}_A^*\cdot\hat{\vec{v}}_B\right) \;-\; \kappa\,\vec{u}\cdot\nabla\left(\hat{p}_B\hat{p}_A^*\right) \;+\; \hat{p}_A^*\hat{q}_B \;+\; \hat{q}_A^*\hat{p}_B\;,
\end{aligned} \tag{2.39}$$

These wave fields are assumed to occur in a volume V over which the following equation integrates:

$$\int_V \nabla \cdot \left(\hat{p}_A^* \hat{\vec{v}}_B + \hat{\vec{v}}_A^* \hat{p}_B\right) d^3\mathbf{x} = -\int_V \vec{u} \cdot \left(\rho \nabla \left[\hat{\vec{v}}_A^* \cdot \hat{\vec{v}}_B\right] + \kappa \nabla \left[\hat{p}_B \hat{p}_A^*\right]\right) d^3\mathbf{x} + \int_V \left(\hat{p}_A^* \hat{q}_B + \hat{q}_A^* \hat{p}_B\right) d^3\mathbf{x} \,. \tag{2.40}$$

The Gauss's theorem states that if a volume V with a vector field has no sinks and no sources then every flow, which enters through the boundary surface S of the volume also has to leave through the surface. Therefore, the volume integral left side of Equation 2.40 can be substituted by a surface integral:

$$\int_V \left(\hat{q}_A^* \hat{p}_B + \hat{p}_A^* \hat{q}_B\right) d^3\mathbf{x} = \oint_S \left(\hat{p}_A^* \hat{\vec{v}}_B + \hat{\vec{v}}_A^* \hat{p}_B\right) \cdot \vec{n}\, d^2\mathbf{x} + \int_V \vec{u} \cdot \left(\kappa \nabla \left[\hat{p}_A^* \hat{p}_B\right] + \rho \nabla \left[\hat{\vec{v}}_A^* \cdot \hat{\vec{v}}_B\right]\right) d^3\mathbf{x} \,. \tag{2.41}$$

The pressure and velocity fields in the surface integral $\oint_S \left(\hat{p}_A^* \hat{\vec{v}}_B + \hat{\vec{v}}_A^* \hat{p}_B\right) \cdot \vec{n}\, d^2\mathbf{x}$ do not need to be known for the entire volume V. Pressure and velocity only need to be known for the locations on the surface S. In Equation 2.41, we defined a nonreciprocal acoustic wave field tailored for our purpose.

Source A and B are assumed to be impulsive sources located inside of Volume V. Hence, the spatial source distributions $\hat{q}_A(\mathbf{x}, \omega)$ and $\hat{q}_B(\mathbf{x}, \omega)$ are Dirac impulses:

$$\hat{q}_A(\mathbf{x}, \omega) = \delta(\mathbf{x} - \mathbf{x}_A), \tag{2.42a}$$
$$\hat{q}_B(\mathbf{x}, \omega) = \delta(\mathbf{x} - \mathbf{x}_B), \tag{2.42b}$$

with $\delta(\mathbf{x} - \mathbf{x}_A)$ as Dirac at the source location $\mathbf{x}_A$, and $\delta(\mathbf{x} - \mathbf{x}_B)$ as Dirac at the source location $\mathbf{x}_B$.

Now, the wave field at an arbitrary location $\mathbf{x}$ can be understood as an impulse response to the impulsive sources at $\mathbf{x}_A$, and $\mathbf{x}_B$, since the wave field is caused by these sources. The impulse response at $\mathbf{x}$ to an impulsive source at $\mathbf{x}_A$ is the same as the Green's function $\hat{G}(\mathbf{x}, \mathbf{x}_A, \omega)$.

Hence, the pressure field $\hat{p}_A(\mathbf{x}, \omega)$ can be defined as Green's function $\hat{G}_p$ from the source location $\mathbf{x}_A$ to an arbitrary location $\mathbf{x}$ in the wave field:

$$\hat{p}_A(\mathbf{x}, \omega) = \hat{G}_p(\mathbf{x}, \mathbf{x}_A, \omega), \tag{2.43}$$

where the subscript indicates that the Green's function describes a pressure field.

The particle velocity $\hat{\vec{v}}_A(\mathbf{x},\omega)$ can also be defined by a similar Green's functions $\hat{G}_{v,i}$ from the source location $\mathbf{x}_A$ to an arbitrary location $\mathbf{x}$ in the wave field:

$$\hat{v}_{A,i}(\mathbf{x},\omega) \;=\; \hat{G}_{v,i}(\mathbf{x},\mathbf{x}_A,\omega), \tag{2.44}$$

where the index i indicates the vector components ($\hat{v}_x = \hat{G}_{v,x}$, $\hat{v}_y = \hat{G}_{v,y}$, $\hat{v}_z = \hat{G}_{v,z}$).

The equivalent Green's functions from the source location $\mathbf{x}_B$ to an arbitrary location $\mathbf{x}$ in the wave field are:

$$\hat{p}_B(\mathbf{x},\omega) \;=\; \hat{G}_p(\mathbf{x},\mathbf{x}_B,\omega), \tag{2.45a}$$

$$\hat{v}_{B,i}(\mathbf{x},\omega) \;=\; \hat{G}_{v,i}(\mathbf{x},\mathbf{x}_B,\omega). \tag{2.45b}$$

Now, $\hat{q}_A^*\hat{p}_B$, and $\hat{p}_A^*\hat{q}_B$ in Equation 2.41 can be substituted by the Green's functions in Equation 2.43 – Equation 2.45, beginning with the integral on left side of Equation 2.41:

$$\int_V \left(\hat{p}_A^*\hat{\vec{v}}_B + \hat{\vec{v}}_A^*\hat{p}_B\right) d^3\mathbf{x} \\ = \int_V \left(\left[\delta(\mathbf{x}-\mathbf{x}_A)\right]^* \hat{G}_p(\mathbf{x},\mathbf{x}_B,\omega) \;+\; \left[\hat{G}_p(\mathbf{x},\mathbf{x}_A,\omega)\right]^* \delta(\mathbf{x}-\mathbf{x}_B)\right) d^3\mathbf{x}\,. \tag{2.46}$$

These terms can be replaced by the following Green's functions:

$$\int_V \left[\delta(\mathbf{x}-\mathbf{x}_A)\right]^* \hat{G}_p(\mathbf{x},\mathbf{x}_B,\omega)\, d^3\mathbf{x} \;=\; \hat{G}_p(\mathbf{x}_A,\mathbf{x}_B,\omega)\,, \tag{2.47a}$$

$$\int_V \left[\hat{G}_p(\mathbf{x},\mathbf{x}_A,\omega)\right]^* \delta(\mathbf{x}-\mathbf{x}_B)\, d^3\mathbf{x} \;=\; \left[\hat{G}_p(\mathbf{x}_B,\mathbf{x}_A,\omega)\right]^*\,, \tag{2.47b}$$

where $\hat{G}_p(\mathbf{x}_A,\mathbf{x}_B,\omega)$ is the Green's function from $\mathbf{x}_B$ to $\mathbf{x}_A$, and $\left[\hat{G}_p(\mathbf{x}_B,\mathbf{x}_A,\omega)\right]^*$, the complex conjugate Green's function from $\mathbf{x}_A$ to $\mathbf{x}_B$. In these equations the multiplication with the Dirac can be understood as a spatial filter (also known as sift–property of the Dirac function). Hence in Equation 2.47a, the Green's function $\hat{G}_p(\mathbf{x},\mathbf{x}_B,\omega)$ from $\mathbf{x}_B$ to the pool of arbitrary locations $\mathbf{x}$ in the wave field is filtered by a spatial filter (a spike) at $\mathbf{x}_A$. As a result only the Green's function to location $\mathbf{x} = \mathbf{x}_A$ is not suppressed, while all Green's functions to other locations become zero, i.e., we obtain $\hat{G}_p(\mathbf{x}_A,\mathbf{x}_B,\omega)$.

Also the pressure and the particle velocity fields on the right side of Equation 2.41 are replaced by the Green's functions in Equation 2.43 – Equation 2.45:

$$\hat{G}_p(\mathbf{x}_A, \mathbf{x}_B, \omega) \; + \; \left[\hat{G}_p(\mathbf{x}_B, \mathbf{x}_A, \omega)\right]^* \; = \; \sum_{n=1}^{4} I_n, \tag{2.48}$$

with:

$$I_1 \; = \; \oint_S \left[\hat{G}_p(\mathbf{x}, \mathbf{x}_A, \omega)\right]^* \; \hat{G}_{v,i}(\mathbf{x}, \mathbf{x}_B, \omega) \; n_i \; d^2\mathbf{x}, \tag{2.49a}$$

$$I_2 \; = \; \oint_S \left[\hat{G}_{v,i}(\mathbf{x}, \mathbf{x}_A, \omega)\right]^* \; \hat{G}_p(\mathbf{x}, \mathbf{x}_B, \omega) \; n_i \; d^2\mathbf{x}, \tag{2.49b}$$

$$I_3 \; = \; \int_V \kappa \, u_k \, \nabla_k \Big(\left[\hat{G}_p(\mathbf{x}, \mathbf{x}_A, \omega)\right]^* \; \hat{G}_p(\mathbf{x}, \mathbf{x}_B, \omega) \Big) \; d^3\mathbf{x}, \tag{2.49c}$$

$$I_4 \; = \; \int_V \rho \, u_k \, \nabla_k \Big(\left[\hat{G}_{v,i}(\mathbf{x}, \mathbf{x}_A, \omega)\right]^* \; \hat{G}_{v,i}(\mathbf{x}, \mathbf{x}_B, \omega) \Big) \; d^3\mathbf{x}, \tag{2.49d}$$

where $u_k \nabla_k$ denotes the component–wise multiplications of the dot product $\vec{u} \cdot \nabla = u_x \frac{\partial}{\partial x} + u_y \frac{\partial}{\partial y} + u_z \frac{\partial}{\partial z}$. This notation is used in all following equations. Note that the Green's functions in I_1 and I_2 only need to be known for receiver locations on the surface S, i.e., in Equation 2.49a and 2.49b, $\mathbf{x}$ is located on S.

In order to simplify Equation 2.49, some approximations are made. It is assumed that the waves described by Green's functions pass the surface S towards the outside. It is also assumed that the wind u_k is small in comparison to the sound speed c, i.e., the Mach number is much smaller than 1:

$$\left| \frac{u_k n_k}{c_T} \right| \; \ll \; 1 \, , \tag{2.50}$$

Furthermore, source and receivers are thought to be located further apart than the double wave length (far field). Under this assumption the pressure and particle velocity have the same phase and only differ in the amplitude:

$$\hat{G}_{v,i} n_i \; \approx \; \frac{1}{\rho c_T} \, \hat{G}_p \, , \tag{2.51}$$

ρc is also know as the acoustic impedance Z for a plane wave. This far field assumption causes an error in amplitude if the waves do not pass the evolving surface S orthogonally, i.e., in direction of the normal vector $\vec{n}$. In a wave field with a flow $\vec{u}$ the waves do not necessarily pass the evolving surface S orthogonally. This leads to an error in the amplitude, but the phase is not influenced by this assumption. Using this assumption the angle between propagation direction and the normal vector $\vec{n}$ can be neglected.

Applying the mentioned approximations to I_1 and I_2 (Eq. 2.49a, and Eq. 2.49b) yields:

$$I_1 \approx I_2 \approx \frac{1}{\rho c_T} \oint_S \hat{G}^*(\mathbf{x}, \mathbf{x}_A, \omega)\, \hat{G}(\mathbf{x}, \mathbf{x}_B, \omega)\, d^2\mathbf{x}\,, \tag{2.52}$$

where $\hat{G}$ is used instead of $\hat{G}_p$.

In the next step, the influence of the wind u_k on I_3 and I_4 in Equation 2.48 is studied. Assuming that the contribution of the derivative of wind u_k and of density ρ are small in comparison to the contribution of the derivative of the Green's functions, the Gaussian theorem can be applied to Equation 2.49c and κ be replaced by $\kappa = 1/(\rho {c_T}^2)$:

$$I_3 \approx \frac{1}{\rho c_T} \oint_S \hat{G}^*(\mathbf{x}, \mathbf{x}_A, \omega)\, \hat{G}(\mathbf{x}, \mathbf{x}_B, \omega)\, \frac{u_k n_k}{c_T}\, d^2\mathbf{x}\,, \tag{2.53}$$

Equation 2.50 states that the wind u_k is small in comparison to the sound speed c, therefore I_3 (Eq. 2.53) is much smaller than I_1 (Eq. 2.52):

$$I_3 \ll I_1\,, \tag{2.54}$$

Again the contribution of the derivative of wind u_k and of density ρ are considered to be small in comparison to the contribution of the derivative of the Green's functions and the Gauss's theorem can also be applied to Equation 2.49d. Taking Equation 2.51) into account yields:

$$I_4 \approx I_3 \approx \frac{1}{\rho c_T} \oint_S \hat{G}^*(\mathbf{x}, \mathbf{x}_A, \omega)\, \hat{G}(\mathbf{x}, \mathbf{x}_B, \omega)\, \frac{u_k n_k}{c_T}\, d^2\mathbf{x}\,. \tag{2.55}$$

which leads, according to the relations 2.50 and 2.54 to the conclusion:

$$I_4 \ll I_1\,, \tag{2.56}$$

Hence I_3 and I_4 in Equation 2.49c and 2.49d can be neglected. Replacing in Equation 2.49 I_1 and I_2 (Eq. 2.49a and b) by their approximation (Eq. 2.52) yields:

$$\hat{G}(\mathbf{x}_A, \mathbf{x}_B, \omega) + \hat{G}^*(\mathbf{x}_B, \mathbf{x}_A, \omega) \approx \frac{2}{\rho c_T} \oint_S \hat{G}^*(\mathbf{x}, \mathbf{x}_A, \omega)\, \hat{G}(\mathbf{x}, \mathbf{x}_B, \omega)\, d^2\mathbf{x}\,, \tag{2.57}$$

Next, the wind in the acoustic wave field is turned in the opposite direction; i.e., u_k is replaced by $-u_k$. This step allows also to turn the direction of the Green's functions [*Wapenaar and Fokkema*, 2004; *Brekhovskikh and Godin*, 2010]:

$$\hat{G}(\mathbf{x}_B, \mathbf{x}_A, \omega) + \hat{G}^*(\mathbf{x}_A, \mathbf{x}_B, \omega) \approx \frac{2}{\rho c_T} \oint_S \hat{G}^*(\mathbf{x}_A, \mathbf{x}, \omega)\, \hat{G}(\mathbf{x}_B, \mathbf{x}, \omega)\, d^2\mathbf{x}\,, \tag{2.58}$$

where $\hat{G}(\mathbf{x}_B, \mathbf{x}_A, \omega)$ is the Green's function from $\mathbf{x}_A$ to $\mathbf{x}_B$, $\hat{G}^*(\mathbf{x}_A, \mathbf{x}_B, \omega)$ is the conjugate complex Green's function from $\mathbf{x}_B$ to $\mathbf{x}_A$, $\hat{G}^*(\mathbf{x}_A, \mathbf{x}, \omega)$ is the conjugate

complex Green's function from $\mathbf{x}$ to $\mathbf{x}_A$, $\hat{G}(\mathbf{x}_B, \mathbf{x}, \omega)$ is the Green's function from $\mathbf{x}$ to $\mathbf{x}_B$.

By the interchange in Equation 2.58 the previous source coordinates $\mathbf{x}_A$ and $\mathbf{x}_B$ become receiver coordinates. Receiver A at $\mathbf{x}_A$ and receiver B at $\mathbf{x}_B$ are introduced. At the same time the previous arbitrary coordinates of the acoustic wave field $\mathbf{x}$ become arbitrary source locations. For example $\hat{G}(\mathbf{x}_B, \mathbf{x}, \omega)$ is the Green's function from an arbitrary location $\mathbf{x}$ in the wave field to a receiver B. In Equation 2.58, only source locations $\mathbf{x}$ on the surface S need to be taken into account (cf. Eq. 2.41).

Next, Equation 2.58 is transformed back to the time domain. The transformation of the conjugate complex Green's function ($\hat{G}^*(\mathbf{x}_A, \mathbf{x}, \omega)$) yields the time–reversed Green's function ($G(\mathbf{x}_A, \mathbf{x}_B, -t)$) in the time domain:

$$G(\mathbf{x}_B, \mathbf{x}_A, t) \; + \; G(\mathbf{x}_A, \mathbf{x}_B, -t) \; \approx \; \frac{2}{\rho c_T} \oint_S G(\mathbf{x}_B, \mathbf{x}, t) \; * \; G(\mathbf{x}_A, \mathbf{x}, -t) \; d^2\mathbf{x} \; , \quad (2.59)$$

where the asterisk ($*$) denotes a temporal convolution. Convolved are $G(\mathbf{x}_A, \mathbf{x}, -t)$, the time–reversed Green's function from a source at $\mathbf{x}$ to receiver A (at $\mathbf{x}_A$), with $G(\mathbf{x}_B, \mathbf{x}, t)$, the Green's function from the same source to receiver B (at $\mathbf{x}_B$). The surface integral ($\oint_S$) integrates over the enclosing surface S of the volume V in which the two receivers A and B are located. $G(\mathbf{x}_B, \mathbf{x}_A, t)$ represents the Green's function from receiver A to receiver B, and $G(\mathbf{x}_A, \mathbf{x}_B, -t)$ is the time–reversed Green's function of propagation in the opposite direction. As already mentioned in Equation 2.21, the convolution of a function with a time–reversed function is the same as a crosscorrelation of the two functions:

$$G(\mathbf{x}_B, \mathbf{x}_A, t) \; + \; G(\mathbf{x}_A, \mathbf{x}_B, -t) \; \approx \; \frac{2}{\rho c_T} \oint_S G(\mathbf{x}_B, \mathbf{x}, t) \; \otimes \; G(\mathbf{x}_A, \mathbf{x}, t) \; d^2\mathbf{x} \; , \quad (2.60)$$

where $\otimes$ denotes the crosscorrelation. I.e., the crosscorrelation of two receiver responses in a moving medium is the same as the impulse response at receiver B to a source at the location of receiver A plus the time–reversed version of the impulse response at receiver A to a source at the location of receiver B.

3

Infrasonic Interferometry of Stratospherically Refracted Microbaroms – A Numerical Study

Abstract

The atmospheric wind and temperature can be estimated through the traveltimes of infrasound between pairs of receivers. The traveltimes can be obtained by infrasonic interferometry. In this study, the theory of infrasonic interferometry is verified and applied to modeled stratospherically refracted waves. Synthetic barograms are generated using a raytracing model and taking into account atmospheric attenuation, geometrical spreading, and phase shifts due to caustics. Two types of source wavelets are implemented for the experiments: blast waves and microbaroms. In both numerical experiments, the traveltimes between the receivers are accurately retrieved by applying interferometry to the synthetic barograms. It is shown that microbaroms can be used in practice to obtain the traveltimes of infrasound through the stratosphere, which forms the basis for retrieving the wind and temperature profiles.

Published as: Fricke, J. T., Allouche, N. E., Simons, D. G., Ruigrok, E. N., Wapenaar, K., and Evers, L. G. (2013). Infrasonic interferometry of stratospherically refracted microbaroms – A numerical study. J. Acoust. Soc. Am., 134(4):2660–2668. Note that minor changes have been introduced to make the text consistent with the other chapters of this thesis.

3.1 Introduction

In 1996 the Comprehensive Nuclear–Test–Ban Treaty Organization (CTBTO) chose the measurements of infrasound as one of its verification techniques. Ever since, the study of infrasound has experienced a renaissance [*Dahlman et al.*, 2009]. The Treaty is verified through the International Monitoring System (IMS), which uses, in addition to the infrasound recordings, seismic, hydroacoustic and radionuclide measurements.

The traveltimes of infrasound through the atmosphere and their detectability strongly depend on the temperature and the wind in the stratosphere [*Gutenberg*, 1939]. As a consequence of this dependency, temperature and wind profiles can be estimated by measuring the traveltimes of infrasound. For such an estimation, an inversion of the model of infrasound propagation through the atmosphere is required. Numerical studies for building such an inverse model of the atmosphere are done by *Drob et al.* [2010] and *Lalande et al.* [2012].

Accurate traveltimes are an essential input for the inverse model, since small changes in traveltime can lead to large changes in output (temperature and wind). Usually, the traveltimes are measured by a ground–truth event, e.g., an explosion [*Evers et al.*, 2012], or a volcanic eruption [*Le Pichon et al.*, 2005]. This dependency on a ground–truth event has the disadvantage that the exact time and location of the event need to be known. Another disadvantage is the very limited occurrence of ground–truth events.

The traveltimes can also be estimated using a method called infrasonic interferometry. This is based on the theory of nonreciprocal Green's function retrieval by crosscorrelation [*Wapenaar*, 2006; *Godin*, 2006]. This theory determines the outcome of the crosscorrelation of the measured noise field at two receivers A and B in a moving medium. Assuming the noise field is equipartitioned, this crosscorrelation converges to the Green's function from receiver A to receiver B plus the time–reversed Green's function from receiver B to receiver A, convolved with the autocorrelation of the noise. In other words, the traveltimes between two receivers can be determined by crosscorrelating the ambient noise at these two receivers.

The interferometry of acoustic and elastic waves has successfully been applied in oceanography [*Roux et al.*, 2004], in seismology [*Shapiro and Campillo*, 2004; *Sabra et al.*, 2005; *Bensen et al.*, 2007; *Draganov et al.*, 2007], and in ultrasonic applications [*Weaver and Lobkis*, 2001].

In a first study with direct tropospheric waves, *Haney* [2009] has shown that interferometry can also be applied to infrasonic ambient noise. Haney retrieves the temperature and the strength of the wind in the troposphere by using this method. *Marcillo and Johnson* [2010] have demonstrated that the wind vector can also be resolved by applying interferometry to three infrasound sensors. The ambient infrasonic fluctuations consist mostly of microbaroms [*Posmentier*, 1967]. Microbaroms result from the nonlinear interaction of oceanic waves. Microbaroms are almost continuously present at a frequency of 0.2 Hz [*Brekhovskikh et al.*, 1973; *Donn and Naini*, 1973].

In this numerical study, infrasonic interferometry is applied to stratospherically

refracted microbaroms. With this approach, the traveltimes of infrasound through the stratosphere are obtained. Observations of temperature and wind above an altitude of 20 km are very limited. Therefore, successful application of the interferometric technique to stratospheric infrasound will have a direct use for the validation of upper atmospheric models.

The first part of this paper discusses the theoretical background of interferometry. In the second part, a detailed description of the applied model is given. The third part presents the results of the interferometry applied to numerical data which are generated with the model.

3.2 Infrasonic Interferometry

In this paper, interferometry is applied to stratospherically refracted infrasound. A derivation of the interferometric relations is given by *Wapenaar* [2006], which we will summarize in this section.

The atmosphere through which the infrasound propagates is a moving medium. In the aforementioned paper it is shown how interferometry can be used in such a moving medium, under the assumption that the flow velocity of the medium is small in comparison to the sound speed. For higher Mach numbers this approach becomes less accurate for amplitudes, but it still predicts the traveltimes very well. The Green's function between two receivers can be expressed as:

$$G(\mathbf{x}_B, \mathbf{x}_A, t) \; + \; G(\mathbf{x}_A, \mathbf{x}_B, -t) \; \approx \; \frac{2}{\rho c_T} \oint_S G(\mathbf{x}_A, \mathbf{x}, -t) \; * \; G(\mathbf{x}_B, \mathbf{x}, t) \; d^2\mathbf{x} \; , \quad (3.1)$$

where the asterisk ($*$) denotes a temporal convolution. Convolved are $G(\mathbf{x}_A, \mathbf{x}, -t)$, the time–reversed Green's function from a source at $\mathbf{x}$ to receiver A (at $\mathbf{x}_A$), with $G(\mathbf{x}_B, \mathbf{x}, t)$, the Green's function from the same source to receiver B (at $\mathbf{x}_B$). The surface integral ($\oint_S$) integrates along all sources $\mathbf{x}$ on boundary surface S of the volume in which the two receivers A and B are located. $G(\mathbf{x}_B, \mathbf{x}_A, t)$ represents the Green's function of infrasound propagation from receiver A to receiver B, and $G(\mathbf{x}_A, \mathbf{x}_B, -t)$ is the time–reversed Green's function of propagation in the opposite direction. Equation 3.1 holds for inhomogeneous density $\rho(\mathbf{x})$, sound speed $c(\mathbf{x})$, and wind velocity $\vec{u}(\mathbf{x})$ inside surface S. At and outside S the medium is assumed to be homogeneous (denoted by c and ρ in Eq. 3.1) and the wind velocity is assumed to be small in comparison with the sound speed. In the case discussed in this paper, the receivers are located on the ground and the waves reach them through the atmosphere. We consider the ground as a totally reflecting (rigid) surface. Since the normal component of the particle velocity on the rigid surface is zero, the integrand of the representation integral underlying Equation 3.1 vanishes on the ground surface [*Wapenaar and Fokkema*, 2006] (see Figure 3.1a). Thus, the integration in Equation 3.1 over a closed surface can be replaced by an integration over only the upper hemisphere. Equation 3.1 is valid for both two and three dimensions, but here we will proceed with a two dimensional configuration. Therefore the integration over a hemisphere is reduced to an integration over the semi circle L (see Figure 3.1b).

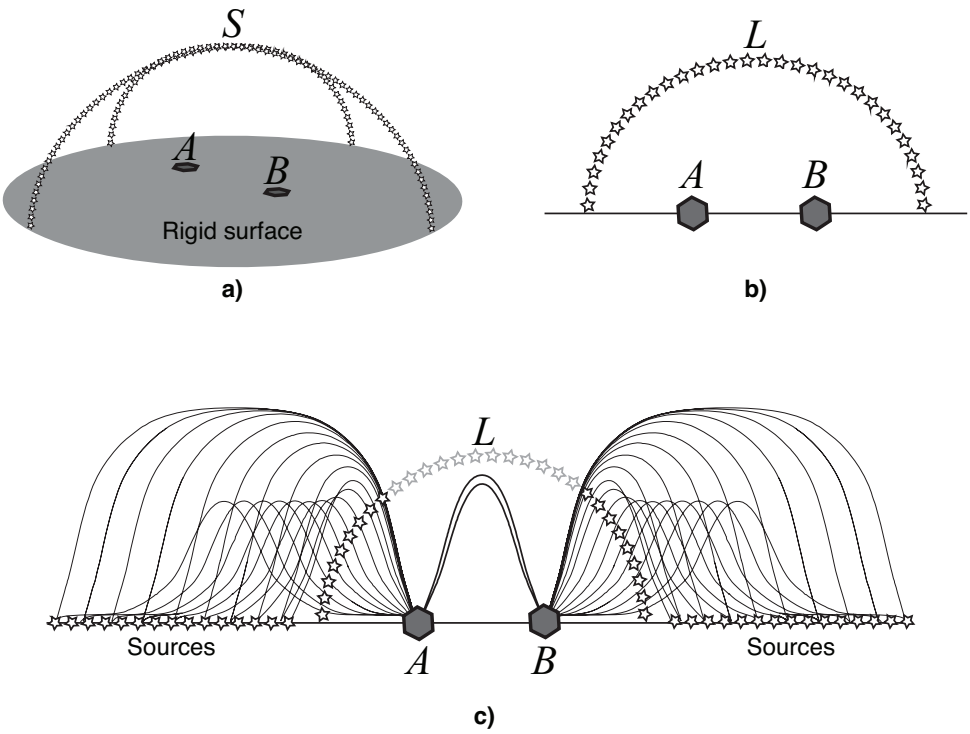


Figure 3.1: ***a)*** *Two receivers (A and B) on the ground (rigid surface) in a volume with the surface S on which the sources x are located.* ***b)*** *The integration over the hemisphere above the receivers A and B can be reduced by an integration over the semi circle L.* ***c)*** *The sources denoted by the black stars on the semi circle L can be represented by stratospherically refracted sources on the ground. The sources in gray are not represented in this example.*

Hence, the integration over the sources on the semi circle L can be expressed by the following simplification of Equation 3.1:

$$G(\mathbf{x}_B, \mathbf{x}_A, t) \; + \; G(\mathbf{x}_A, \mathbf{x}_B, -t) \; \approx \; \frac{2}{\rho c_T} \int_L G(\mathbf{x}_A, \mathbf{x}, -t) \; * \; G(\mathbf{x}_B, \mathbf{x}, t) \; d\mathbf{x} \; , \quad (3.2)$$

where G denotes now a two dimensional Green's function, which includes the rigid ground surface boundary conditions. Equation 3.2 applies for impulsive sources (at all $\mathbf{x}$ on L) like blast waves. Suppose now there are uncorrelated noise sources $N(\mathbf{x}, t)$ which are distributed at locations $\mathbf{x}$ on semi circle L, whose wave fields are recorded simultaneously by receiver A and B. An example of such sources could be the microbaroms which are part of the ambient noise field. Since the sources of microbaroms are located on the oceans, the sources do not lie on semi circle L, but on ground level. The microbaroms are refracted by the stratosphere. According to

the Huygens principle, these refracted microbaroms can be represented as sources that are located on the semi circle L [*Ruigrok et al.*, 2010]. Figure 3.1c shows an example of how the sources (black stars) on L can represent sources on the ground. The other sources (gray stars) are not represented in this example, but they would not contribute to the result because they are located outside the Fresnel zone [*Wapenaar et al.*, 2010]. If all these sources are uncorrelated the ensemble average over their correlations equals $C(t)$, the autocorrelation of N, times a spatial delta function, according to:

$$\langle N(\mathbf{x}, -t) \ * \ N(\mathbf{x}', t)\rangle \ = \ C(t)\delta(\mathbf{x} - \mathbf{x}') \ , \tag{3.3}$$

with $\mathbf{x}$ and $\mathbf{x}'$ as locations of two sources, $\langle N(\mathbf{x}, -t) \ * \ N(\mathbf{x}', t)\rangle$ indicates an ensemble average and δ a spatial Dirac impulse on L. In practice, the ensemble averaging is replaced by integrating over sufficiently long time. The observed pressure p, at receiver A and receiver B, consists of all noise sources N convolved with Green's functions:

$$p(\mathbf{x}_A, t) \ = \ \int_L G(\mathbf{x}_A, \mathbf{x}, t) \ * \ N(\mathbf{x}, t) d\mathbf{x} \ , \quad \text{and} \tag{3.4a}$$

$$p(\mathbf{x_B}, t) \ = \ \int_L G(\mathbf{x}_B, \mathbf{x}, t) \ * \ N(\mathbf{x}, t) d\mathbf{x} \ . \tag{3.4b}$$

The crosscorrelation of the measured ambient noise at receiver A and receiver B can be expressed by crosscorrelating Equation 3.4a with 3.4b:

$$\begin{aligned} &\langle p(\mathbf{x}_A, -t) \ * \ p(\mathbf{x}_B, t)\rangle \\ = \ &\left\langle \int_L G(\mathbf{x}_A, \mathbf{x}, -t) * N(\mathbf{x}, -t) \ d\mathbf{x} \ * \ \int_L G(\mathbf{x}_B, \mathbf{x}', t) * N(\mathbf{x}', t) \ d\mathbf{x}' \right\rangle . \end{aligned} \tag{3.5}$$

If we substitute the spatial ensemble average of the noise sources by the autocorrelation (Equation 3.3) we find

$$\begin{aligned} &\langle p(\mathbf{x}_A, -t) \ * \ p(\mathbf{x}_B, t)\rangle \\ = \ &\int_L \int_L G(\mathbf{x}_A, \mathbf{x}, -t) \ * \ G(\mathbf{x}_B, \mathbf{x}', t) \ * \ C(t)\delta(\mathbf{x} - \mathbf{x}') \ d\mathbf{x} \ d\mathbf{x}' \ . \end{aligned} \tag{3.6}$$

Using the sift–property of the delta function, we get

$$\langle p(\mathbf{x}_A, -t) \ * \ p(\mathbf{x}_B, t)\rangle \ = \ \int_L G(\mathbf{x}_A, \mathbf{x}, -t) \ * \ G(\mathbf{x}_B, \mathbf{x}, t) d\mathbf{x} \ * \ C(t) \ . \tag{3.7}$$

By convolving Equation 3.2 with $C(t)$ the integral in Equation 3.2 can be replaced by the left hand side of Equation 3.7:

$$\{G(\mathbf{x}_B, \mathbf{x}_A, t) \; + \; G(\mathbf{x}_A, \mathbf{x}_B, -t)\} \; * \; C(t) \; \approx \; \frac{2}{\rho c_T} \langle p(\mathbf{x}_A, -t) \; * \; p(\mathbf{x}_B, t) \rangle \; . \quad (3.8)$$

The right–hand side of Equation 3.8 describes the crosscorrelation of ambient noise measured by the receivers A and B on the ground below a moving medium, the atmosphere. According to Equation 3.8, this crosscorrelation is equal to the Green's function from $\mathbf{x}_A$ to $\mathbf{x}_B$ plus the time reversed Green's function from $\mathbf{x}_B$ to $\mathbf{x}_A$, convolved with the autocorrelation of the noise. Equation 3.8 implies that the traveltimes of infrasound between two receivers can be determined by crosscorrelating the ambient noise at these two receivers.

3.3 Modeling of the Infrasound Propagation

From here onward we assume the atmosphere is stratified. There are various approaches modeling infrasound propagation through a stratified atmosphere. These are all based on approximations of the wave equation. One of these methods is based on the parabolic equations [*Lingevitch et al.*, 2002]. Dependent on the spatial and temporal resolution, this approach can easily lead to high computation costs.

A computationally less intensive method uses the raytracing models. Raytracing simplifies the wave equation by deriving the Hamiltonian equations from the Eikonal equation [*Georges*, 1971; *Cowling et al.*, 1971]. The solution of the Hamiltonian equations is a ray, which indicates the path of infrasound. This high-frequency approximation is possible, since the examined wavelengths are small in relation to the stratified profiles of temperature and wind, and the reflecting surfaces [*Blom and Waxler*, 2012]. Examples of such raypaths are shown in Figure 3.2. The raytracing model we implemented solves the Hamiltonian equations numerically with the Runge-Kutta algorithm and uses the effective sound speed approximation. In contrast to existing raytracing models (HARPA [*Jones et al.*, 1986], WASP-3D [*Dessa et al.*, 2005]), which are implemented in spherical coordinates, we implemented the Hamiltonian solver in Cartesian coordinates.

With our raytracing model, it is possible to calculate the raypaths of any emitting angle. However, only rays which connect the sources with the receivers (eigenrays) contribute to the measured pressure. The eigenrays are determined with a least squares approximation of the minimum distance between the receiver and the reflections of the rays on the ground.

While propagating from the source through the atmosphere to the receiver, the infrasound is attenuated and phase shifted. The atmospheric attenuation depends on the frequency of the infrasound and the density of the atmospheric layer. To calculate the atmospheric attenuation, we use the emperical NRLMSISE–00 model (Naval Research Laboratory Mass Spectrometer and Incoherent Scatter radar Exosphere) [*Picone et al.*, 2002]. Figure 3.3 shows an example of the atmospheric attenuation of different frequencies. The infrasound is additionally reduced by the

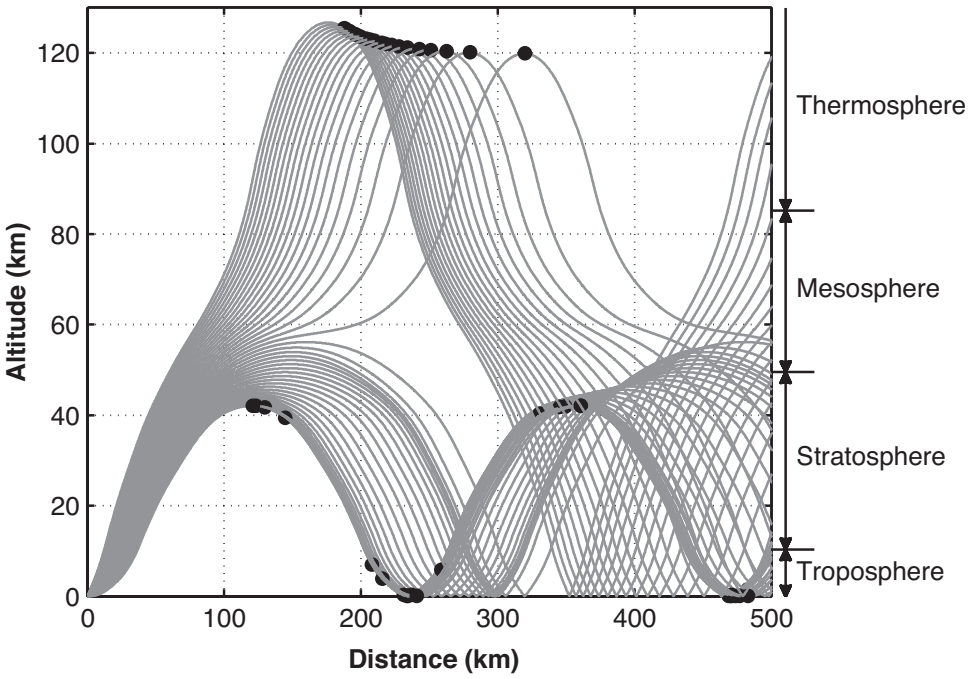


Figure 3.2: *The rays indicate the path of the infrasound though the atmosphere. The black dots indicate the position of caustics.*

geometrical spreading since the sound energy is distributed over a larger area. The spreading can be calculated with the Jacobian matrix which takes into account how the ray coordinates are changing when the emitting angle changes. Figure 3.4 shows an example of geometrical spreading as a function of distance for different emitting angles.

The phase shift depends on caustics. The caustics can be found on the basis of the spreading (Jacobian matrix), since caustics occur when neighboring rays touch (black dots in Figure 3.2). First–order caustics cause a phase shift of 90° of the time dependent pressure . Such caustics are taken into account. In caustics the amplitude prediction by raytracing breaks down, since the spreading becomes zero, which result in non–physical predictions of an infinite amplitude [*Gilmore*, 1993; *Pierce*, 1989]. The time dependent pressure is represented by a source wavelet. The receiver response (also known as barogram) is computed by shifting this wavelet in time and phase, and modifying its amplitude, dependent on the raypath. Two kinds of sources can be generated: blasts and microbaroms. Blast waves occur if a large amount of energy is set free in a small volume (e.g., during an explosion [*Baker*, 1973]), as shown in Figure 3.5.

Ground–truth events like explosions, which would generate blast waves are not always available. If there are no events, the receivers measure ambient noise. In

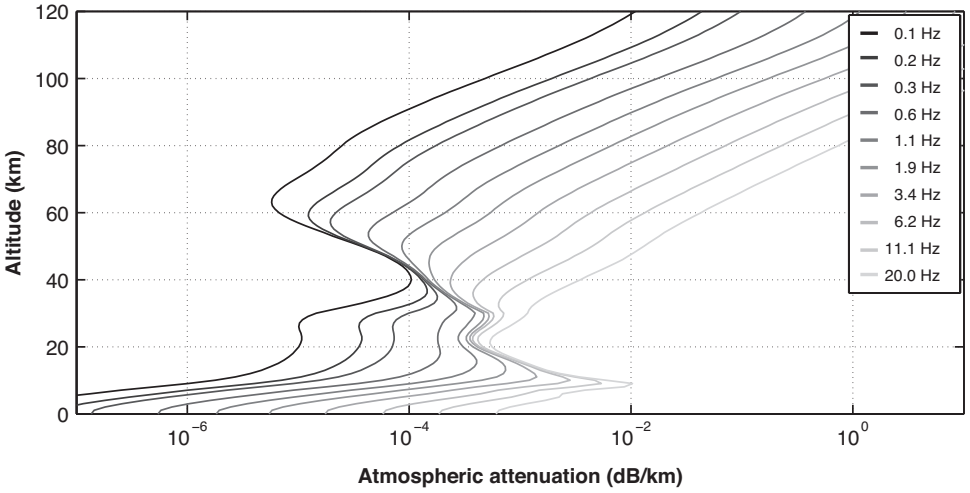


Figure 3.3: *The atmospheric attenuation as a function of altitude for different frequencies [Picone et al., 2002].*

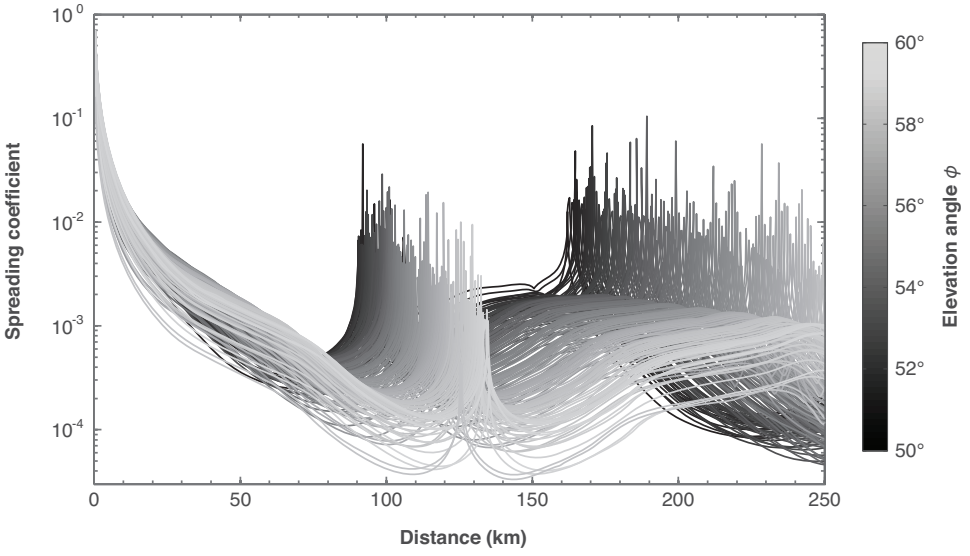


Figure 3.4: *An example of geometrical spreading as a function of distance. The geometrical spreading depends on the initial elevation angle of the raypath. The geometrical spreading coefficient has a peak at the caustics, since the spreading is zero there.*

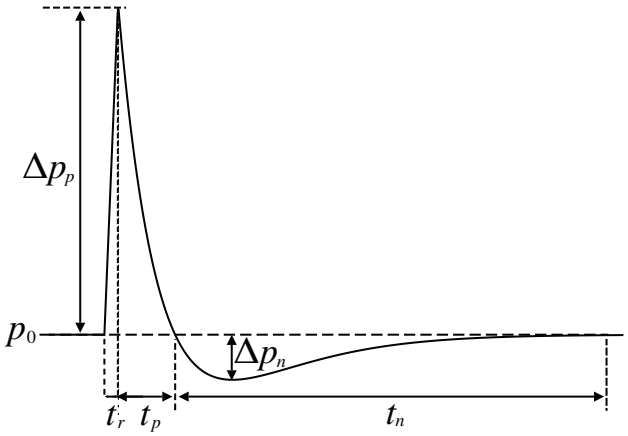


Figure 3.5: *A blast wave: after a negligible rising time (t_r) the pressure decreases from the positive perturbation (Δp_p) during the positive phase (t_p) until it falls under the normal ambient pressure, Δp_n during the negative phase (t_n).*

the past, ambient noise was considered a disturbance and was ignored. Over the last years, noise has moved more into the focus of scientific interest, since it carries information about the medium through which it propagates. Due to wave-wave interactions in the oceans, acoustic energy is generated that couples with the atmosphere [*Brekhovskikh et al.*, 1973; *Waxler and Gilbert*, 2006]. This energy is due to pressure fluctuations in the ocean and due to the compression of the air by the ocean waves. The ambient noise field in the atmosphere mainly consists of such energy, usually referred to as microbaroms. The empirically well determined spectrum of microbaroms lies between 0.1 Hz and 0.5 Hz and has its maximum at 0.2 Hz [*Posmentier*, 1967; *Donn and Naini*, 1973]. Figure 3.6 shows an example of microbaroms, recorded in De Bilt, the Netherlands. Microbaroms can be distinguished from other noise by a strong correlation between different sensors. Note that in this example the sensors are closely spaced and not hundreds of kilometers apart as discussed later in this paper.

3.4 Numerical Experiments

In this section, we apply infrasonic interferometry to responses of two kinds of sources: blasts and microbaroms. In the first experiment, we model blast waves as line source response and the barograms at two receivers. The traveltimes of the eigenrays between these two receivers are determined using crosscorrelation. The example with blast sources provides a better understanding of the results, because the arrivals related to different raypaths are identifiable in the barograms, although this is an unrealistic set up for blast sources. The second experiment deals with

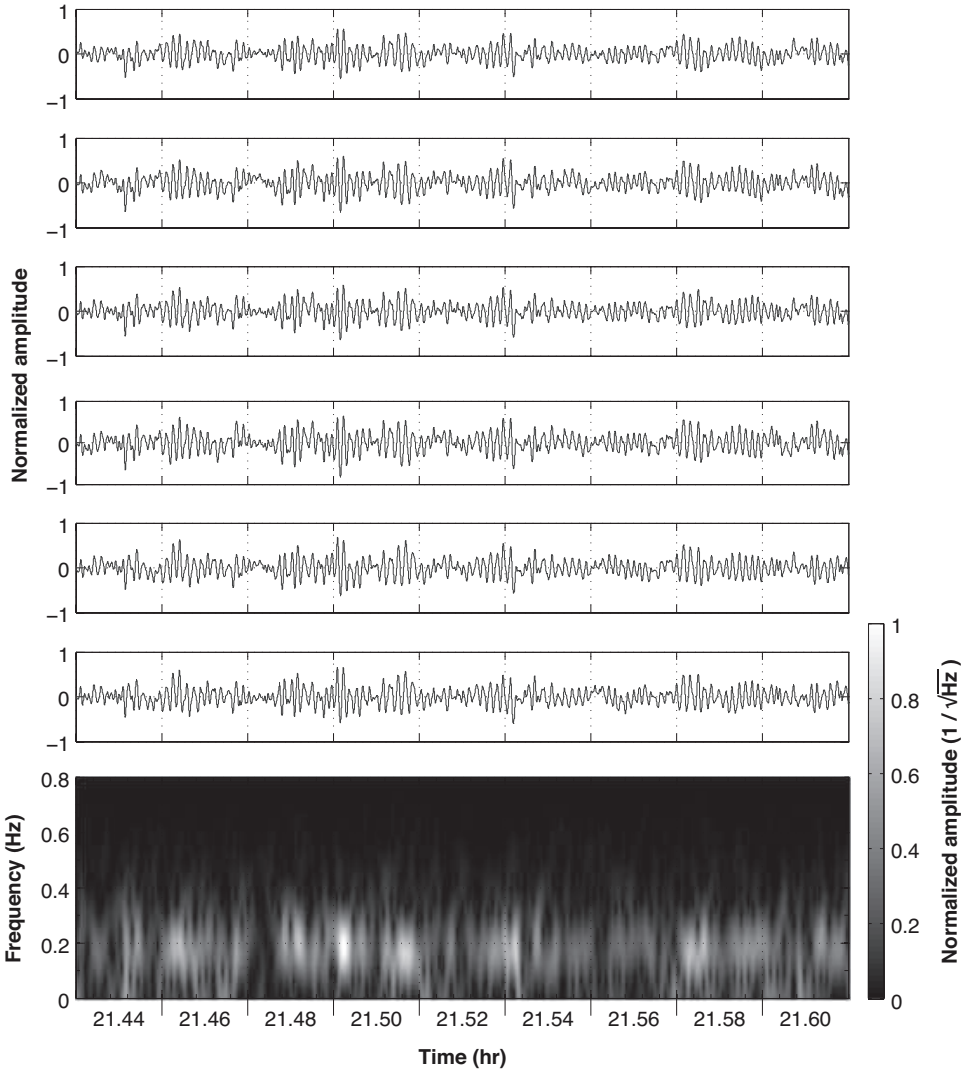


Figure 3.6: *An example of microbaroms and their spectrum, recorded with six array elements in De Bilt, the Netherlands.*

microbaroms emitted from the same source array as in in the previous experiment. Microbaroms are in reality more likely to be encountered simultaneously than blasts.

■ 3.4.1 Numerical Experiment with Blast Waves

Figure 3.7 shows the setup of the numerical experiment. 361 sources, with 0.5 km spacing, are used ranging from $x = -90$ km to $x = +90$ km. Receiver A and receiver B are located at $x_A = 210$ km and $x_B = 430$ km. Note there is only illumination from one side in this setup. However, one-sided illumination suffices to find one of the two Green's function in Equation 3.2. For the calculation of the rays, the velocity profiles in the right–hand side of Figure 3.7 are used.

Curve c shows the velocity dependent on the temperature and curve c_{ef} the effective velocity dependent on temperature and wind. The effective velocity is obtained by adding the velocity c_T (Figure 3.8a) to the projection of the meridional and zonal wind (Figure 3.8b) in the direction of receiver A and B ($c_{ef} = c_T + \vec{u} \cdot \vec{n}$, with $\vec{u}$ the wind vector and $\vec{n}$ the vector which directs from receiver A to receiver B). With these velocity profiles, receiver A measures the infrasound which propagates along the eigenrays in Figure 3.7a. Receiver B is reached by the eigenrays plotted in Figure 3.7b. The color refers to the different source locations. For the eigenrays in Figure 3.7, the synthetic barograms recorded at each receiver are calculated using the raytracing model described in Section 3.3. The result of the two receivers is shown in Figure 3.9 for all sources. In this figure, it can be seen that each source has two eigenrays with two different traveltimes to the receiver. Infrasonic interferometry, given in Equation 3.2, is applied by crosscorrelating the barograms of receiver A and B and summing the result over the sources. Figure 3.10a shows the outcome of the crosscorrelation of each source and Figure 3.10b shows the summation.

In order to evaluate the result of the interferometry in Figure 3.10b, we compare it with the response computed for a blast wave source located at receiver A and measured at receiver B. This is shown in Figure 3.10c, where we can identify two arrivals: one at 755 s and the second one at 780 s. The arrival at 755 s corresponds to the infrasound refracted at an altitude of 30 km, whereas the one at 780 s corresponds to the rays refracted at an altitude of 40 km (see Figure 3.7). These are respectively a fast and slow arrival as also observed by *Kulichkov et al.* [2004]; *Evers and Haak* [2007]. The shape of the arrival at 755 s can be explained by minus the autocorrelation of the blast wavelet (Figure 3.5). The minus-sign is a result of the two caustics on the 30 km refracted raypath, which cause a phase shift of 180°. By comparing Figures 3.10b and 3.10c, we notice that the result of the crosscorrelation has a clear first arrival at 755 s and a weaker second arrival at 780 s. In Figure 3.7b it can be seen that the gradient of the effective velocity c_{ef} for the refraction at an altitude of 30 km is much stronger than for the refraction at an altitude of 40 km. If the velocity gradient is stronger, more energy is refracted. Therefore, far more energy will be refracted for the first arrival than for the second arrival. Including more sources and finding more eigenrays may improve the results.

In Figure 3.10b we also observe several weak events between 730 s – 750 s and 785 s – 805 s, which do not occur in Figure 3.10c. In order to understand these spurious events, we need to have a closer look at Figure 3.10a, where we can see that

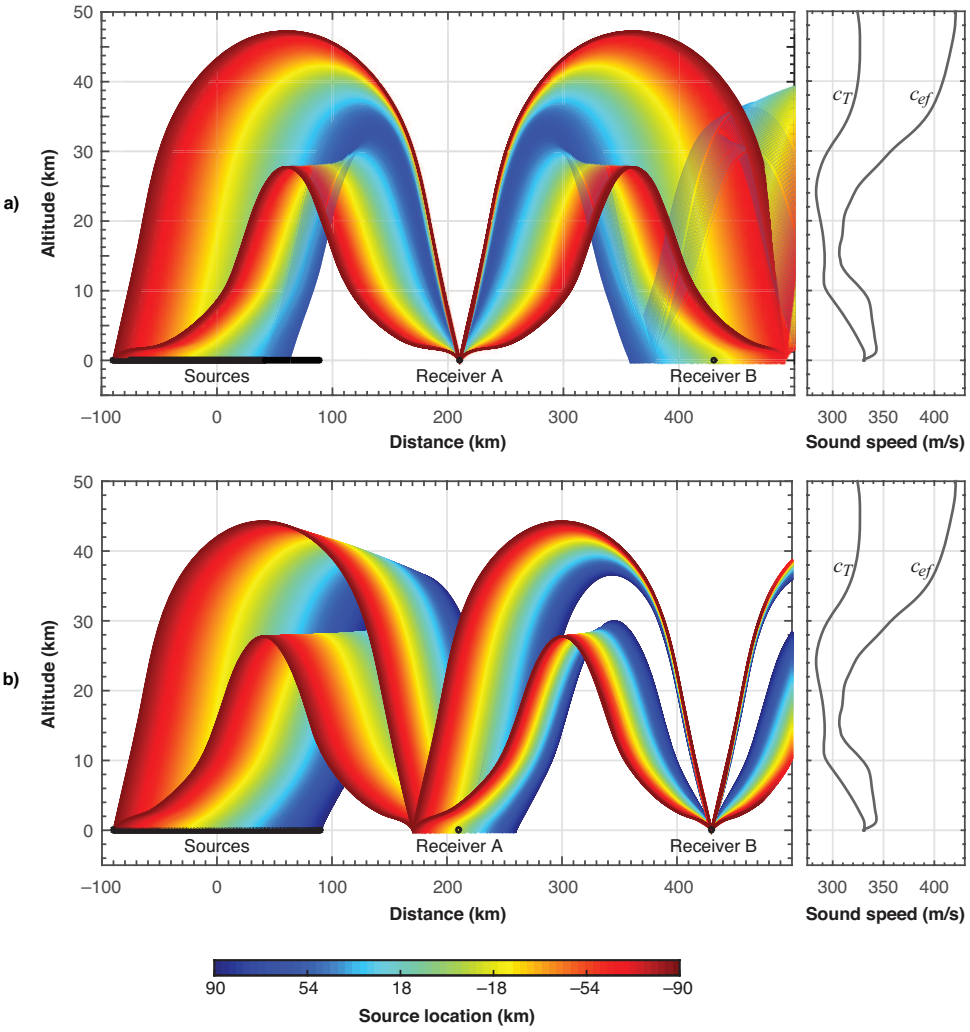


Figure 3.7: *Receiver A (at 210 km) and B (at 430 km) have different eigenrays.* ***a)*** *The eigenrays between receiver A and the 361 sources. The color indicates the source location ranging from $x = -90$ km to $x = +90$ km. Not all eigenrays of receiver A reach receiver B. The sources from $x = +63$ km to $x = +90$ km are in the shadow zone of receiver A and do not contribute eigenrays to receiver A.* ***b)*** *The eigenrays between the sources and receiver B. The corresponding velocity profiles are shown on the right–hand side. Curve c_T shows the temperature dependent velocity and curve c_{ef} the velocity dependent on temperature and wind*

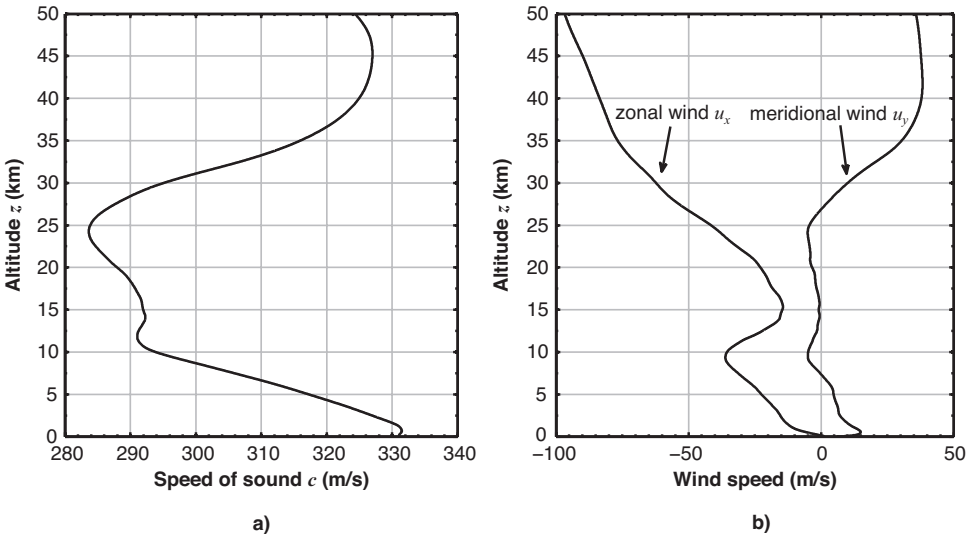


Figure 3.8: *The sound speed profile* **a)** *and the wind profile* **b)** *used for the calculation of the eigenrays in Figure 3.7. The meridional wind is northwardly and the zonal wind eastwardly directed. The effective velocity in Figure 3.7 is an addition of the sound speed and the wind in the direction of the sound.*

they are strongly present for each source. They originate from the crosscorrelation between the two differently refracted raypaths. The spurious event at 730 s – 750 s results from the crosscorrelation of the 40 km refraction at receiver A and the 30 km refraction at receiver B. The spurious event at 785 s – 805 s is the result of the correlation of the 30 km refraction at receiver A and the 40 km refraction at receiver B. After summation, the spurious events are suppressed. The spurious events are not completely canceled out, since the sources of the line array (see Figure 3.7) can not represent all sources on the semi circle L (see Figure 3.1c). More sources may reach a better coverage of the semi circle L.

■ 3.4.2 Numerical Experiment with Microbaroms

For the numerical experiment with microbaroms, the same source – receiver configuration (Figure 3.7) and temperature, wind profiles (Figure 3.8) are used as in the previous experiment. In order to simulate microbaroms, random noise is generated and subsequently filtered between 0.1 Hz and 0.5 Hz. Since each source has a different noise signal, all the sources are uncorrelated. The microbaroms propagate along the same eigenrays as the blast waves (see Figure 3.7). Figures 3.11a and 3.11b show all the microbaroms due to simultaneously acting noise sources that reach receiver A and B, respectively. In this experiment we also apply infrasonic interferometry given in Equation 3.8. In the first step, all microbaroms recorded by

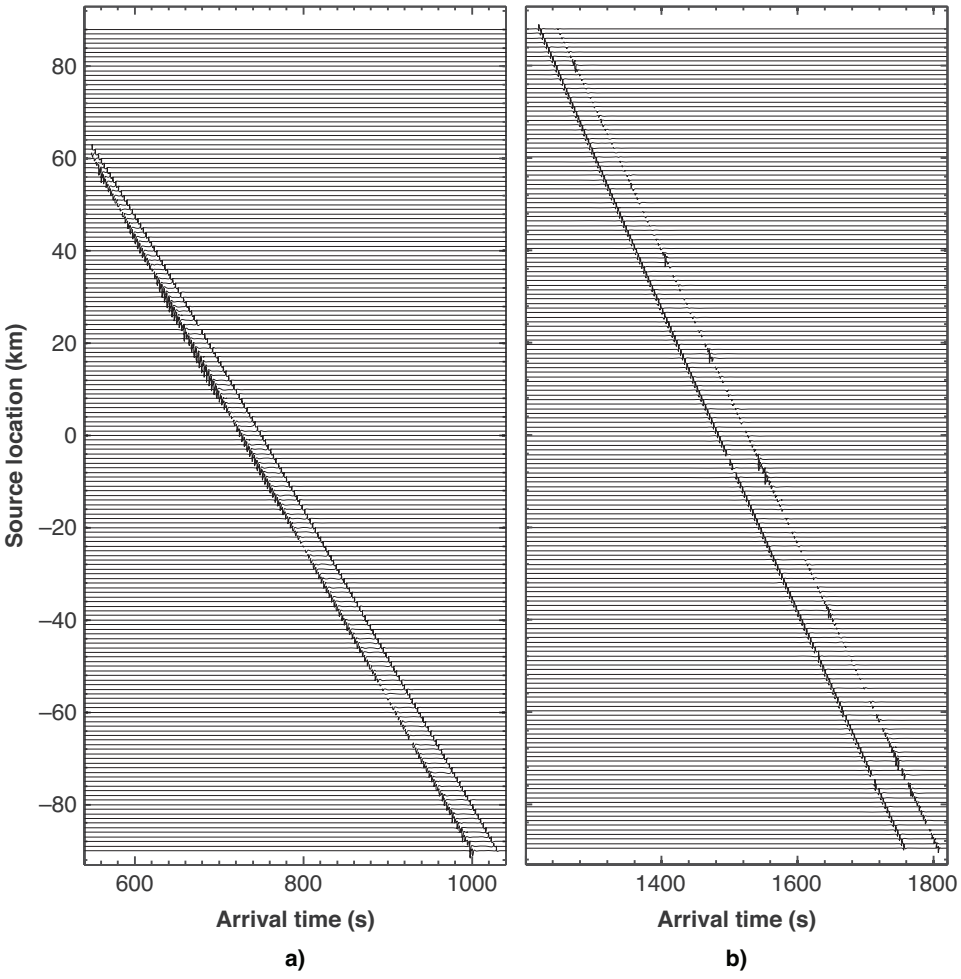


Figure 3.9: *Each blast wave reaches the receiver via an eigenray (see Figure 3.7) with a different traveltime and a different attenuation.* ***a)*** *Barograms of receiver A* ***b)*** *Barograms of receiver B. The amplitude is normalized.*

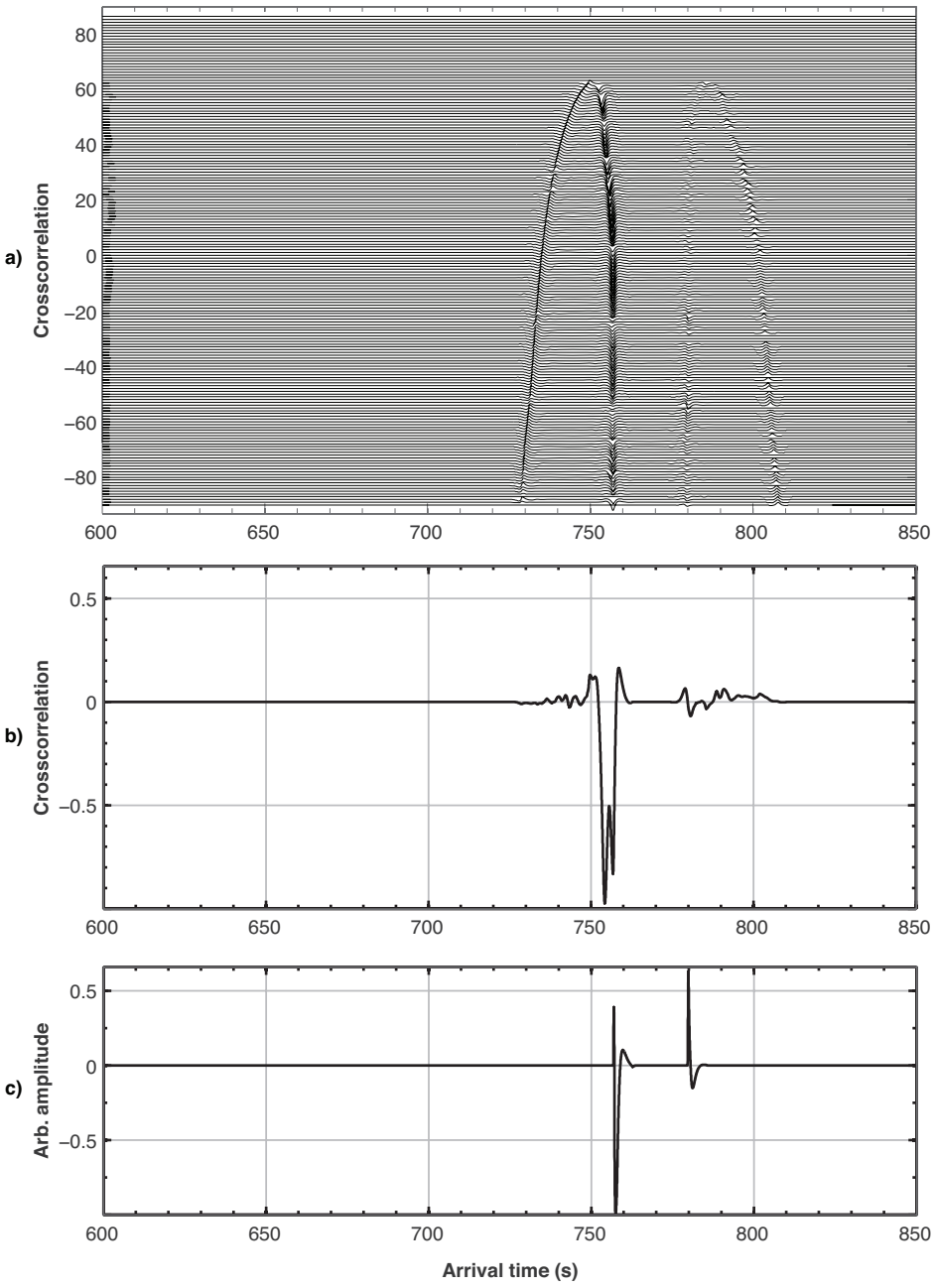


Figure 3.10: ***a)*** *Crosscorrelations between receiver A and receiver B as given by the integrand in Equation 3.2 for each of the 361 source locations.* ***b)*** *The summations of the different crosscorrelations in Figure a.* ***c)*** *The response computed for a blast wave source located at receiver A and measured at receiver B.*

receiver A are summed to obtain the simulated measurement shown in Figure 3.11a bottom. The same procedure is done for receiver B (Figure 3.11b bottom). Note: Figure 3.11 shows only short time windows, selected from a five–hour simulation. In the second step, the simulated measurements of receiver A and B are crosscorrelated. The result, shown in Figure 3.12a, is evaluated in the same way as in the previous numerical experiment. This is done by comparing it with the response computed for a blast wave source located at receiver A and measured at receiver B (Figure 3.12d). In order to find the limits of the crosscorrelation, in practice, we add different noise levels to the microbarom signal predicted at each receiver location. The signal–to–noise–ratio is defined as $SNR = (\frac{S}{N})^2$, with S the root–mean–square of the microbaroms and N the root–mean–square of the added noise. The minimal needed SNR is found by reducing the the SNR stepwise. Figure 3.12b shows the crosscorrelation of simulated data with $SNR = 0.5$ at receiver A and at receiver B $SNR = 0.013$. The SNR at receiver B is lower because the energy has travelled through the stratosphere. In Figure 3.12c the crosscorrelation of simulated measurements with a $SNR = 0.2$ at receiver A and $SNR = 0.005$ at receiver B.

In the result of the crosscorrelation, we observe one clear arrival at 755 s, related to the infrasound refracted at 30 km height. The arrival of the 40 km height refraction is not distinguishable because it is masked by noise. The result of the crosscorrelation could be improved by crosscorrelating longer time windows and including more sources. However a longer time window would have to be based on the assumption of longer constant atmospheric conditions. In the experiment with a SNR of 0.5 we are able to determine the traveltime by crosscorrelation. For a SNR of 0.2 or lower it is hardly possible to resolve the traveltime.

3.5 Conclusions

Through numerical experiments, we have verified the theory of infrasonic interferometry and showed that it can be used to estimate the traveltimes of stratospherically refracted waves. We generated synthetic time signals using a raytracing model and taking into account atmospheric attenuation, geometrical spreading and phase shifts due to caustics. Two types of source wavelets were implemented for the numerical experiments: blast waves and microbaroms. We simulated an array of sources and two receivers, which are each reached by eigenrays refracted at 30 km and 40 km height. In the first experiment with the blast wave, we were able to estimate the traveltime of the 30 km refraction. The traveltime of the second refraction could be found less clearly, since the velocity gradient at 40 km height is smaller. In the experiment with microbaroms, the traveltime of the first arrival was recovered as well, but the traveltime of the second raypath could not be detected, for the same reason. The results could be improved by including more sources. Nevertheless, the traveltime of the 30 km refraction can be well estimated above a signal–noise–ratio of 0.5 using infrasonic interferometry. This shows that microbaroms can be used in practice to obtain the traveltimes of infrasound through the stratosphere. It depends on the wind and temperature profile which parts of the stratosphere are sampled. In the specific case studied here, arrivals from 40 km altitude did not show

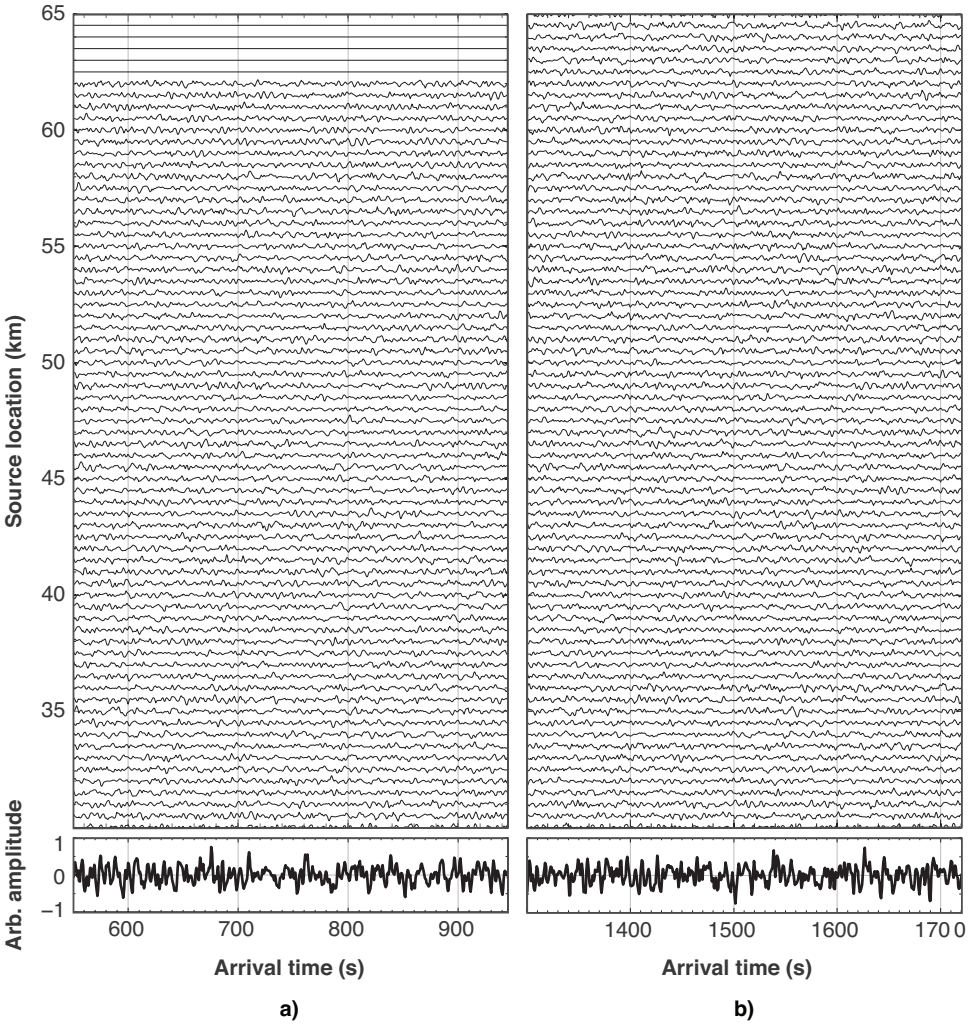


Figure 3.11: *The simulated measurements are obtained by addition of the microbaroms which reach the receivers.* ***a)*** *The microbaroms measured at receiver A.* ***b)*** *The microbaroms measured at receiver B. The figures show a few sources of the simulated 361 sources and a short time window of the simulated five hours.*

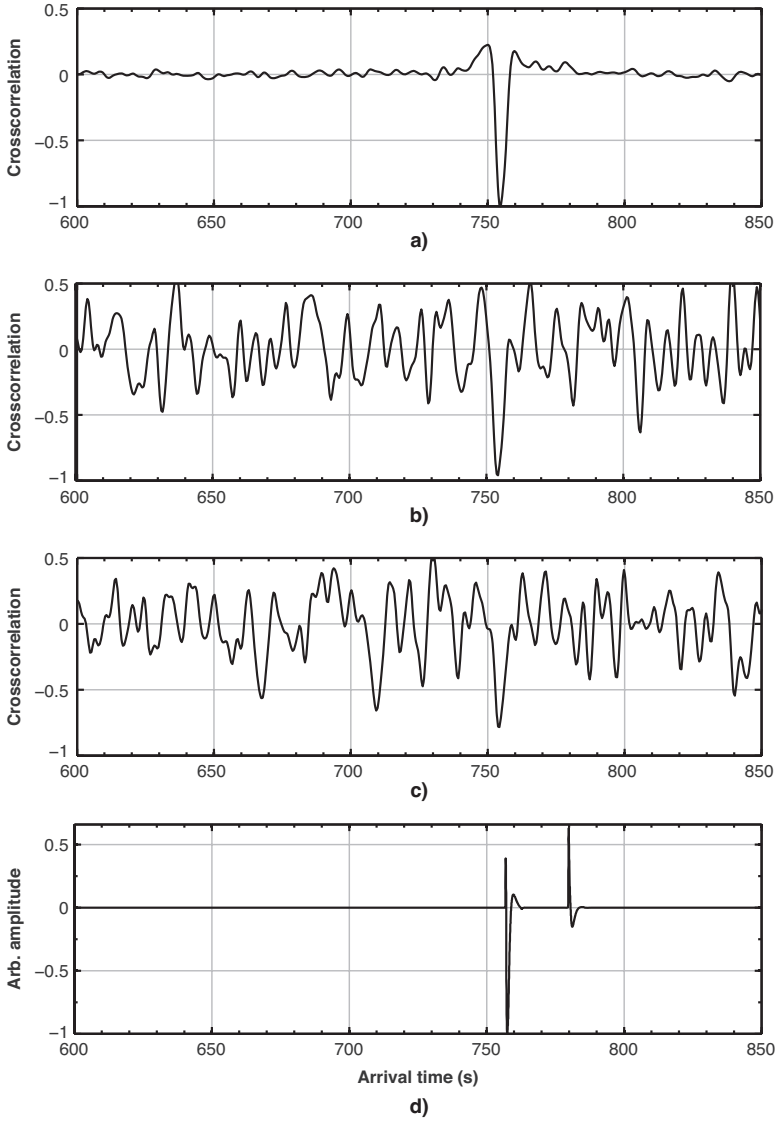


Figure 3.12: ***a)*** *Crosscorrelations of microbaroms as given in Equation 3.8. Five hours of simulated measurements without additional noise (SNR = ∞) of receiver A (Figure 3.11a) and receiver B (Figure 3.11b) are crosscorrelated.* ***b)*** *Crosscorrelation of the same simulated data, but with additional noise (SNR = 0.5 at receiver A and SNR = 0.013 at receiver B).* ***c)*** *Crosscorrelation of the same simulated data with a SNR = 0.2 at receiver A and SNR = 0.005 at receiver B.* ***d)*** *As reference, a blast source at receiver A measured with receiver B.*

up coherently in the crosscorrelation result.

The next step will be the inversion of the traveltimes obtained at many receiver pairs in order to estimate the temperature and wind profiles. For this inversion, the atmospheric conditions of the described raytracing model can be varied. In case the searched temperature and wind profiles are found, the simulated ray propagates from receiver A to B in the estimated traveltime. Therefore, the possible wind and temperature profiles can be estimated in a least squares approximation. A reasonable variation of the atmospheric conditions is based on the empirical orthogonal functions (EOF) [*Williams*, 1997; *Drob et al.*, 2010]. The EOF are obtained by applying a principal component analysis to observations of the atmospheric conditions over several years.

In future, we will apply the proposed methodology to microbaroms, which are measured by the "Large Aperture Infrasound Array" (LAIA). LAIA has been installed by the Royal Netherlands Meteorological Institute (KNMI) in the framework of the radio–astronomical "Low Frequency Array" (LOFAR) initiative.

3.6 Acknowledgments

We thank Philip Blom and Dr. Roger Waxler of the National Center for Physical Acoustics (NCPA) for supporting us with their knowledge about the geometrical spreading. We also thank Dr. Deyan Draganov for sharing his knowledge about the crosscorrelation of microseisms. This research is funded by the 'Netherlands Organization for Scientific Research' (NWO).

4

Infrasonic interferometry applied to microbaroms observed at the Large Aperture Infrasound Array in the Netherlands

Abstract

We present the results of infrasonic interferometry applied to microbaroms, obtained from ambient noise. For this purpose the "Large Aperture Infrasound Array" (LAIA) was used, which has been installed in the Netherlands. Preprocessing appeared to be an essential step in enhancing the microbarom signals from ambient noise that strongly influences the results of the interferometry. Both the state of the atmosphere and the noise characteristics are taken into account to assess the strength of the crosscorrelation. The delay time of the microbaroms between two stations is determined through cross correlating the recordings. By calculating the crosscorrelations between all 55 station pairs of LAIA, we are able to find the delay time of microbaroms up to a interstation distance of 40.6 km. Using the strength of the crosscorrelations, we are able to show that the coherence of the microbaroms along the direction of arrival is higher than orthogonal to it. A comparison of the atmospheric state, with a crosscorrelation, over a period of ten days, reveals that the infrasound propagation over the array is correlated with the tropospheric temper-

Published as: Fricke, J. T., Evers, L. G., Smets, P. S. M., Wapenaar, K., and Simons, D. G. (2014). Infrasonic interferometry applied to microbaroms observed at the Large Aperture Infrasound Array in the Netherlands. J. Geophys. Res. Atmos., 119(16), 9654–9665. Note that minor changes have been introduced to make the text consistent with the other chapters of this thesis.

ature and wind. Based on the crosscorrelations between the three closest stations, we are able to passively estimate the effective sound speed and the wind speed as a function of time.

4.1 Introduction

It has recently been shown that the variability of the (upper) atmosphere can be probed using infrasound. *Le Pichon et al.* [2005] and *Antier et al.* [2007] demonstrated that continuous infrasound monitoring of volcanoes provides means for probing fine–scale wind fluctuations from the ground to the stratosphere. *Lalande et al.* [2012] developed an inverse model to investigate the capability of infrasound observations as a remote sensing technique. Observing the Tungurahua volcano in Ecuador, *Assink et al.* [2012, 2013] showed that infrasonic remote sensing of wind can be applied to the upper atmosphere. Even the effects of small–scale atmospheric gravity wave fluctuations can be found in infrasound measurements as shown by *Drob et al.* [2013]. For the troposphere, *Marcillo and Johnson* [2010] demonstrated that the wind vector can be obtained with three infrasound sensors in the near field of a volcano.

In general, such studies depend on ground truth events, i.e., an explosion or a volcanic eruption. This is a disadvantage because the exact time and location of these events are need to be known. Furthermore, there is only a limited occurrence of such ground–truth events.

Ambient infrasonic noise consists mostly of microbaroms [*Posmentier*, 1967]. These microbaroms result from the nonlinear interaction of oceanic waves and are almost continuously present at a frequency of 0.2 Hz [*Brekhovskikh et al.*, 1973; *Donn and Naini*, 1973]. Atmospheric temperature and wind can be retrieved from microbaroms using infrasonic interferometry, which is based on the theory of non-reciprocal Green's function retrieval by crosscorrelation [*Wapenaar*, 2006; *Godin*, 2006]. This theory determines the outcome of the crosscorrelation of the measured noise field at two receivers A and B in a moving medium. Assuming that the noise field is equipartitioned, this crosscorrelation converges to the Green's function from receiver A to receiver B plus the time–reversed Green's function from receiver B to receiver A, convolved with the autocorrelation of the noise. In other words, the delay times between the two receivers in both directions can be determined by cross correlating the ambient noise at these two receivers. In a study with direct tropospheric waves measured at two locations, *Haney* [2009] has shown that interferometry can be applied to infrasonic ambient noise to retrieve temperature and the strength of winds in the troposphere.

In our recent paper [*Fricke et al.*, 2013], we applied infrasonic interferometry to synthetically generated microbaroms, which were refracted by the stratosphere to gather insight and prove their feasibility for probing the stratosphere. In a recent approach, *Godin et al.* [2014] were able to use traffic noise to estimate the wind vector in the troposphere, showing that the atmosphere can also be probed by ambient noise. Another technique using sound to probe the atmosphere is sonic detection and ranging. Such an active technique can be used to obtain wind and

temperature of the lower atmosphere [*Crescenti*, 1997].

In this paper, we apply infrasonic interferometry to measured microbaroms. We investigate the distance up to which the infrasonic wave of the microbaroms is coherent by calculating the crosscorrelations between all 55 station pairs of the so–called "Large Aperture Infrasound Array" (LAIA) in The Netherlands. LAIA was installed at the site of the radioastronomical "Low Frequency Array" (LOFAR) [*Van Haarlem et al.*, 2013]. The derived delay times are used to estimate the direction of arrival (DOA). Curve fitting of the coherence then gives the sound speed scatter and the scatter of the incident angle. Further, we compare the atmospheric state with the crosscorrelation over a period of ten days. Based on the crosscorrelations between the three closest stations, we estimate the effective sound speed and the wind speed as a function of time.

The structure of this paper is as follows. Section 4.2 begins with a description of the "Large Aperture Infrasound Array" (LAIA) used to measure the ambient noise. Then, Section 4.3 gives an overview of the processing of the ambient noise in order to extract microbaroms and discusses which processing steps are applied to the results of the crosscorrelations. In Section 4.4, we discuss the atmospheric conditions during the time of interest and how microbaroms are generated. In Section 4.5 we investigate the result of the crosscorrelations as a function of interstation distance and time. The first part of this section examines the coherence, while the latter compares the crosscorrelation results with the atmospheric variability. The last part lists the conclusions from this study.

4.2 The Large Aperture Infrasound Array

In the north of the Netherlands the Royal Netherlands Meteorological Institute (KNMI) installed the "Large Aperture Infrasound Array" (LAIA), which consists of 11 infrasound receivers (microbarometers) and has an aperture of 82.6 km with its center at 52.91°N and 6.87°E (cf. Figure 4.1).

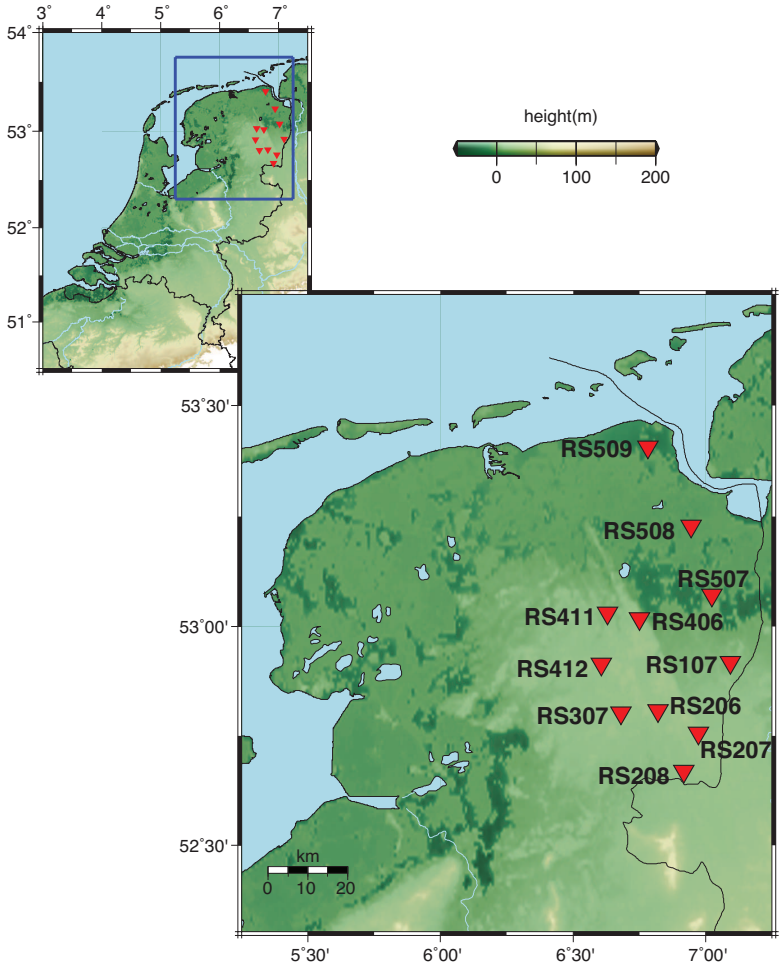


Figure 4.1: *The Large Aperture Infrasound Array (LAIA) in the north of the Netherlands (52.91° N 6.87° E) consists of 11 microbarometers and has an aperture of 82.6 km.*

The array can be characterized through a plot of the interstation distance versus the interstation orientation (cf. Figure 4.2). The orientation of the station combination is expressed as an azimuth angle. An angle of 0° (or 180°) indicates a north–south orientation and 90° (or 270°) an east–west orientation. Each station pair is orientated in two opposite directions. To avoid redundancy, Figure 4.2 presents only the angles from 0° to 180°. According to Figure 4.2 the interstation distances and orientations are well distributed, which avoids spatial aliasing [*Haubrich*, 1968].

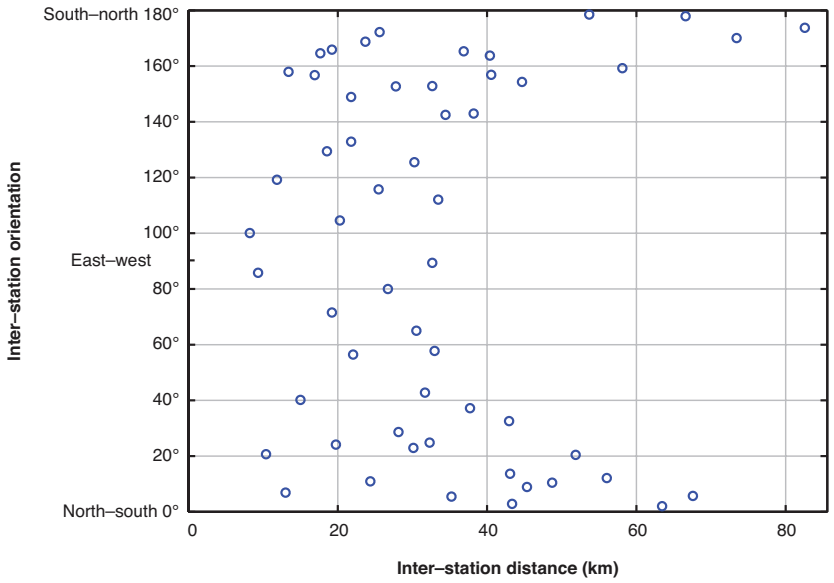


Figure 4.2: *The interstation distance versus the interstation orientation of all possible station combinations of the Large Aperture Infrasound Array (LAIA). An angle of 0° indicates a north–south orientation and 90° an east–west orientation.*

The in–house developed microbarometers are able to measure infrasound up to a period of 1000 s with a sensitivity from 1 mPa up to tens of pascals. The period of 1000 s lies in the acoustic–gravity wave regime [*Mentink and Evers*, 2011]. The analog signal is digitized by a 24 bit A/D converter with a sample rate of 40 Hz. Each microbarometer is equipped with six porous hoses in a star–like configuration with a diameter of 10 m. This layout realizes analog noise reduction by spatial sampling. Because noise is mostly caused by wind, which has a small coherence length, it cancels out over the area of the spatial sampling. The signal of interest, i.e., the infrasonic wave, has a much larger wavelength and is not affected by the noise reducer.

4.3 Processing of Microbaroms and Crosscorrelations

The microbaroms occur around 0.2 Hz and have amplitudes at the receiver of order of 0.1 Pa. Amplitudes of transients are often larger; for instance, sonic booms in the far field have amplitudes of up to 10 Pa. There are several methods known from seismic interferometry to suppress such disturbances [*Bensen et al.*, 2007]. In this section, we describe how we tailored these methods to infrasonic interferometry.

In the first processing step, the raw data are band–pass filtered in order to remove pressure fluctuations caused by wind and sources with frequencies outside of the microbarom band. Figure 4.3 shows an unfiltered (Figure 4.3a) and a band–pass filtered (Figure 4.3b) spectrogram of a recording. We used a second order Butterworth band–pass filter with corner frequencies from 0.05 Hz to 0.3 Hz. The peak around 0.2 Hz is caused by microbaroms.

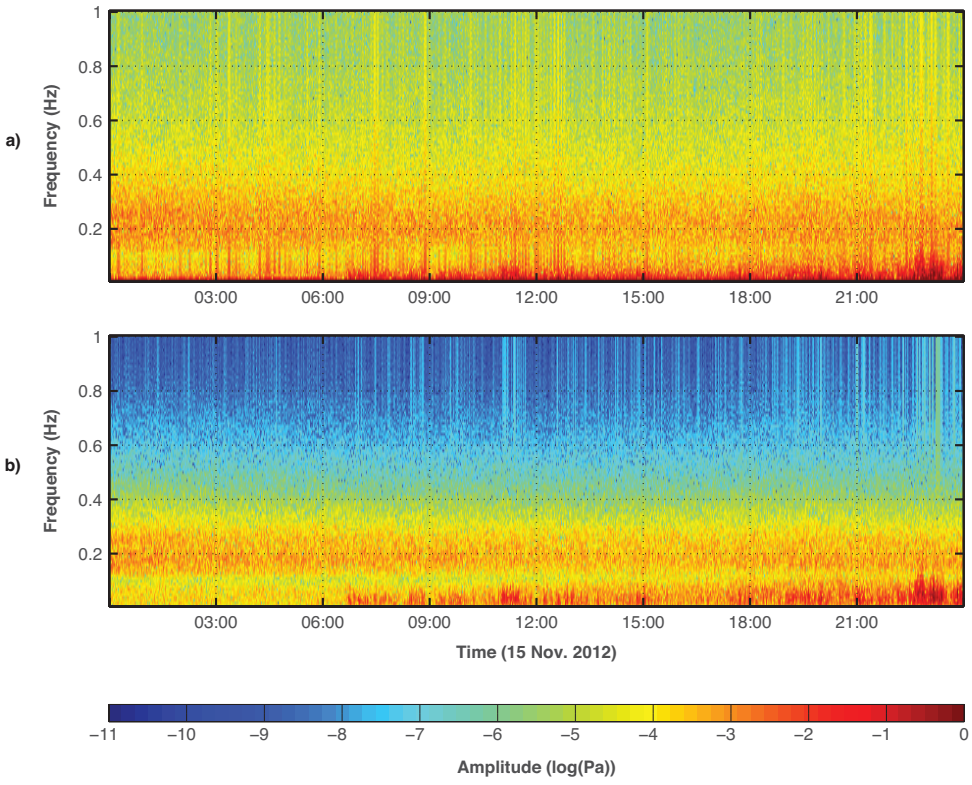


Figure 4.3: *Spectrogram of a* ***a)*** *recording unfiltered and* ***b)*** *band–pass filtered. The peak around 0.2 Hz is caused by microbaroms.*

Figure 4.4a shows the crosscorrelations of band–pass filtered data recorded at stations RS206 and RS412 over ten days. We chose these two stations since they lie along the expected direction of arrival (DOA) [*Evers and Haak*, 2001; *Kedar et al.*, 2008]. The data were split into moving time windows of 3 h, which had an overlap of 98% ($\approx$ 2:56 h) to enhance the resolution. Figure 4.4a shows a distinct change in character between 18 November 2012 and 19 November 2012 as well as just after 24 November 2012. These are periods in time, when there is less wind noise. In Figure 4.4a the microbaroms can be found as a strong peak (red spot) in the crosscorrelation on 15 November 2012 around 18:00h, at a delay time of around 55 s.

The determined delay time of 55 s is reasonable for a direct path of 18.5 km, which is the distance between the recording stations RS206 and RS412. We used this known microbarom peak as a reference for determining the processing parameters in a trial and error approach. The performance of the parameters is determined by the sharpness of the peak, which can be measured by the signal–to–noise ratio (SNR). All processing steps were applied to the raw data before crosscorrelation in order to maximize the quality of the microbarom peak obtained after crosscorrelation.

Using this approach, we found the mentioned corner frequencies (0.05 Hz and 0.3 Hz) of the band pass. Next, we determined the settings for temporal normalization and spectral normalization (i.e., whitening) by trial and error. The temporal normalization raises weak signals of microbarom sources and reduces strong signals of transients like wind and blasts. It calculates the root–mean–square (RMS) of the data in a time window of a certain length and divides the sample in the center of the window by the obtained RMS. By trial and error, we found an optimal window length of 46 s. The spectral normalization flattens the spectrum of the recording. This also amplifies microbaroms by raising weak frequencies, whereas strong monochromatic disturbances are suppressed. We found a whitening band from 0.03 Hz to 0.21 Hz and a cosine taper applied to the ends of the spectra to result in the highest SNR. The cosine taper gives a smooth transition between these corner frequencies and the cutoff frequencies (0 Hz and 0.34 Hz). Figure 4.4b shows the crosscorrelations of the fully processed recordings of RS206 with RS412, using the parameters listed above for the band–pass, temporal, and spectral normalization. The normalized result of the crosscorrelation (Figure 4.4c) emphasizes the development of the delay time over several days.

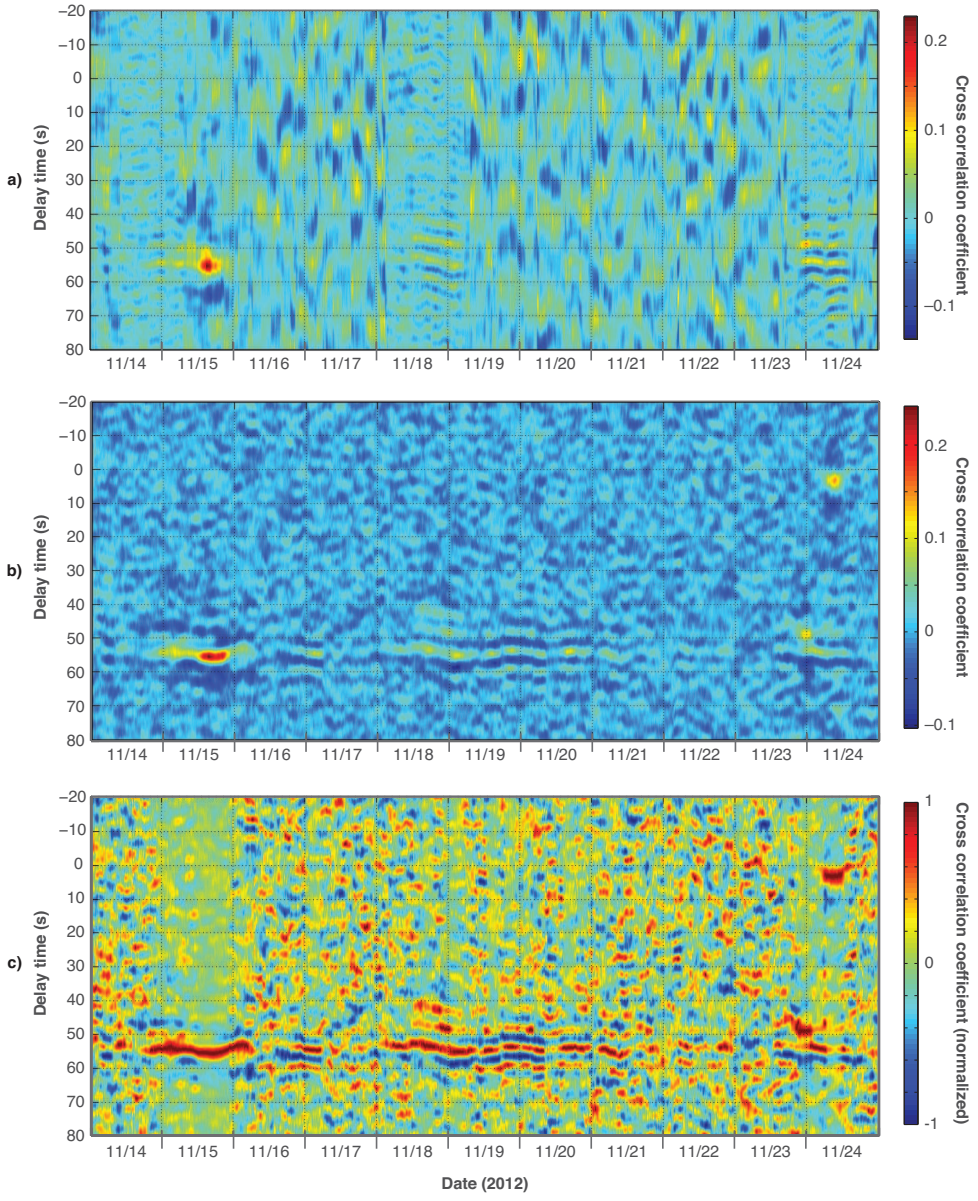


Figure 4.4: ***a)*** *The crosscorrelations of band–pass filtered data of ten days, split into three hour windows. The microbaroms can be found as a peak (red spot) on 15 November 2012. The data were recorded at the stations RS206 and RS412 of LAIA.* ***b)*** *The crosscorrelation of fully processed data after band–pass, temporal, and spectral normalization.* ***c)*** *Normalized result of the crosscorrelation.*

4.4 State of the Atmosphere and Microbarom Sources

In the previous section we described how we found microbaroms for the period between 14 November and 24 November 2012. In this section we describe the influence of atmospheric conditions on the infrasound propagation during these ten days and how we model the microbarom sources in simulations.

■ 4.4.1 Atmospheric Conditions

Figure 4.5 shows the atmospheric specifications (4 times per day) of the operational analysis high–resolution model (ECMWF HRES) provided by the European Centre for Medium–Range Weather Forecasts. This includes the zonal wind, the meridional wind, and the temperature above the array (52.8°N, 6.7°E, grid node).

Gossard and Hooke [1975] described the influence of the atmospheric conditions on the infrasound propagation with the following equation:

$$c_{ef}(z) = \sqrt{\gamma R_s T(z)} + \hat{n}_{DOA} \cdot \vec{u}(z) \tag{4.1}$$

where $c_{ef}(z)$ is the effective sound speed dependent on the altitude z, γ is the ratio of specific heats, R_s is the gas constant, $T(z)$ is the temperature in Kelvin, $\hat{n}_{DOA}$ is the direction of the sound propagation, and $\vec{u}(z)$ is the wind vector. The first term of this equation describes the influence of the adiabatic sound speed ($c_T(z) = \sqrt{\gamma R_s T(z)}$) and can be calculated using $\gamma R_s = 402.8\ \mathrm{m^2 s^{-2} K^{-1}}$. The second term describes the influence of the wind on the effective sound speed and is a projection of the wind in the direction of the sound propagation. We describe in Section 4.5.1 how the direction of arrival (DOA) is determined.

For the ten days shown, there is a strong zonal wind in the stratosphere. This zonal wind is caused by the circumpolar vortex, which is directed eastward in a regular Northern Hemisphere winter. Sudden stratospheric warmings can change the direction and strength of the polar vortex [*Rind and Donn*, 1978; *Evers and Siegmund*, 2009]. At 10 km altitude we find the jet stream, which is more variable due to Rossby wave activity [*Holton*, 2004]. The increase in temperature in the stratosphere is caused by the ozone layer, which absorbs solar radiation. This increase will lead to an increase in $c_{ef}(z)$ (see Equation 4.1), enabling the ducting of infrasound between the Earth's surface and the stratopause. In general, the zonal wind is stronger than the meridional wind.

■ 4.4.2 Microbarom Sources

Large energetic systems of ocean waves, e.g., marine storms, hurricanes, and high–amplitude long–period ocean swell, radiate acoustic energy almost continually into both the ocean and the atmosphere [*Longuet-Higgins*, 1950; *Brekhovskikh et al.*, 1973]. The ocean component can couple to the ocean floor, radiating seismic energy into the solid Earth [*Gutenberg*, 1939; *Donn and Naini*, 1973]. The atmospheric component is referred to as microbaroms, whereas the seismic component is known as microseisms. Ocean surface wave interaction can cause second–order pressure oscillations, generating almost continuously coherent ambient noise at twice the ocean

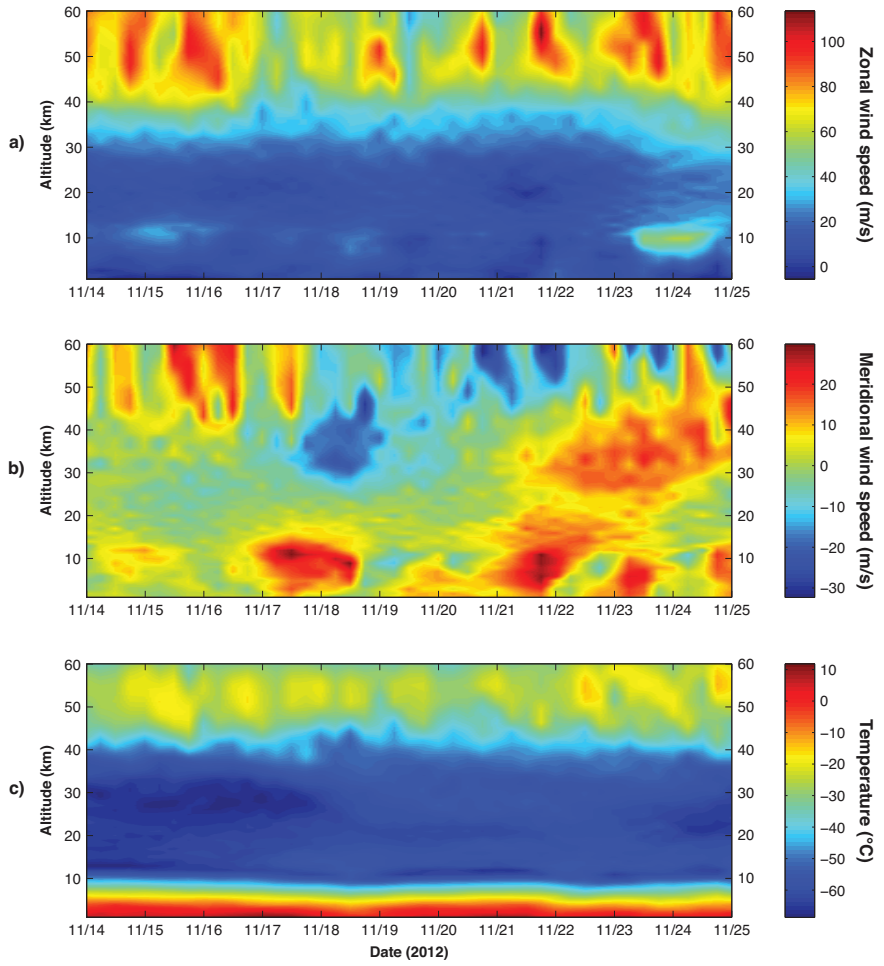


Figure 4.5: *The atmospheric specifications (four times per day) of the European Centre for Medium–Range Weather Forecasts (ECMWF) operational analysis high–resolution (HRES) model. This includes* ***a)*** *the zonal wind,* ***b)*** *the meridional wind, and* ***c)*** *the temperature above the array (52.8° N, 6.7° E grid nodes ECMWF).*

surface wave frequency [*Longuet-Higgins*, 1950; *Hasselmann*, 1963]. Microbarom signals are well characterized by a radiation frequency of 0.2 ± 0.1 Hz. Microbarom radiation can be fully modeled a two–fluid model, over air and seawater, and a sea–state model [*Waxler and Gilbert*, 2006]. Column resonance is allowed assuming an elastic seafloor, taken into account the bathymetry [*Waxler et al.*, 2007]. The *Waxler and Gilbert* [2006] source model is validated by *Walker* [2012] and *Stopa et al.* [2012], studying ambient swell and hurricane–induced microbaroms, respectively. The ECMWF high–resolution Wave Atmosphere Model (WAM) is used as

sea–state model for microbarom modeling (model cycle 38r1, June 2012). The WAM model is coupled to the ECMWF HRES model, important for microbarom simulations. It is an analysis model, consisting of both model data and assimilated buoy and satellite data. The sea–state is described by the 2–D wave spectra (2DFD), consisting of 36 frequencies and directions. Integration of the wave spectrum over direction and frequency results in the significant wave height for each longitude and latitude. Wave periods range from approximately 30 s down to 1 s, logarithmically spaced ($T_0/T_n = 1.1^{n-1}$), with a horizontal resolution of 0.25°. Model runs are available every 6 h, globally, with latitudes up to 85°. Applying the *Waxler and Gilbert* [2006] microbarom source model with bathymetry on ECMWF ocean wave spectra results in an energetic microbarom source region located around Iceland for the entire ten day period. A map of the microbarom activity on 15 November 2012 is shown in Figure 4.6.

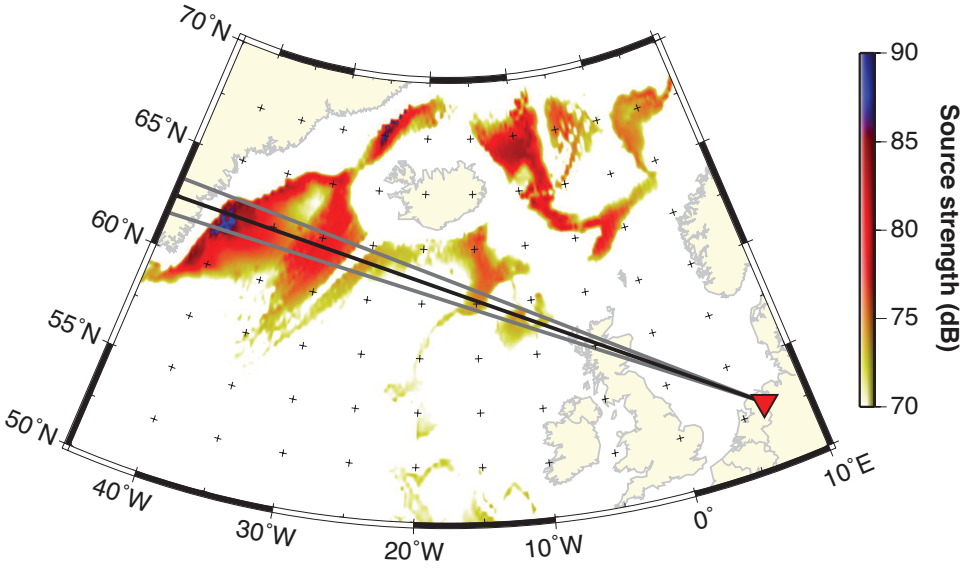


Figure 4.6: *A map of the microbarom activity on 15 November 2012. Color coded is the microbarom source intensity for 0.05 Hz to 0.34 Hz, applying the Waxler and Gilbert [2006] model including bathymetry [Waxler et al., 2007]. Ocean and weather data are obtained from the European Centre for Medium–Range Weather Forecasts (ECMWF). The black line shows the direction of arrival (DOA) for microbaroms of* 310° *and is calculated in a least squares estimation. The gray lines illustrate the angular scatter of* $\pm 1.3°$ *(see Section 4.5.1).*

4.5 Retrieving Parameters of Infrasound Propagation and the Atmosphere

■ 4.5.1 Crosscorrelation and Coherence as a Function of Distance

After the optimization of the processing parameters, we determined the direction of arrival (DOA) and the maximum interstation distance for which the delay time can still be obtained by crosscorrelation. For this purpose, we calculated the crosscorrelations between all 55 possible station pairs of LAIA.

The left column of Figure 4.7 shows the crosscorrelations of six selected station pairs in order of increasing distance. On the right, the orientation of the pair is shown (0° is north, and 90° is east). For distances over 40.6 km it becomes more difficult to identify the delay time in the crosscorrelation, since there are several peaks. All 39 crosscorrelations over smaller distances provide microbarom delay times (cf. Figure 4.13 in the supporting information).

Under the plane wave assumption, we are able to calculate the direction of arrival (DOA) in a least squares estimation using the 39 obtained delay times. Figure 4.6 shows the estimated DOA of 310° for the microbarom peak on 15 November 2012. It points to the northern Atlantic Ocean, a known source of microbaroms [*Evers and Haak*, 2001; *Kedar et al.*, 2008]. This direction also corresponds to region of microbarom sources found in the simulations of the microbarom source model (cf. Section 4.4.2) indicated by the colors in Figure 4.6. On 15 November this direction dominates the results of the crosscorrelations and the contribution of sources from other direction is negligible. The strongest crosscorrelation is achieved between RS206 and RS412 (Figure 4.7c) at 18.5 km. It is remarkable that the crosscorrelation at 18.5 km is stronger than all crosscorrelations of smaller distances (see Figures 4.7a and 4.7b). By examining the direction, we find that the orientation of RS206 – RS412 is closest to the DOA. As an additional verification of the DOA we modeled the microbarom propagation with a ray tracer. The ray tracing model takes temperature and wind profiles of 15 November into account. These profiles are calculated in a three–dimensional interpolation from data provided by ECMWF (see Section 4.4). Figure 4.8 shows the simulated raypaths along the back azimuth plane of 310° obtained by a backward simulation from the array to the microbarom sources. The paths indicate that the receivers of LAIA were reached by microbaroms which were first refracted in the stratosphere and then propagated in the troposphere. The tropospheric rays in this figure have elevation angles between 0° and 9° from the horizontal.

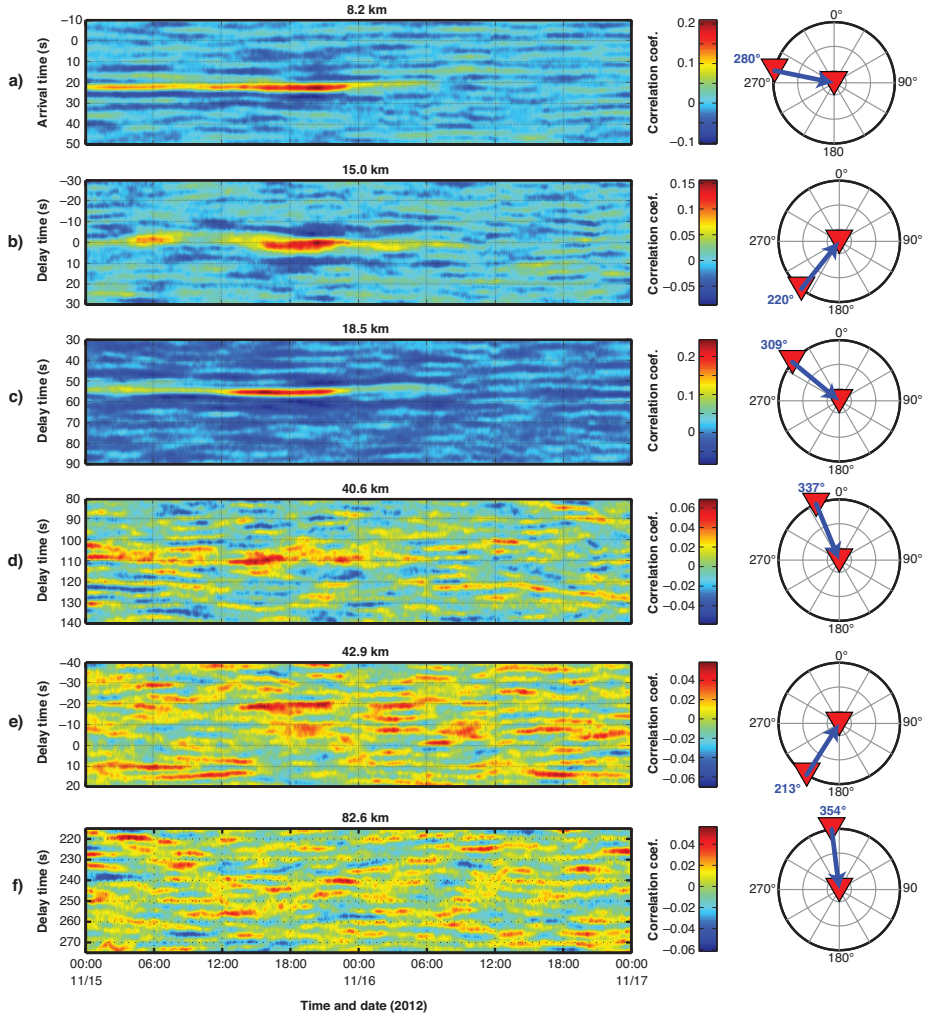


Figure 4.7: a–f) *The left–hand side shows the crosscorrelations of six selected station pairs in order of increasing distance. On the right the orientation of the pair is shown (0° is north, and 90° is east). The crosscorrelation of the smallest interstation distance (8.2 km, stations RS406 – RS411) is shown in Figure 4.7a. The strongest crosscorrelation between RS206 and RS412 is shown in Figure 4.7c. 40.6 km is the maximal distance at which we still obtain a clear peak in the crosscorrelation (RS507 – RS509) is shown in Figure 4.7d. The crosscorrelation of the largest interstation distance (82.6 km, RS208 – RS509) is shown in Figure 4.7f.*

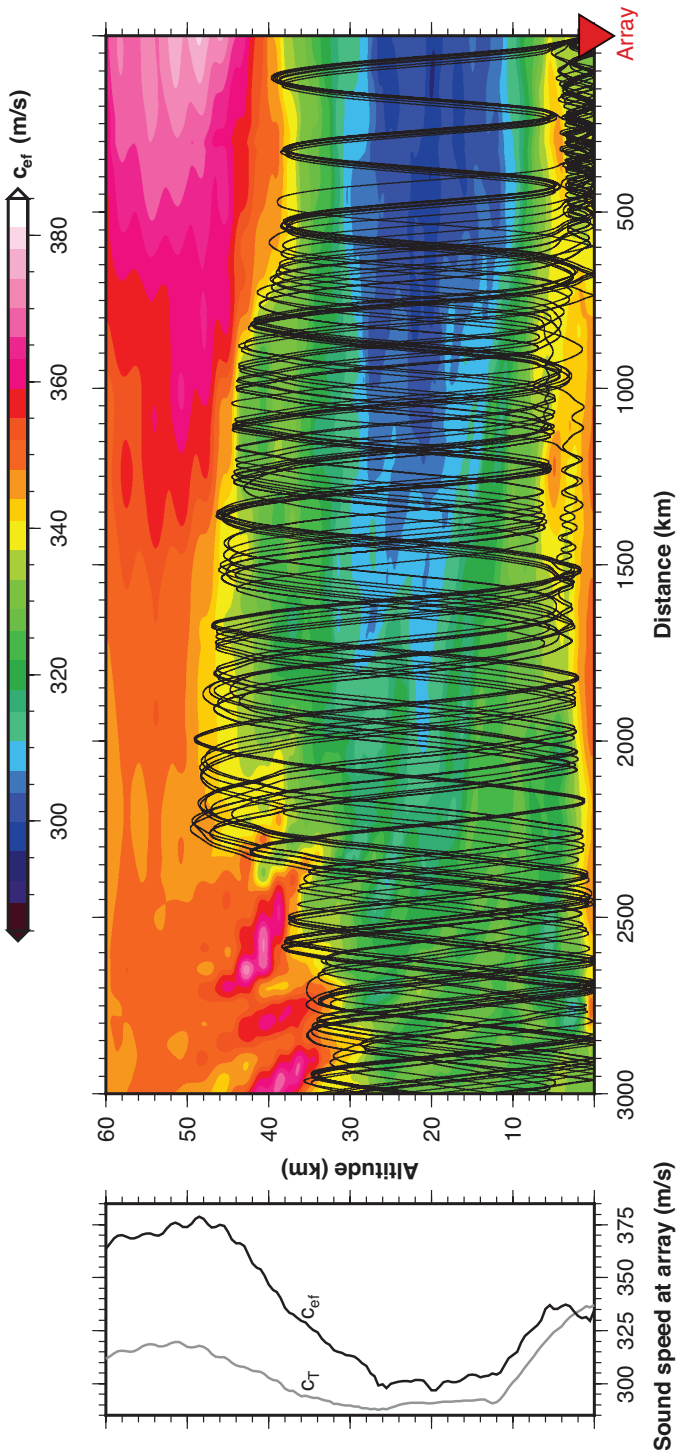


Figure 4.8: ***a)*** *Speed of sound $c_T(z)$ and effective sound speed $c_{ef}(z)$ at the center of LAIA (52.91° N 6.87° E).* ***b)*** *The atmospheric trajectories generated by a ray tracer for a back azimuth of 310°. The ray tracing model takes temperature and wind profiles of 15 November 2012 into account. Temperature and wind profiles are calculated in a three–dimensional interpolation from data provided by ECMWF (see Section 4.4). The paths indicate that the receivers of LAIA were reached by microbaroms which were first refracted in the stratosphere and then propagated tropospherically.*

Next, we study the influence of the station orientation on the coherence. Figure 4.9 shows the magnitude square coherence calculated for the station pairs on 15 November 2012, for the three hour window from 14:52h till 17:52h. We chose this time window, because it contains the strongest peak (see Figure 4.4). The coherence (msc_{xy}) was calculated using a Hanning smoothing window of 18 min and the following equation [*Mack and Flinn*, 1971]:

$$msc^2_{xy}(f) \;=\; \frac{\left|G_{xy}(f)\right|^2}{G_x(f)G_y(f)}\;, \tag{4.2}$$

where $G_x(f)$ and $G_y(f)$ are the autopower spectra and $G_{xy}(f)$ is the cross–power spectrum of the station pair. The recordings of the stations were band–pass filtered (0.05 Hz – 0.21 Hz) and temporal normalized (window length of 2.43 s) before the spectra were calculated (see Section 4.3). Figure 4.9 shows the coherence of a spectral peak at 0.19 Hz. We split the coherencies into two groups according to the direction of the station pair. Group A (dots) consists of all station pairs which are oriented parallel to the DOA within ±22° (288° – 332°), while to group B (triangles) belong all station pairs which are oriented orthogonal to the DOA within ±22° (198° – 242°). All other pairs were disregarded. Figure 4.9 shows that the strength of the coherencies in group B diminishes more rapidly with increasing distance than in group A. *Mack and Flinn* [1971] have described this relation between distance, direction, and spatial coherence for acoustic–gravity waves with a period between 10 s and 100 s (Equation 4.3). According to *Mack and Flinn* [1971], the loss of coherence along the DOA (red curve in Figure 4.9) results from scattering and mode superposition, and the loss of coherence orthogonal to the DOA (green curve) is an effect of scattered waves which reach the stations from a range of azimuths:

$$\varepsilon^2(\vec{r},f) \;=\; \left|\frac{\sin(2\pi k_0 x \sin\Delta\theta)}{2\pi k_0 x \sin\Delta\theta}\right|^2 \left|\frac{\sin(2\pi\Delta k y)}{2\pi\Delta k y}\right|^2, \tag{4.3}$$

where ε is a measure of the spatial coherence, f is the frequency, and $\vec{r}$ is the distance vector between the stations, which consists of the components x (orthogonal to DOA) and y (parallel to DOA). We assume the wave number k_0 to be $0.497\,\mathrm{km}^{-1}$ (with the frequency $f = 0.19\,\mathrm{Hz}$ and the effective sound speed $c_{ef} = 342\,\mathrm{m/s}$). The angular scatter is $\Delta\theta$, and Δk is a measure of the sound speed scatter Δc ($k_0 \pm \Delta k = \frac{f}{c_{ef} \mp \Delta c}$). The term to the right of the product in Equation 4.3 describes the coherence of group A, since the distances in x direction of these station pairs are negligible ($x \approx 0$). The term to the left describes the spatial coherence of group B ($y \approx 0$). By varying the angular scatter $\Delta\theta$ and the sound speed scatter Δc, we can estimate the two curves in Figure 4.9. The red curve in Figure 4.9 is valid for sound speed scatter of $\Delta c = \pm 5.9\,\mathrm{m/s}$ and the green curve for an angular scatter of $\Delta\theta = \pm 1.7°$. The angular scatter corresponds to the accuracy of the DOA estimation (see gray lines in Figure 4.6). The velocity scatter corresponds to the accuracy of the sound speed and the wind speed estimation in the next section.

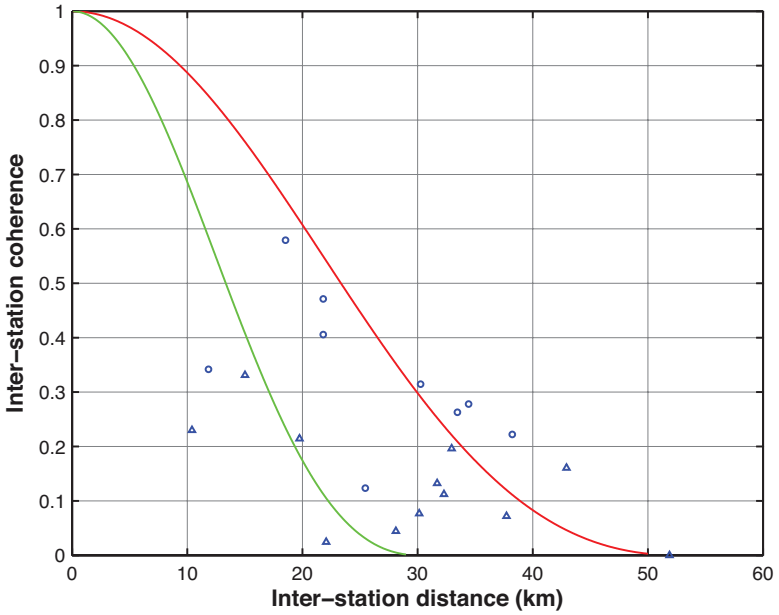


Figure 4.9: *The interstation coherence sorted into two groups dependent on the direction of the station pair. In group A (dots) are all station pairs which are oriented parallel to the direction of arrival within ±22° (288°–332°). Group B (triangles) contains all station pairs which are oriented orthogonal to the direction of arrival within ±22° (198°–242°). The red curve is valid for sound speed scatter of $\Delta c = \pm 5.9\,m/s$ and the green curve for a angular scatter of $\Delta\theta = \pm 1.7°$.*

■ 4.5.2 Crosscorrelation and Atmospheric Variability as a Function of Time

In this section, we investigate whether a relation between the result of the crosscorrelation (Figure 4.4) and the atmospheric conditions (Figure 4.5) can be found.

Overall, we observed a decrease of the crosscorrelation strength with a strong meridional wind in the lower atmosphere (<10 km). This can be explained by the higher noise levels.

Figure 4.10a shows the crosscorrelation of the station pair RS206 and RS412. This is the strongest crosscorrelation of all station combinations (see Section 4.5.1). As a reference, the white curve shows the adiabatic sound speed $c_{T,0}$ close to the two stations, which is calculated using surface temperature T measured by the KNMI. To take the influence of the wind into account, we projected the wind speed $\vec{u}$ in the DOA $\hat{n}_{DOA}$ and added it to the adiabatic sound speed $c_{T,0}$ (see Equation 4.1). Figure 4.10b shows the wind speed with black dots for the ground level and gray dots for the stratosphere at 39 km. Our numerical experiments with the ray tracer described in Section 4.5.1 (Figure 4.8) found this altitude to be dominant in the

refraction of microbaroms, urging an investigation of the stratospheric layer at a height of 39 km for influence on the propagation over the array. The corresponding wind direction is shown in Figure 4.10c (0° is north; 90° is east). The stratospheric wind speed and direction are provided by the ECMWF (see Section 4.4) and the tropospheric wind speed and direction are measured by the KNMI. In Section 4.5.1 we obtained 310° as the DOA of the microbaroms (red line in Figure 4.10c), which is used for the projection of the wind.

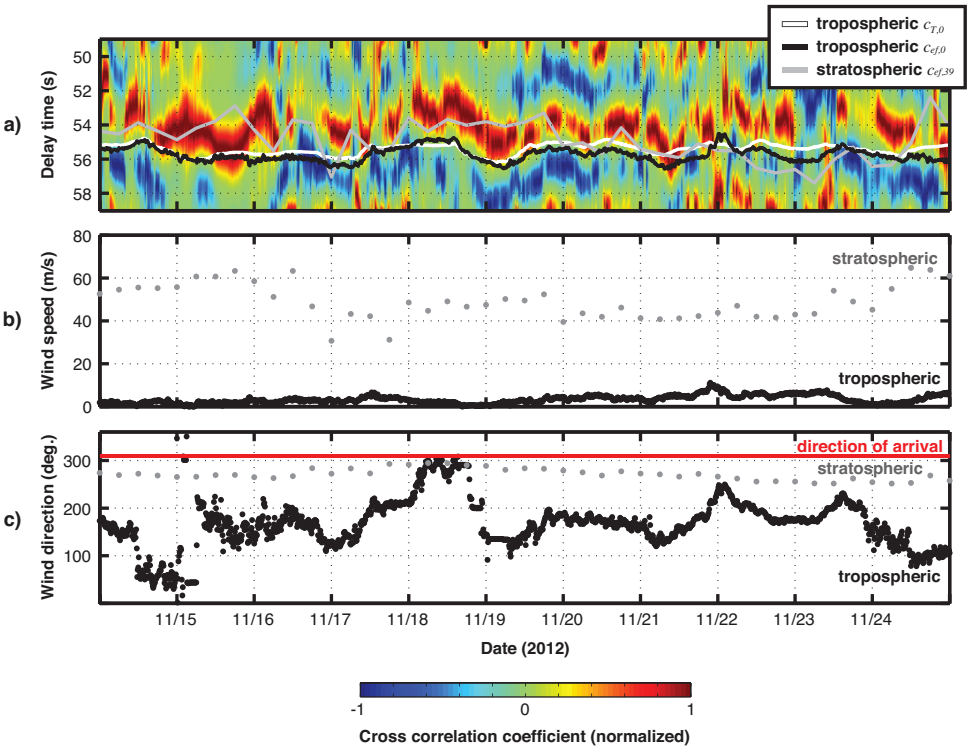


Figure 4.10: ***a)*** *Crosscorrelation of the station combination RS206 and RS412. The color indicates the normalized strength of the crosscorrelation. The white curve shows the arrival time of microbarom signals derived from adiabatic tropospheric sound speed $c_{T,0}$ at the two stations. The black curve indicates the arrival time derived from the effective tropospheric sound speed $c_{ef,0}$, and the gray curve the arrival time derived from the effective stratospheric sound speed $c_{ef,39}$. The tropospheric conditions were measured by the KNMI, and the stratospheric conditions were provided by ECMWF.* ***b)*** *Wind speed in the troposphere (black dots) and in the stratosphere (gray dots).* ***c)*** *Wind direction in the troposphere (black dots) and in the stratosphere (gray dots). The red line indicates the direction of arrival DOA.*

We calculated the correlation coefficient between the result of the crosscorrelation and the different sound speeds (adiabatic surface sound speed $c_{T,0}$, effective surface sound speed $c_{ef,0}$, and effective stratospheric sound speed $c_{ef,39}$), in order to quantify their relation (cf. Table 4.1). We found a higher correlation between tropospheric sound speeds ($c_{T,0}$, $c_{ef,0}$) and infrasonic delay time than between stratospheric sound speed ($c_{ef,39}$) and infrasonic delay time. This indicates that tropospheric wind and temperature have a stronger influence on the microbarom propagation over the array than stratospheric conditions; i.e., we observed tropospheric propagation near the stations. These results are corroborated by the ray tracing simulation (cf. Section 4.5.1).

	$c_{T,0}$	$c_{ef,0}$	$c_{ef,39}$
Crosscorrelation	0.3	0.5	0.01

Table 4.1: *Correlation coefficients between the result of the crosscorrelation and the different sound speeds (adiabatic surface sound speed $c_{T,0}$, effective surface sound speed $c_{ef,0}$, and effective stratospheric sound speed $c_{ef,39}$).*

In the following section the influence of the tropospheric conditions on the delay time is studied further. For this purpose, we selected the crosscorrelations between the stations RS206, RS307, and RS412. Using these values and the least squares estimation introduced in Section 4.5.1, we estimated the effective surface sound speed $c_{est,0}$ over the three stations and the DOA for the whole period of ten days. Figure 4.11a shows $c_{est,0}$ as red dots and $c_{ef,0}$ as a black line. We can see that the difference between $c_{ef,0}$ and $c_{est,0}$ was larger (10 m/s) in the first two days and became smaller (5 m/s) after 16 November. After 19 November the $c_{est,0}$ comes even closer to $c_{ef,0}$ (2 m/s).

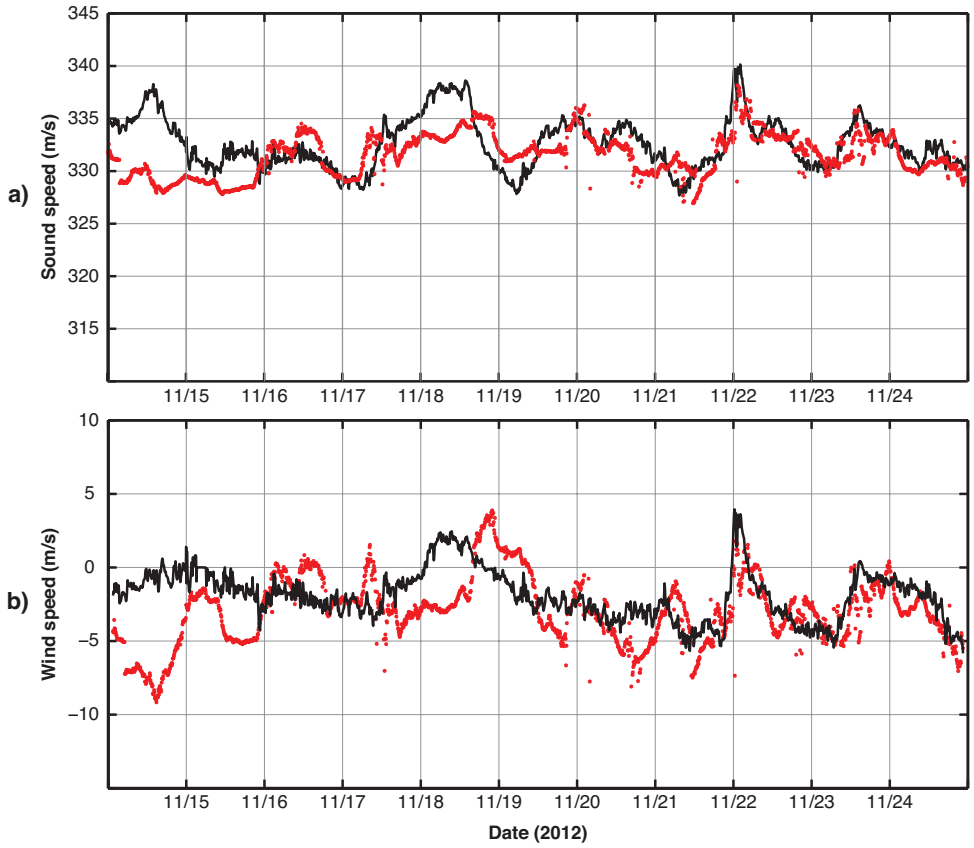


Figure 4.11: ***a)*** *Effective sound speed $c_{ef,0}$ (black line) provided by the ECMWF model in comparison with estimated effective sound speed $c_{est,0}$ (red dots). $c_{est,0}$ is found in a least squares estimation using the crosscorrelations of the stations RS206, RS307, and RS412.* ***b)*** *Wind speed provided by ECMWF (black line) and estimated wind speed (red dots). The wind speed was determined by subtracting the adiabatic sound speed $c_{T,0}$ from the estimated effective sound speed $c_{est,0}$.*

Since $c_{est,0}$ consists of $c_{T,0}$ and the projected wind $\vec{u}$, we are able to estimate the wind speed between the three stations by subtracting $c_{T,0}$ from $c_{est,0}$. Figure 4.11b shows the estimated wind speed (red dots) and the wind speed (black line) provided by ECMWF. The difference between estimated wind and measured wind shows a similar trend to the sound speed estimation. The largest difference occurs during the first two days (10 m/s) and becomes smaller with around 5 m/s on 18 November till around 2 m/s after 19 November.

The differences between estimations and measurements correspond to the velocity scatter of 5.9 m/s on 15 November found in Section 4.5.1. The increasing

accuracy of the estimations after 18 and 19 November might be explained by the presence of a stronger wind at 500 m height than at the ground (see Figure S1 in the supporting information), which could cause a duct for the microbaroms below 500 m. Such a duct would reinforce a direct wave propagation between the stations. An explanation of the larger differences before the 18 November is that due to possible refractions in the lower atmosphere, instead of direct paths, uncertainties in the derived sound speed and wind arise. Refractions would result in estimations of the speed which are too low, since the delay time between the stations increases. This theory is supported by the ray tracing simulation (cf. Section 4.5.1) in Figure 4.8, where we find refractions in the lower atmosphere near the array at the 15 November.

4.6 Conclusions

We successfully applied infrasonic interferometry to measured microbaroms. The delay time of the microbaroms between two stations is determined through cross correlating the recordings. This calculation for all 55 station pairs of the "Large Aperture Infrasound Array" (LAIA) gives the delay time of microbaroms up to a distance of 40.6 km, i.e., the infrasonic wave of the microbaroms is coherent up to this distance. The derived delay times are used to estimate the direction of arrival (DOA), which corresponds to the known microbarom sources in the north Atlantic Ocean. The strength of the 55 crosscorrelations were used to show that the coherence of the microbaroms along the DOA is higher than the coherence of those orthogonal to it. In a curve fitting of the coherence, we determined the sound speed scatter ($\pm 5.9\,\mathrm{m/s}$) and the scatter of the incident angle ($\pm 1.7°$), which follows *Mack and Flinn* [1971] and extends it to higher frequencies. The scattering of the sound speed lies within what can be assumed to be the range of sound speed variations caused by moderate winds. By comparing the wind speed to the strength of the crosscorrelation as a function of time, we can show that in our data set a strong meridional wind at the ground disturbs the delay time estimation. This can be explained by the higher noise levels due to the meridional wind in this specific case. Furthermore, uncertainties in the derived wind can arise due to possible refractions, instead of direct paths.

In a further comparison of the atmospheric state with a crosscorrelation as a function of time, we show that the infrasound propagation over the array is correlated to tropospheric temperature and wind. We could not find a correlation with the stratospheric conditions. Therefore, we conclude that we successfully applied infrasonic interferometry to microbaroms propagating in the troposphere between the stations.

Based on the crosscorrelations between three closest stations, we are able to estimate the effective sound speed and the wind speed as a function of time. Hence, infrasonic interferometry applied to tropospheric propagating microbaroms is a promising approach for determining the effective sound speed and the wind speed at the ground. To probe the stratosphere with this technique, we need interstation or array distances of about 200 km, which is the average stratospheric shadow zone.

4.7 Acknowledgments

The described methods were applied to data, which can be obtained from the authors on request. We thank Matthew M. Haney for sharing his knowledge about the processing of microbaroms and cross correlations. P.S.M. Smets appreciates the support of the ARISE collaborative project, funded by the European Union (http://arise-project.eu). This research is funded by the Netherlands Organization for Scientific Research (NWO).

4.8 Supplemental material

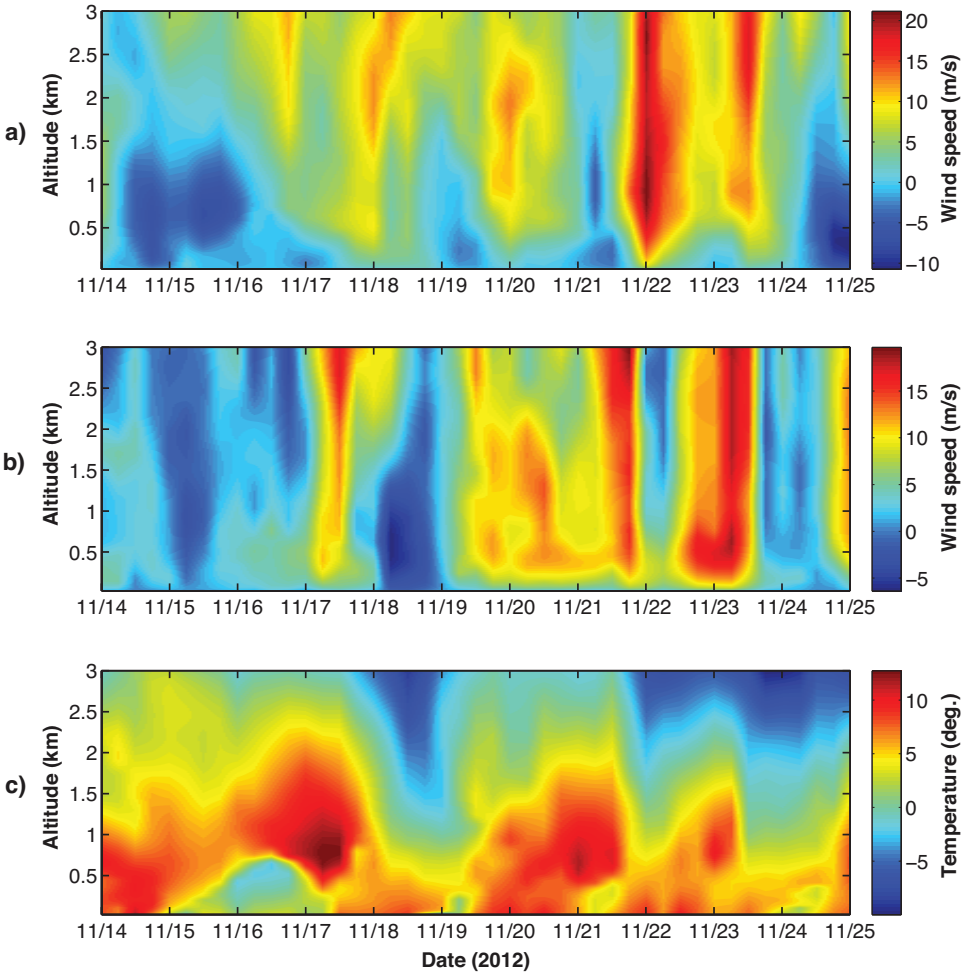


Figure 4.12: *The atmospheric specifications (four times per day) of the European Centre for Medium–Range Weather Forecasts (ECMWF) operational analysis HRES model. This includes* ***a)*** *the zonal wind,* ***b)*** *the meridional wind, and* ***c)*** *the temperature above the array (52.8° N, 6.7° E grid nodes ECMWF).*

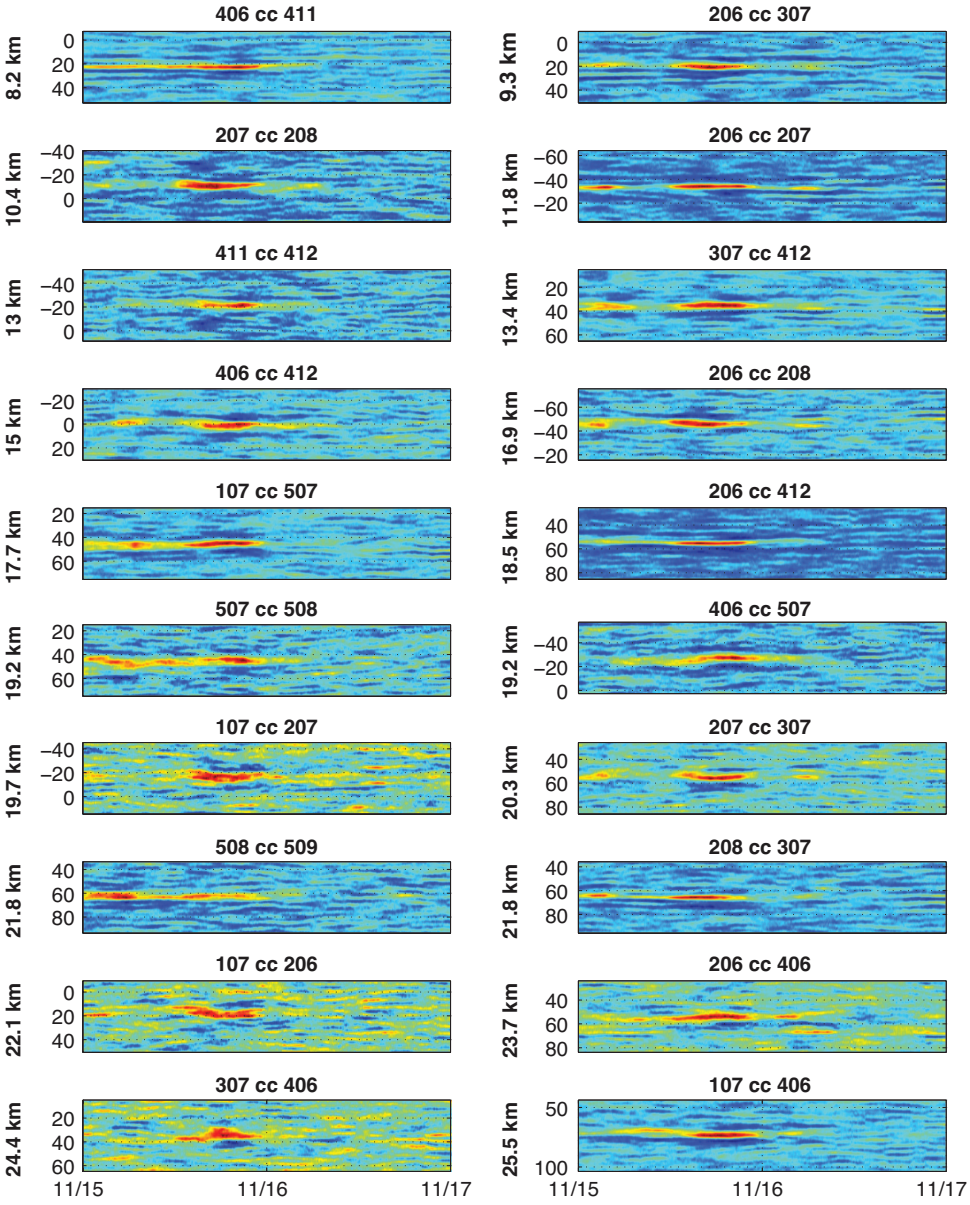


Figure 4.13: *a) The crosscorrelations of the station pairs with inter–station distances between 8.2 km to 25.5 km in order of increasing distance on 15 and 16 November. The color indicates the normalized strength of the crosscorrelation (blue −1, red +1). The delay time is zoomed in on a 50 s time window around the delay time at the maximum of the crosscorrelation.*

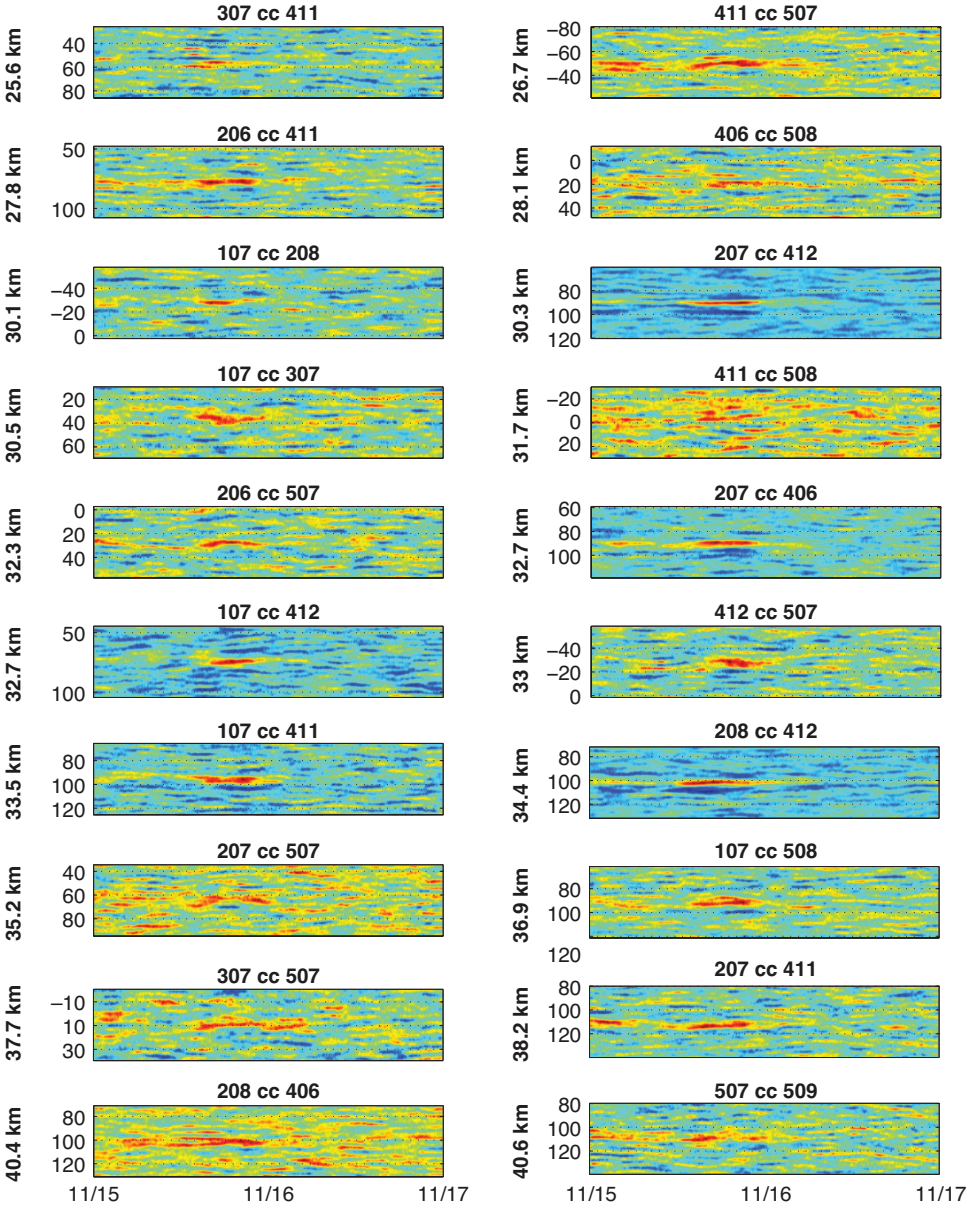


Figure 4.13: ***b)*** *The crosscorrelations of the station pairs with inter–station distances between 25.6 km to 40.6 km in order of increasing distance on 15 and 16 November. The color indicates the normalized strength of the crosscorrelation (blue −1, red +1). The delay time is zoomed in on a 50 s time window around the delay time at the maximum of the crosscorrelation.*

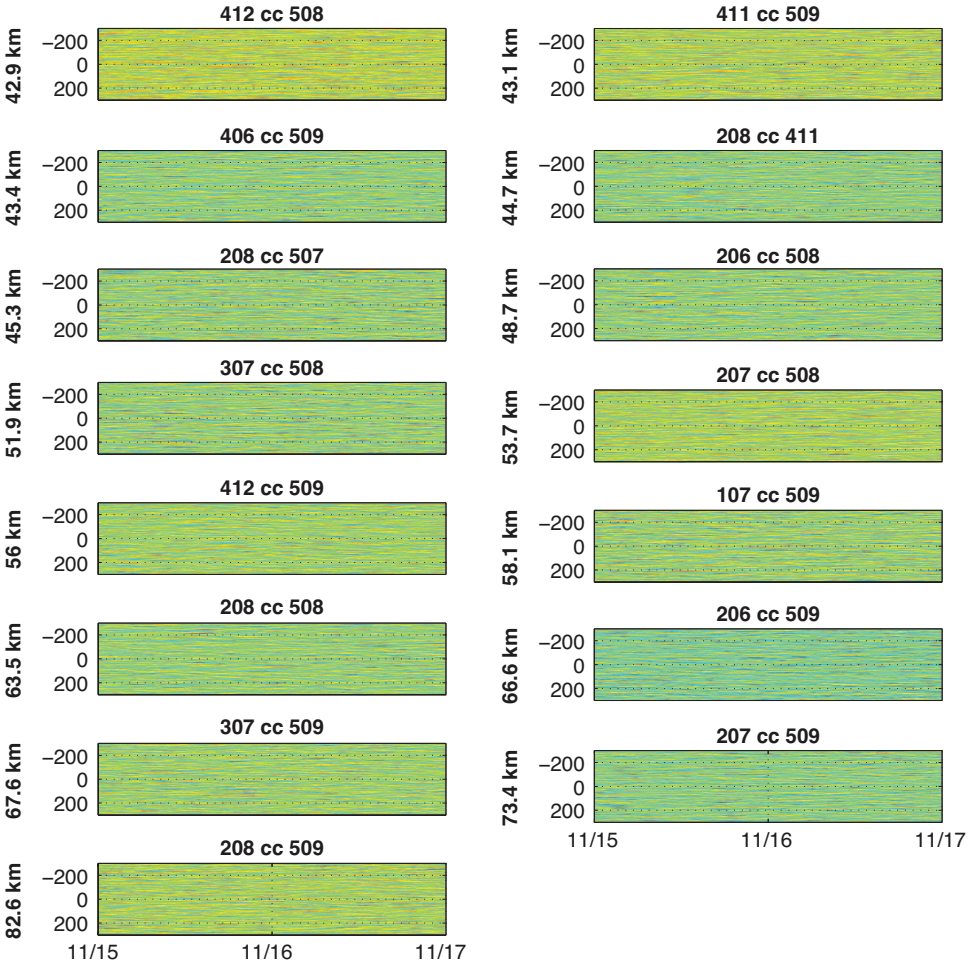


Figure 4.13: ***c)*** *The crosscorrelations of the station pairs with inter–station distances between 42.9 km to 82.6 km in order of increasing distance on 15 and 16 November. The color indicates the normalized strength of the crosscorrelation (blue –1, red +1).*

5

Interferometry applied to stratospherically refracted microbaroms

5.1 Introduction

Up to now, interferometry of infrasound has been shown to be applicable to the troposphere in retrieving the temperature and wind field [*Haney*, 2009; *Johnson et al.*, 2012; *Godin et al.*, 2014; *Fricke et al.*, 2014]. The aim of this study is to explore whether stratospherically refracted energy can be retrieved from crosscorrelating the ambient infrasonic noise field. For this purpose, infrasound recordings from the Alaskan deployment of the infrasonic part of the USArray and of the Alaskan regional array are analyzed.

5.2 Recordings of the Alaskan deployment of the USArray

The USArray deploys, next to a seismic component, infrasound sensors. These sensors are part of the Incorporated Research Institutions for Seismology (IRIS) network. For this study, the location in Alaska was chosen because of the low noise levels due to the thin population and the snow cover over long periods of the year. Under these quiet conditions, it is most likely to measure coherent microbaroms in the ambient noise. The red triangles in Figure 5.1 show the deployed infrasound sensors of the transportable USArray (TA) and the blue triangles show the Alaskan regional array (AK). The center of sensors is located at 147.56 °W and 63.78 °N. The deployed NCPA (National Center for Physical Acoustics) piezo-ceramic infrasound microphone model IFS – 4532 are sensitive in the frequency range of interest, i.e., the microbarom band which peaks around 0.2 Hz [*De Groot-Hedlin and Hedlin*, 2015]. The sensitivity of these microphones is ca. 20 µPa. Since no analog noise reduction

by spatial filters is applied to the sensors, it was decided to select data during wintertime. Diurnal noise levels correlate with the influence of solar radiation. During daytime, noise levels increase as the sun warms the atmosphere which leads to mixing in the boundary layer. At night, the boundary layer stabilizes which reduces the noise levels due to turbulence [*Evers and Haak*, 2005; *Green et al.*, 2012]. In the Alaskan winter, noise levels are expected to be low, since the solar radiation is minimal. Infrasound measurements are digitalized by a Quanterra Q330 AD converter at a sample rate of 40 Hz and available via the BDF data stream of IRIS.

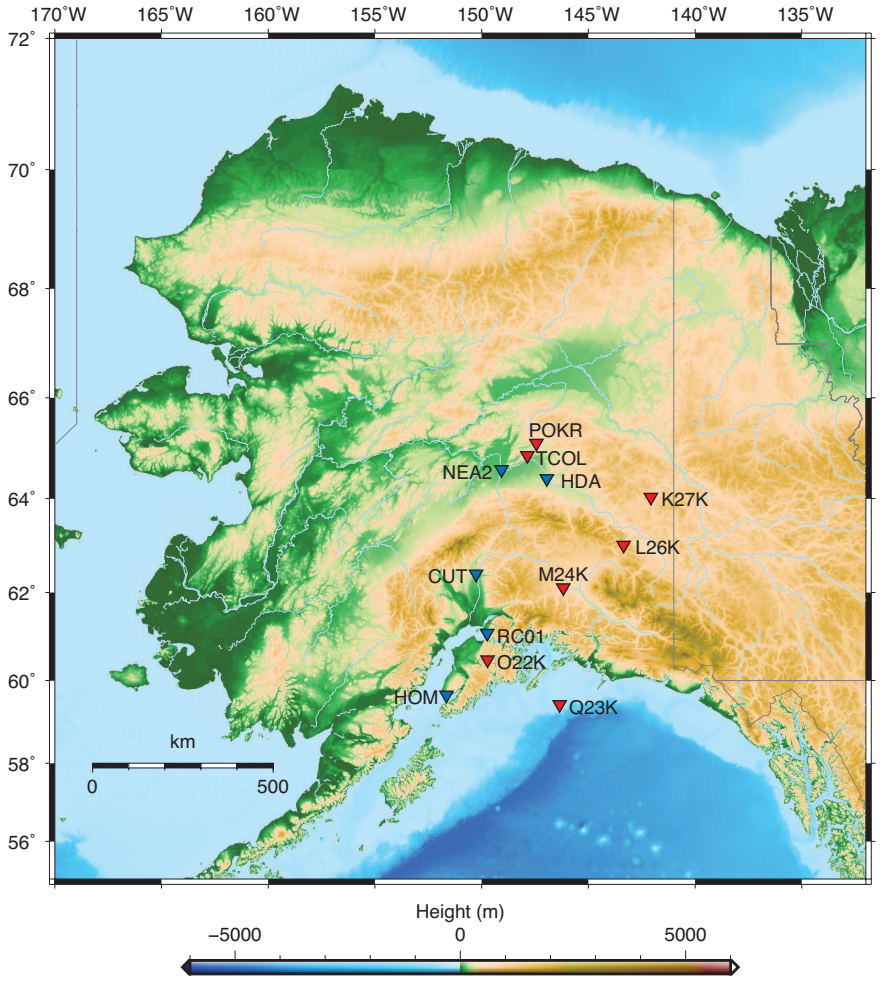


Figure 5.1: *Deployed Alaskan infrasound stations of the transportable USarray (TA) as red triangles and the Alaskan regional array (AK) as blue triangles.*

Figure 5.2 shows spectrograms of the infrasound measurements at the stations shown in Figure 5.1 over a duration of eight months from 1 September 2014 until 30 April 2015. The spectrograms were calculated by using a window length of 100 s and an overlap of 5 s. The name of the station can be found on the left. In the spectrograms, the normalized strengths of the frequencies between 0 Hz and 0.5 Hz are shown. The logarithmic normalized strength is indicated by the color, which can be found in the color bar on the bottom. The black crossed areas indicate the gaps in the measured data. The data in these spectrograms were filtered by a bandpass filter between 0.1 Hz and 0.3 Hz. Figure 5.2 shows that microbaroms can be found as a peak around 0.2 Hz in the winter months.

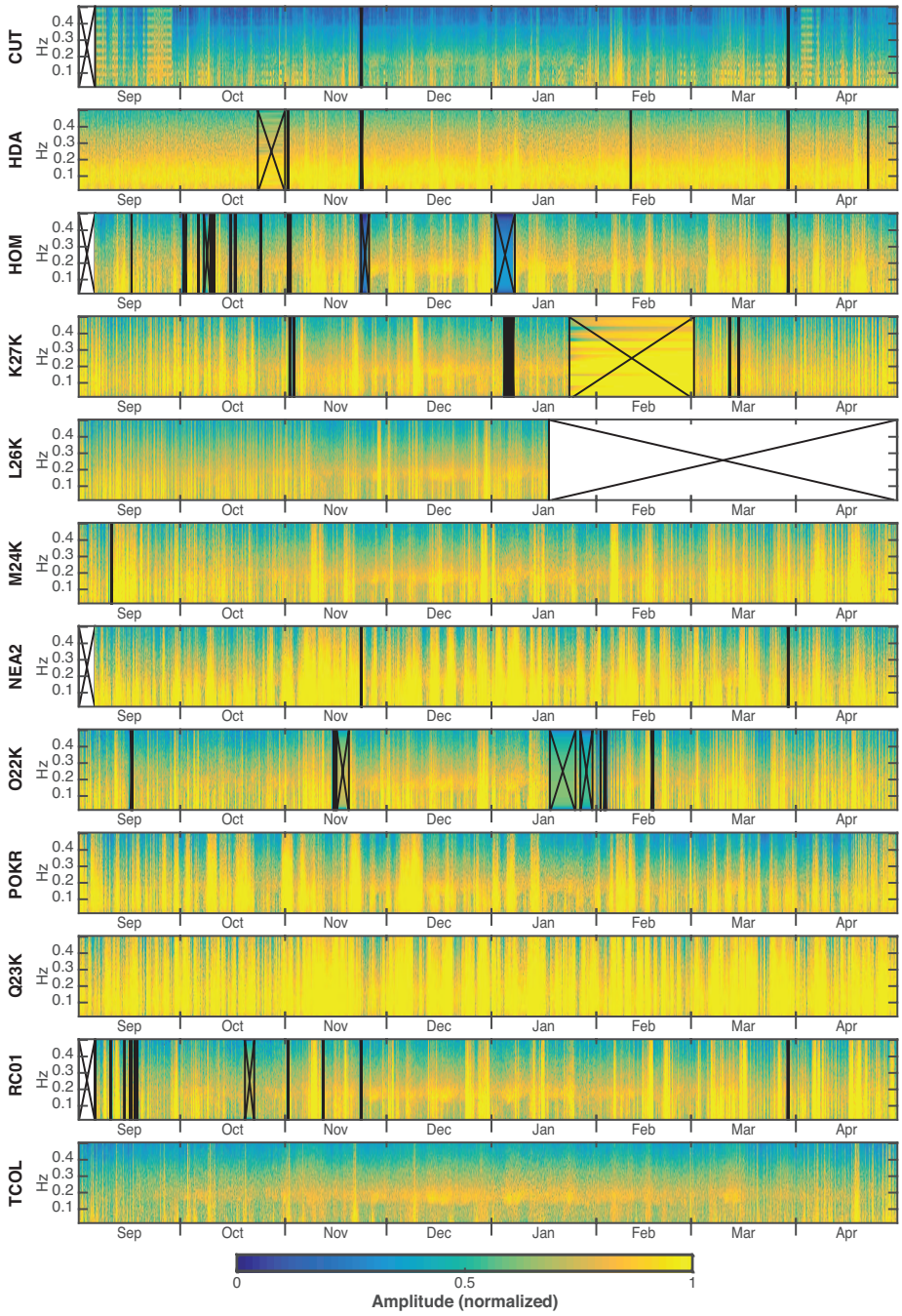


Figure 5.2: *Normalized logarithmic spectrograms of the Alaskan infrasound stations. Microbaroms can be found around* 0.2 Hz *in the winter months. The color shows the logarithm of the amplitude, which is then divided by its maximum.*

5.3 Results of the crosscorrelations

In order to find high values in crosscorrelations, corresponding to stratospherically propagating microbaroms, the optimal preprocessing parameters and the period in which microbaroms occur need to be determined. A first impression of the period in which microbaroms occur is obtained from the spectrograms (see Figure 5.2). In an attempt to further narrow down the period and to find the optimal preprocessing parameter, tropospherically propagating microbaroms are crosscorrelated. By adjusting the preprocessing parameters the tropospheric correlation peaks in the crosscorrelation are amplified. The preprocessing parameters obtained this way and the retrieved period are used in the next section (see Section 5.3.2) to search for correlation peaks in crosscorrelations of stratospherically propagating microbaroms.

5.3.1 Crosscorrelations of tropospherically propagating microbaroms

The station pair POKR – TCOL is 33.85 km apart and a candidate for tropospheric propagation. Figure 5.3a shows the crosscorrelation between measurements of POKR and TCOL in January 2015. The color bar on the right indicates the strength of the crosscorrelation. As mentioned before, it is more likely to measure microbaroms in the winter months. For this reason and according to the analysis of Figure 5.2, the search for peaks in crosscorrelations is initiated by crosscorrelating recordings of January 2015. Prior to crosscorrelation the data are preprocessed following the approach in *Fricke et al.* [2014] (Chapter 4). The below mentioned initial preprocessing parameters can also be found in the left column of Table 5.1. First, the data are filtered by a second order bandpass filter between 0.1 Hz and 0.3 Hz and sampled down from 40 Hz to 10 Hz. In the next processing step the data are temporally normalized by the root–mean–square over a window of 46 s length. In the last step the frequency spectrum of the data is whitened between 0.1 Hz and 0.3 Hz with a 0.12 Hz moving smoothing window. A cosine taper is used to smooth the transition of the spectrum from 0.09 Hz to 0.1 Hz and from 0.3 Hz to 0.34 Hz. The effects of the parameters on the frequency response are shown in Figure 5.4a. The blue curve shows white noise, the red curve shows the pass band and the yellow curve the frequency response to the whitener. The temporal normalization has negligible effects on the frequency response and is not shown in this figure.

The crosscorrelations in Figure 5.3a have correlation peaks at 4/5 January and at 29 January around a delay time of −100 s. For a direct tropospheric path of 33.85 km between the two stations 100 s are a reasonable delay time. The negative delay time indicates that the microbaroms traveled in direction from TCOL to POKR, i.e., that the microbaroms are arriving from south–west, which indicates a source region in the Bering sea. The Bering sea is a well known source region of microbaroms. The crosscorrelations in Figure 5.3a show interference fringe pattern around the peaks. These periodic repeating fringes occur, because the crosscorrelated data only contain a relatively narrow frequency band after bandpass filtering [*Hariharan*, 2012]. In order to avoid the fringes and to obtain only positive correlation values, the envelopes of the crosscorrelations are calculated by applying a Hilbert transformation. The envelopes are shown in Figure 5.3b. In this study the terms crosscorrelation and

envelope of crosscorrelation are used synonymously.

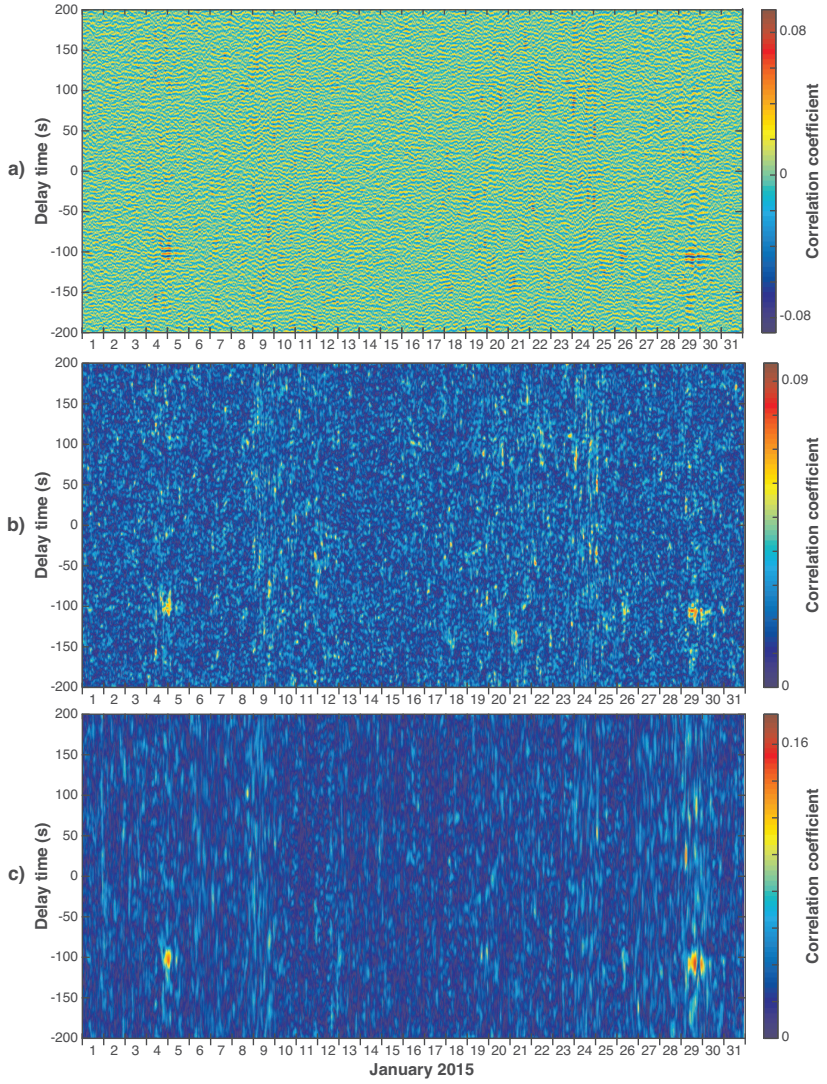


Figure 5.3: ***a)*** *Crosscorrelations between the data of station POKR and TCOL. The data are preprocessed using the initial parameters in Table 5.1. This figure contains peaks around a delay time of −100 s at 4/5 January and at 29 January.* ***b)*** *Envelopes of the crosscorrelations obtained by a Hilbert transformation in order to avoid fringes. In this study the terms crosscorrelations and envelopes of crosscorrelations are used synonymously.* ***c)*** *The envelopes are retrieved by preprocessing the data of POKR and TCOL using the optimized parameters in Table 5.1.*

		Initial parameters	Optimized parameters
Bandpass	f_{low}	0.1 Hz	0.08 Hz
	f_{up}	0.3 Hz	0.11 Hz
Temporal normalization	window length	46 s	58.14 s
Whitener	f_{TL}	0.09 Hz	0.11 Hz
	f_{WL}	0.10 Hz	0.12 Hz
	f_{WU}	0.30 Hz	0.22 Hz
	f_{TU}	0.34 Hz	0.26 Hz
	f_b	0.12 Hz	0.3 Hz
Cross-correlation	window length	3 h	2:59:58.33 h

Table 5.1: *Prior to crosscorrelation the data are preprocessed following the approach described in Fricke et al. [2014] (Chapter 4). The left column lists the initial preprocessing parameters. The parameter set in the right column yields a higher peak in the crosscorrelations at 5 January (see Figure 5.3) and was found by a Nelder–Mead simplex algorithm [Nelder and Mead, 1965; Lagarias et al., 1998].*

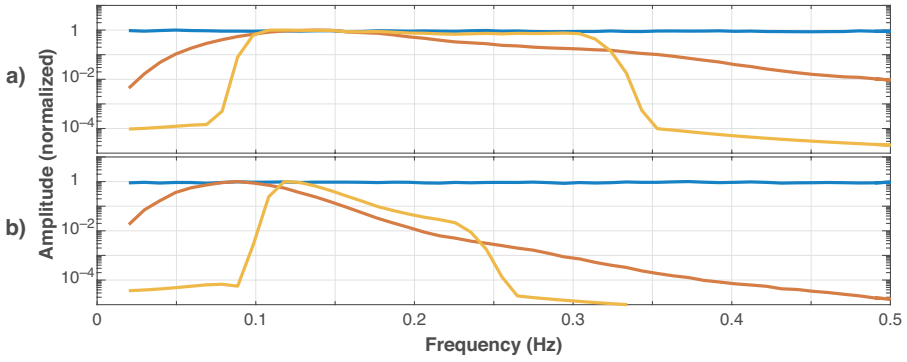


Figure 5.4: *Frequency response of white noise (blue curve) to the band pass filter (red curve) and the whitener (yellow curve).* ***a)*** *Frequency responses to preprocessing by using initial parameters (cf. Table 5.1, left column).* ***b)*** *Frequency responses to preprocessing by using optimized parameters (cf. Table 5.1, right column).*

By adjusting the parameters of the bandpass filter, the automatic gain control, and of the spectral whitener, the height of the correlation peaks at 4/5 January and 29 January is increased. Figure 5.3c shows the result of this parameter adjustment. The data are filtered by a second order bandpass between 0.08 Hz and 0.11 Hz and sampled down from 40 Hz to 10 Hz. In the next preprocessing step the data are temporally normalized by the root–mean–square over a window of 58.14 s length. In the last step the frequency spectrum of the data is whitened between 0.12 Hz and 0.22 Hz with a 0.3 Hz moving smoothing window. This smoothing window is broader than the whitening band and causes a reduction of the higher frequencies (see yellow curve in Figure 5.4). The transitions from 0.11 Hz to 0.12 Hz and from 0.22 Hz to 0.26 Hz were smoothened by a cosine taper. The optimized length of the crosscorrelation window is 2 h, 59 min, and 58.33 s. In Figure 5.4b the frequency response to the band pass is shown by the red curve, and the frequency response to the whitener by the yellow curve.

The influence of the preprocessing parameters on the strength of the correlation peak is nonlinear. Each set of parameters yields a certain strength of the correlation peak and each parameter is a dimension of a multi–dimensional space. By flipping the sign of the crosscorrelation the correlation peak becomes a minimum. In the multi–dimensional space the applied Nelder–Mead simplex algorithm [*Nelder and Mead*, 1965; *Lagarias et al.*, 1998] performs a minimum search. The parameters obtained this way almost doubled the strength of the correlation peak at 5 January (cf. color bars in Figure 5.3).

By crosscorrelating the recordings of the stations POKR and TCOL from September 2014 till April 2015 the crosscorrelations in Figure 5.5 are obtained. The color bar on the bottom shows the strength of the crosscorrelation. Prior to crosscorrelating, the data are preprocessed using the optimized parameters obtained in the previous paragraph (right column Table 5.1). The blue line to the left shows the average overall crosscorrelations of these eight months, the green line is the envelope of the average. Figure 5.5 shows several peaks at +100 s and at −100 s. Also the average on the left shows peaks at ±100 s. The peaks at +100 s occur in November and December 2014 and are higher than the peaks at −100 s in January and February 2015. The crosscorrelations in the winter months show less noise disturbances than the crosscorrelations in September, October, March, and April. The peaks at +100 s indicate that the microbaroms arrive from north–east, which indicates a source region in the North–Atlantic Ocean, and as mentioned before the peaks at −100 s are caused by microbarom sources in the Pacific Ocean.

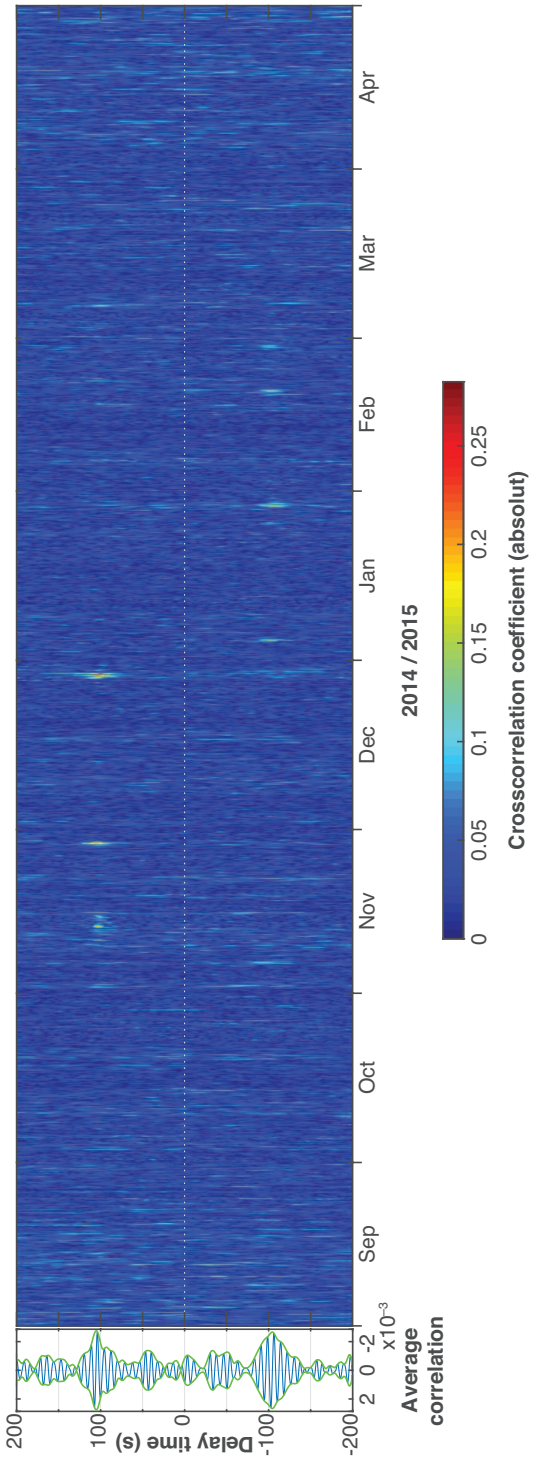


Figure 5.5: *Crosscorrelations of POKR and TCOL recordings from September 2014 till April 2015. The data were processed by applying the optimized parameter set in Table 5.1. These crosscorrelations show correlation peaks around +100 s in November, December, and March and peaks around –100 s in November, January, and February.*

In Figure 5.5 the strongest correlation occurred at 29 December 2014, 19:30h with a correlation coefficient of 0.28. Further analysis of the data showed more periods with high correlation. Figure 5.6 focuses on the periods of the seven strongest correlations, ordered by the strength of the correlation peaks. On the left, the corresponding sound speed profiles, obtained from the European Centre for Medium–Range Weather Forecast (ECMWF), are plotted as a reference. The blue curve is the adiabatic sound speed, the red curve is the effective sound speed, and the vertical yellow line marks the effective sound speed on the ground. Each upper profile shows the effective sound speed from POKR to TCOL and the lower profiles the effective sound speed from TCOL to POKR. The adiabatic sound speed is derived from the temperature above the stations as described in Section 4.4.1. By adding the projected wind to the adiabatic sound speed the effective sound speed from TCOL to POKR is obtained and by subtracting the projected wind from the adiabatic sound speed the effective sound speed from station POKR to TCOL is calculated (cf. equation 4.1). The temperature and wind profiles have a temporal resolution of six hours and 32 levels between 360 m (ground altitude) and three kilometer altitude. The profiles on the left are the particular closest profiles to the time of the correlation peak, for instance in Figure 5.6a the correlation peak occurred at 19:30h and the closest corresponding sound speed profiles on the left are from 18:00h.

For each correlation peak in Figure 5.6 the celerity between POKR and TCOL is determined (see Table 5.2). The celerity c_c is obtained by dividing the distance between POKR and TCOL (33 853.1 m) by the delay time of the particular correlation peak. In Figure 5.6 the celerities are marked by violet circles in the sound speed profiles on the left. According to the trace–velocity matching principle the celerity between two stations is identical to the sound speed at the refraction altitude [*Pierce*, 1989], i.e., the altitude of refraction can be estimated by using the celerity. For this purpose the celerity is compared with the effective sound speed in the profiles and the altitude is determined at which the celerity is equal to the effective sound speed. This altitude is the refraction altitude. In Table 5.2 the refraction altitude is listed in the right column. The trace–velocity matching only applies, if the celerity is equal to the trace velocity. This is the case, if the station pair is oriented parallel to the direction of arrival (DOA), if a stratified atmosphere without lateral changes is assumed, and if the wave propagates through the troposphere, i.e., the trace–velocity matching method only works for direct waves not for refracted waves.

	Delay time (s)	**Celerity c_c(m/s)**	**Refraction altitude (m)**
29 Dec, 19:30h	+99.0	342	770
28 Nov, 19:20h	+102.2	331	750
13 Nov, 13:50h	+102.0	332	390
29 Jan, 15:20h	–108.8	311	370
5 Jan, 0:00h	–104.0	326	1650
19 Feb, 18:30h	–103.6	327	710
27 Feb, 22:40h	–101.5	334	1640

Table 5.2: *Left: delay time of each correlation peak in Figure 5.6. Middle: the celerity is obtained by dividing the distance of 33 853 m by the delay time of the particular correlation peak. Right: the refraction altitude is the altitude at which the sound speed profile (red curves in Figure 5.6) has the same value as the celerity.*

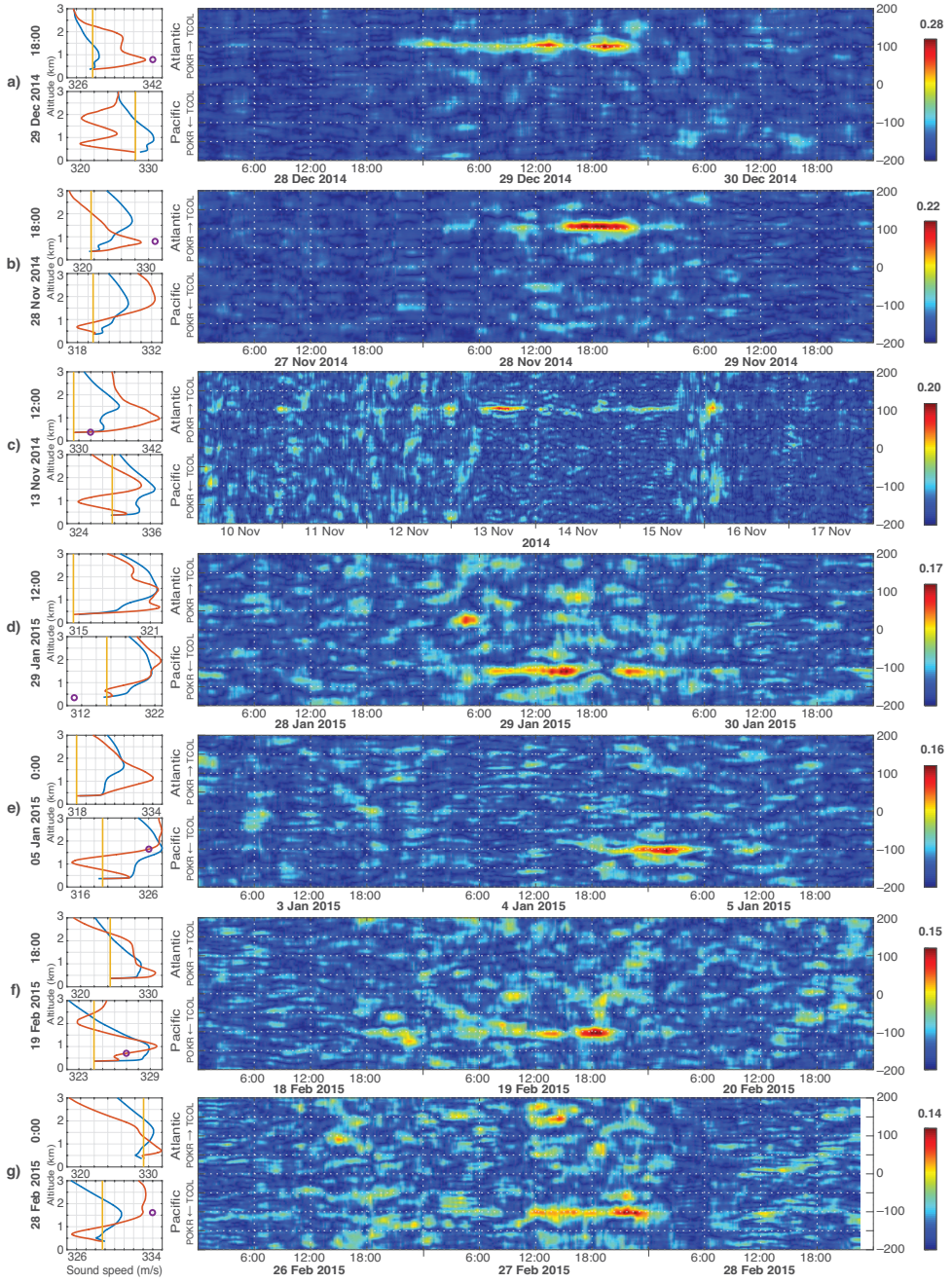


Figure 5.6: *The seven strongest correlation peaks of the crosscorrelation between POKR and TCOL in Figure 5.5. The periods are ordered by the strength of the correlation peaks. On the left the corresponding sound speed profiles are plotted (blue curve: adiabatic sound speed c_T, red curve: effective sound speed c_{ef}, yellow line: sound speed on the ground, violet circles: celerities at the refraction altitude).*

5.3.2 Crosscorrelations of stratospherically propagating microbaroms

In order to find microbaroms that propagated through the stratosphere between two stations the inter–station distance needs to be larger than 150 km to bridge the shadow zone and to allow stratospheric refractions.

In the next sections two possible scenarios are assumed. In the first scenario, it is assumed that the microbarom sources are surrounding the stations. The theory of this scenario is described in Section 2.2. Figure 2.11 illustrates this source distribution. According to the theory the sources within the Fresnel zone interfere constructively (stationary phase) and yield the delay time between the stations as a peak in the average of the crosscorrelations. The sources outside of the Fresnel zone do not contribute to the average. The crosscorrelations of the station pairs with an inter–station distance between 149.3 km and 250.9 km are searched for high correlations. The period which is analyzed runs from September 2014 until April 2015 (Figure 5.7). Then in Figure 5.8 the search is narrowed down to one month (December 2014) in which the tropospheric crosscorrelations showed the strongest correlation peak. In the next part, the search is zoomed in on the delay time of the stationary phase (Figure 5.9), i.e., the delay time, which stratospherically propagating infrasound needs to travel between the particular station pair.

The second scenario takes the varying source locations and varying atmospheric conditions into account. This scenario assumes that the source locations and the atmospheric wind and temperature are varying too fast to obtain a clear peak at the stationary phase in the average. Therefore, the microbarom source activities in the North Atlantic and North Pacific are modeled (see Section 4.4.2) and the propagation path from the sources to the stations are simulated by a raytracer (see Section 3.3). All these simulations take atmospheric wind and temperature into account. This way the delay time between each station pair is estimated dependent on the source location.

First scenario: Surrounding sources

Figure 5.7 shows the crosscorrelations of ten station pairs, with an inter–station distance between 149.3 km and 250.9 km, ordered by distance. The distance can be found on the left side. Prior to crosscorrelation the data were preprocessed using the previously optimized parameters. The color bar on the bottom shows the strength of the crosscorrelations. The gaps in the data are marked by white crosses. On the left the average of the crosscorrelations is shown. The delay time and the corresponding direction of the sound propagation can be found on the vertical axis. The crosscorrelations in the winter months show less noise disturbances than the crosscorrelations in September, October, March, and April. The crosscorrelations in Figure 5.7 show periods with higher correlation coefficients in the end of December. These are the same periods in which the correlation peaks in the tropospheric crosscorrelations occurred. These high correlation periods occurred in all ten station combinations.

In Figure 5.8, the same crosscorrelations as in Figure 5.7 are shown, but focused on December 2014. The strength of each crosscorrelation is indicated by the colorbar on the right. The zoom in on December shows that the periods with higher correlations occurred from 28 to 31 December, but also in the beginning between 7 and 8 December most crosscorrelations show higher coefficients.

Figure 5.9 also shows the crosscorrelations of December 2014, but zoomed in on the estimated delay time, which the sound needs to propagate on a stratospheric path between the stations (stationary phase). The range of delay times was estimated by applying a raytracer (see Section 3.3). In order to simulate the propagation, the raytracer uses the ECMWF profiles of wind and temperature between the particular station pair in December 2014. If there are dominant correlation peaks in the crosscorrelations around the assumed delay time, these peaks will show up in Figure 5.9. Figure 5.8 and Figure 5.9 show that the correlation peaks are distributed rather random over all delay times in the period from 28 to 31 December as well as from 7 to 8 December. The maxima of the averages in Figure 5.9 and the resultant celerities are listed in Table 5.3. The maxima of the station pairs RC01 – HOM, O22K – CUT, and NEA2 – CUT are relatively clear peaks in the average. All average maxima are scattered rather randomly over the limited delay times in Figure 5.9. Also the delay times and the resultant celerities are scattered rather random and do not yield a consistent direction of arrival (DOA).

Station pair			**Delay time (s) (Max. average)**	**Celerity c_c (m/s)**
RC01	—	**CUT**	+525.6	284
M24K	—	**L26K**	+679.9	262
RC01	—	**HOM**	–623.7	307
M24K	—	**CUT**	+763.2	282
O22K	—	**CUT**	–621.0	348
RC01	—	**M24K**	+742.8	297
Q23K	—	**O22K**	+653.2	340
L26K	—	**HDA**	–698.2	337
K27K	—	**HDA**	+873.7	275
NEA2	—	**CUT**	+838.2	299

Table 5.3: *Maxima of the averages in Figure 5.9 and the resultant celerities.*

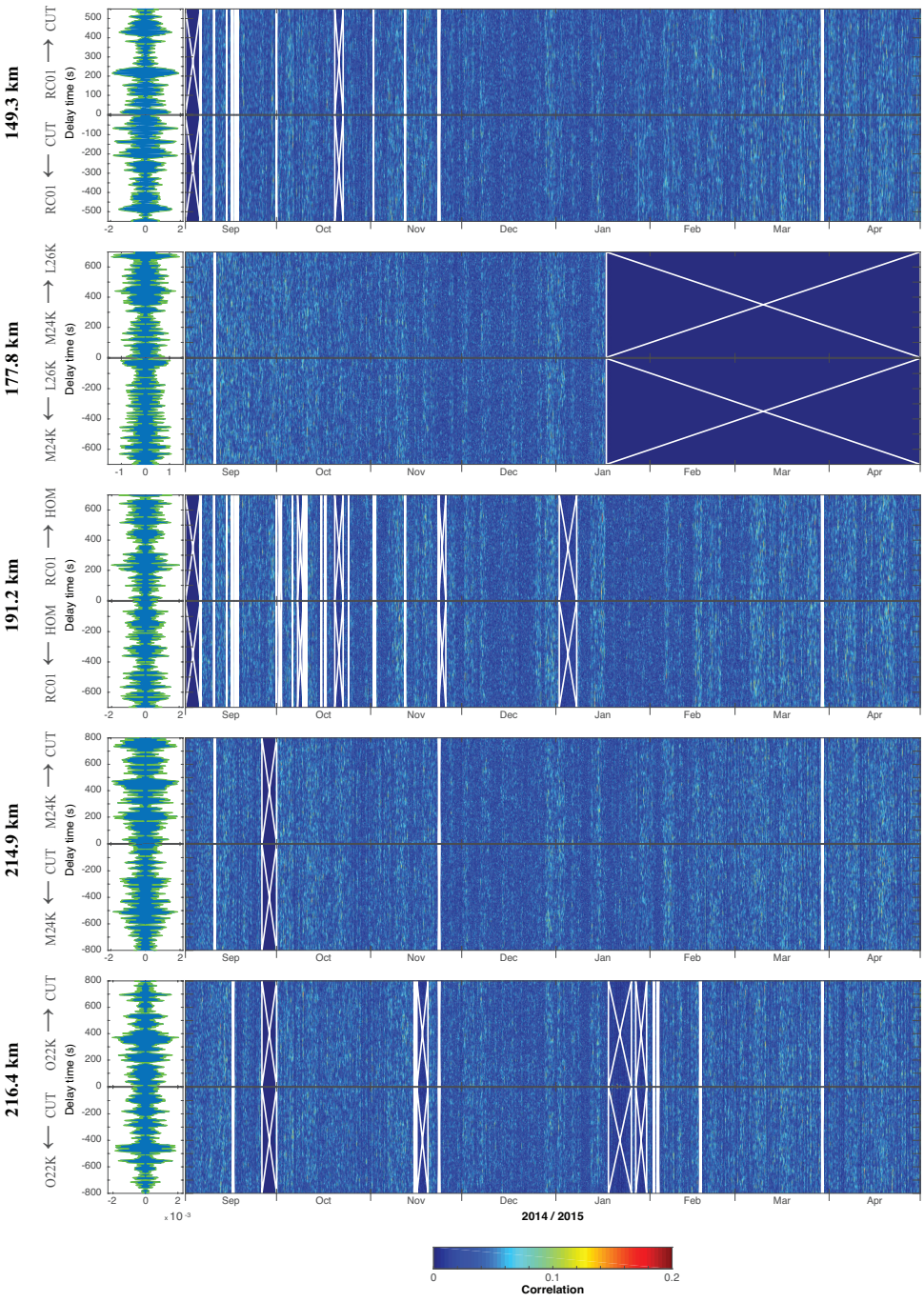


Figure 5.7: *a) Crosscorrelations with inter–station distances between 149.3 km and 216.4 km from September 2014 until April 2015. The associated direction of arrival is indicated by the arrow on the left.*

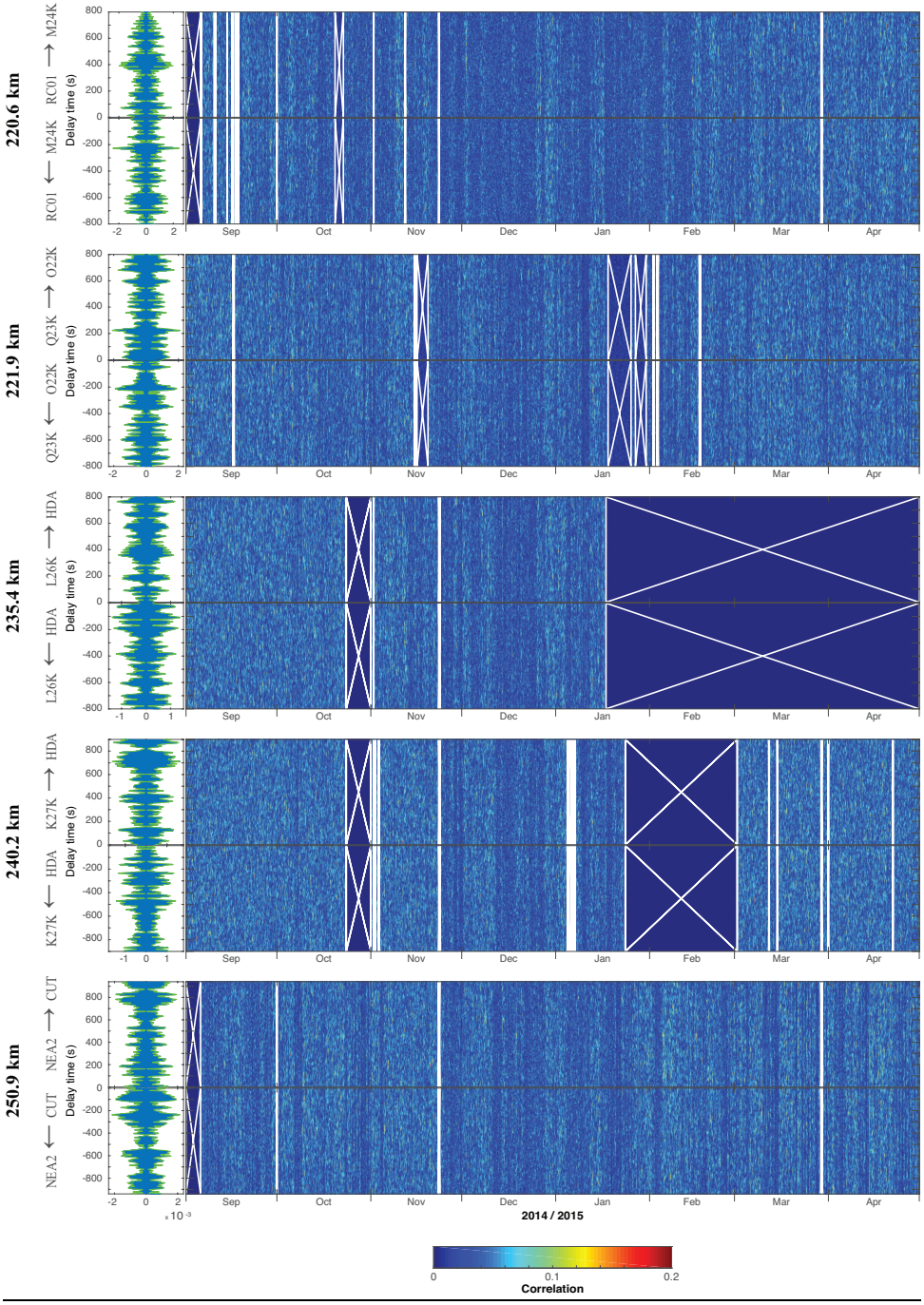


Figure 5.7: ***b)*** *Crosscorrelations with inter–station distances between 220.6 km and 250.9 km from September 2014 until April 2015. The associated direction of arrival is indicated by the arrow on the left.*

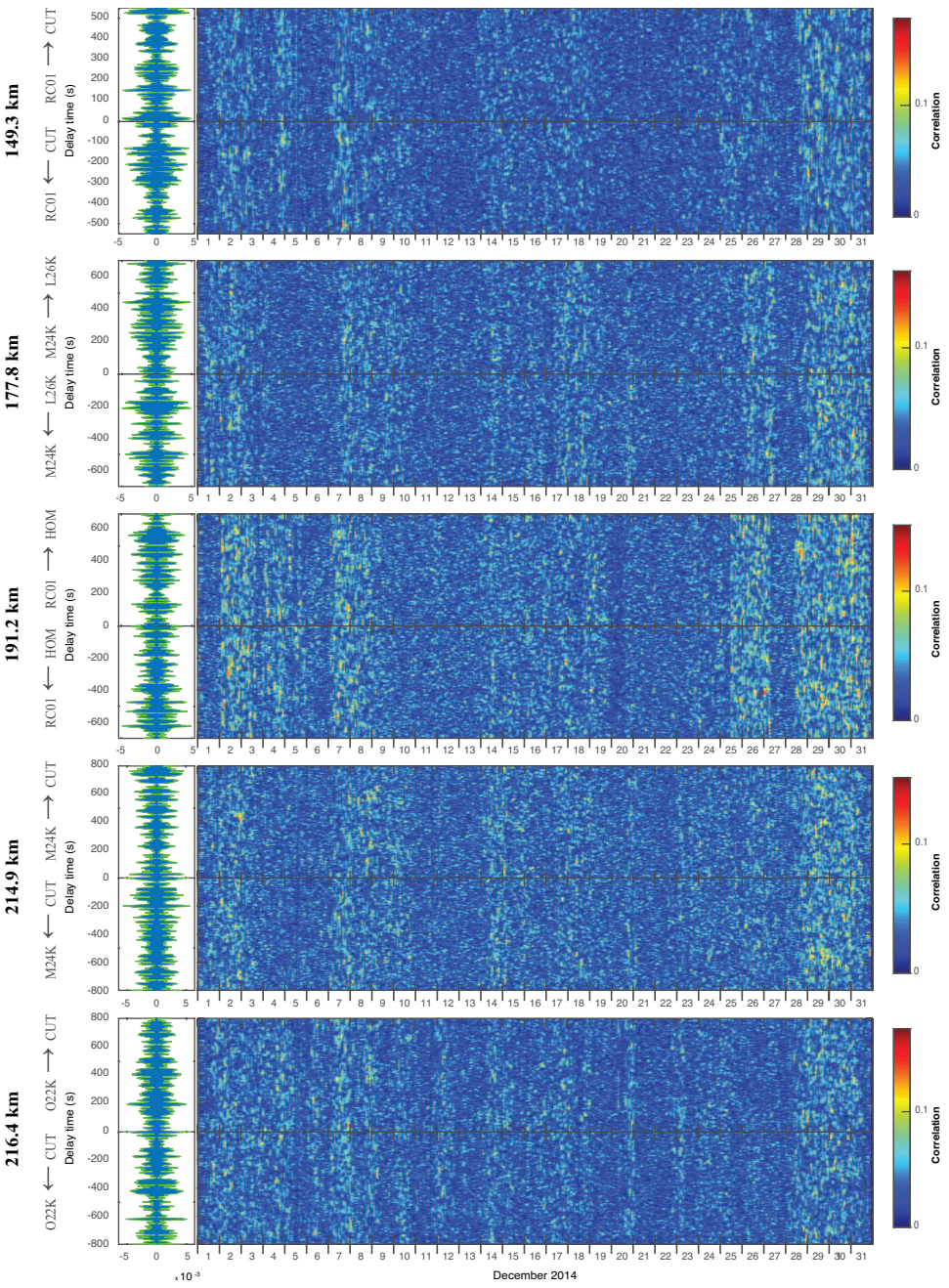


Figure 5.8: *a) Crosscorrelations with inter–station distances between 149.3 km and 216.4 km in December 2014. The associated direction of arrival is indicated by the arrow on the left.*

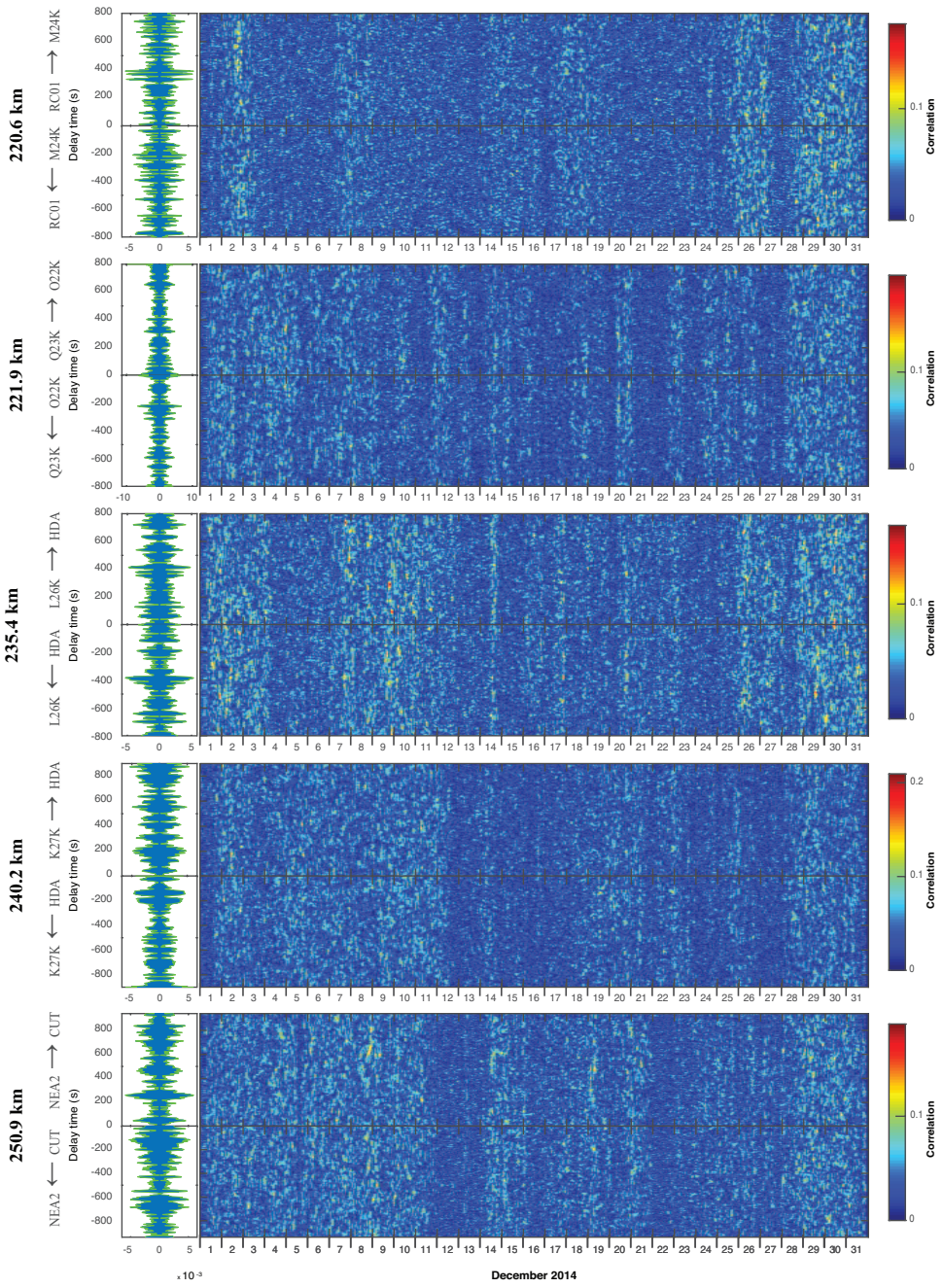


Figure 5.8: *b) Crosscorrelations with inter–station distances between 220.6 km and 250.9 km in December 2014. The associated direction of arrival is indicated by the arrow on the left.*

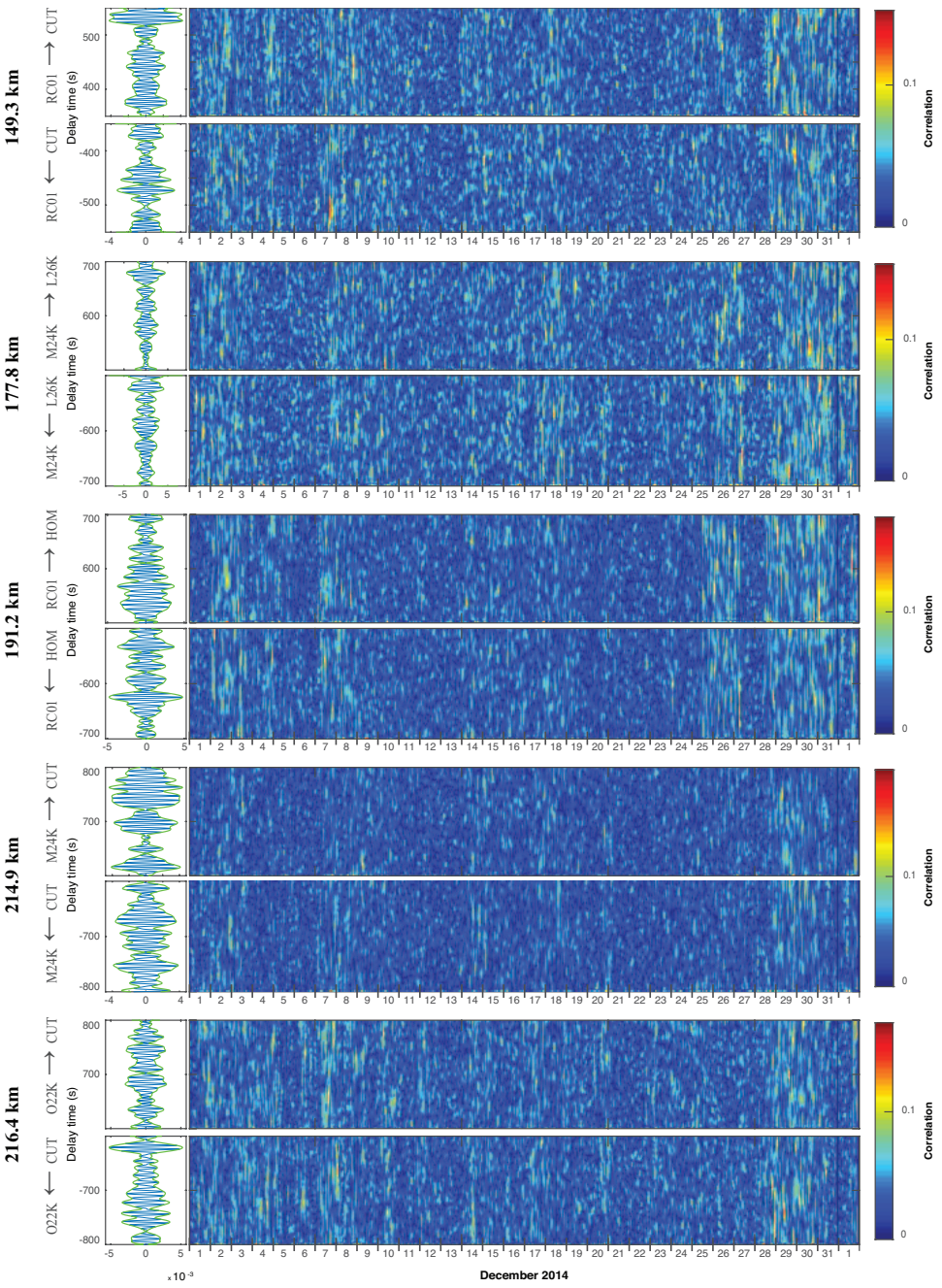


Figure 5.9: *a) Crosscorrelations with inter–station distances between 149.3 km and 216.4 km in December 2014. The delay time is zoomed in around the estimated delay time, which the sound needs to propagate stratospherically between the stations.*

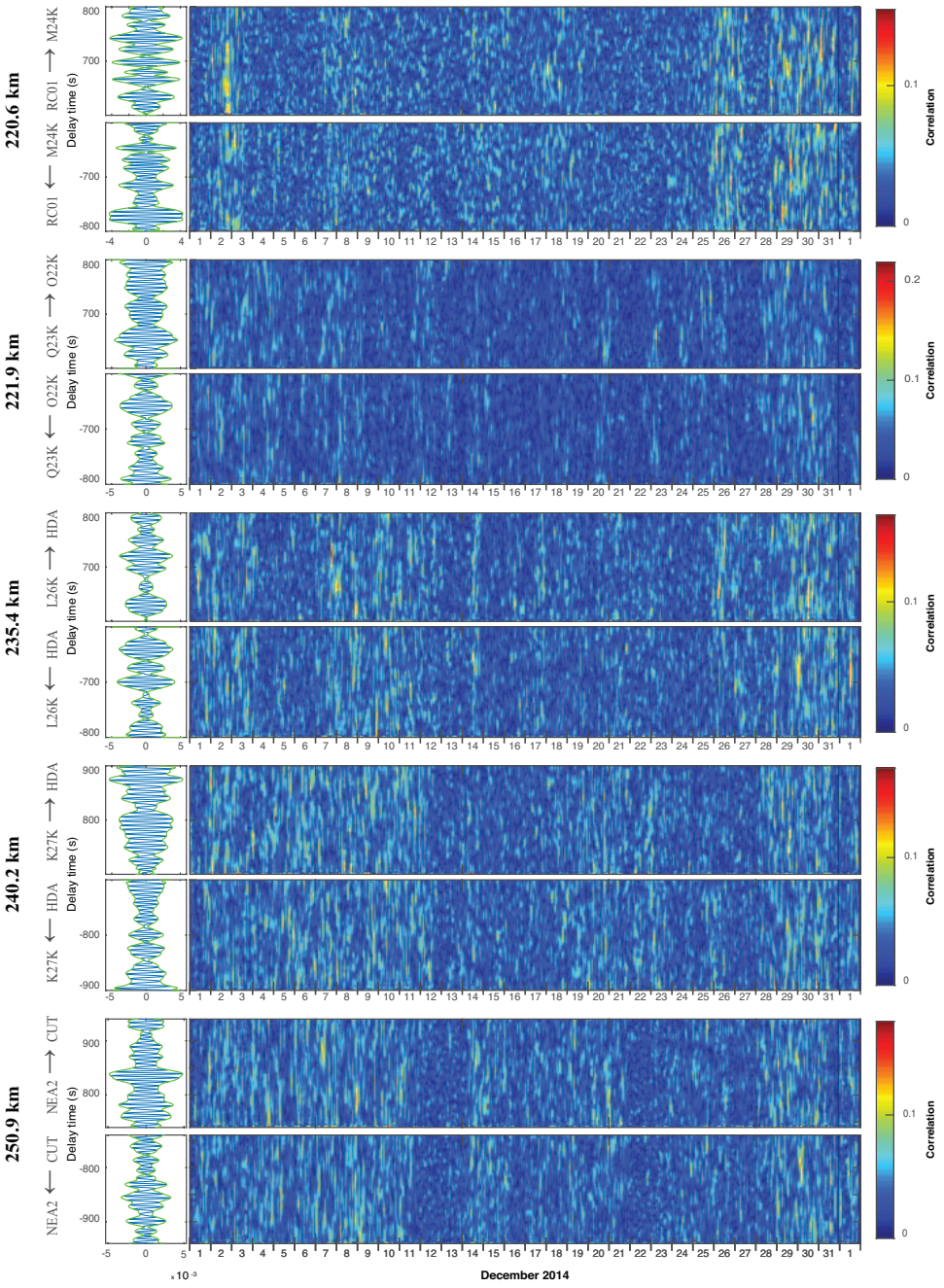


Figure 5.9: ***b)*** *Crosscorrelations with inter–station distances between 220.6 km and 250.9 km in December 2014. The delay time is zoomed in around the estimated delay time, which the sound needs to propagate stratospherically between the stations.*

Second scenario: Taking the microbarom source regions into account

Microbaroms are generated by the non–linear interaction of oceanic waves and occur typically at twice the frequency of the waves [*Brekhovskikh et al.*, 1973; *Donn and Naini*, 1973]. As described in Section 4.4.2, a two–fluid source model and a sea–state model has been developed by *Waxler and Gilbert* [2006], and was applied in several studies, see *Stopa et al.* [2012]; *Walker* [2012]; *Assink et al.* [2014]. These models were further developed by *Waxler et al.* [2007] to take the bathymetry into account and were implemented by *Smets and Evers* [2014]. The microbarom sources in the North Pacific and North Atlantic are modeled for each day in December 2014 by using ECMWF models, i.e., 31 maps of source activities are simulated. Figure 5.10 shows the modeled microbarom source activities at six selected days. The color indicates the strength of the source regions in decibel. The upper row (Figure 5.10a–c) shows microbarom sources in the Pacific Ocean and the lower row (Figure 5.10d–f) microbarom sources active in the Atlantic Ocean. The black lines trace the directions of arrival (DOA) at the Alaskan stations (red triangle).

In order to estimate the delay time between each station pair for each day of December, the most dominant source in the Pacific Ocean and the Atlantic Ocean is selected. For this purpose the source strength is divided by the distance between source and station. The maximum of the obtained ratio is the dominant source. Figure 5.11 shows the source locations of these dominant sources. From the 62 source locations the travel time to each station is simulated by a raytracer (see Section 2.1.1). The raytracer uses the ECMWF wind and temperature profile of the location at the particular day. By subtracting the particular travel times from each other, the delay times between the station pairs are estimated.

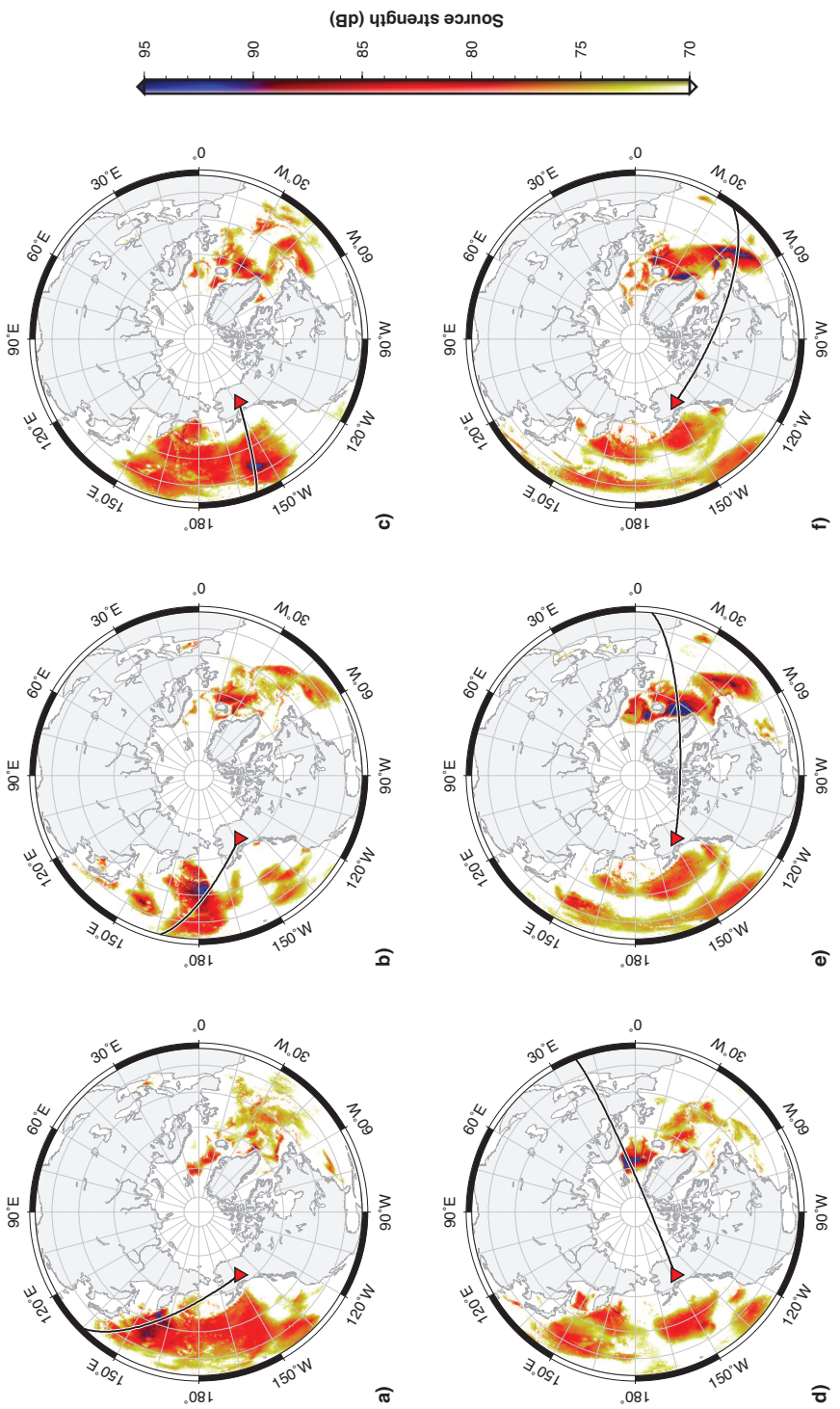


Figure 5.10: *Six selected maps of modeled microbaroms sources at completely different locations in December 2014. The black line shows the corresponding direction of arrival (DOA) at the Alaskan stations (red triangle).* ***a–c)*** *Various source locations in the Pacific Ocean.* ***d–f)*** *Various source locations in the Atlantic Ocean. Maps of microbarom activities are modeled for each day in December 2014.*

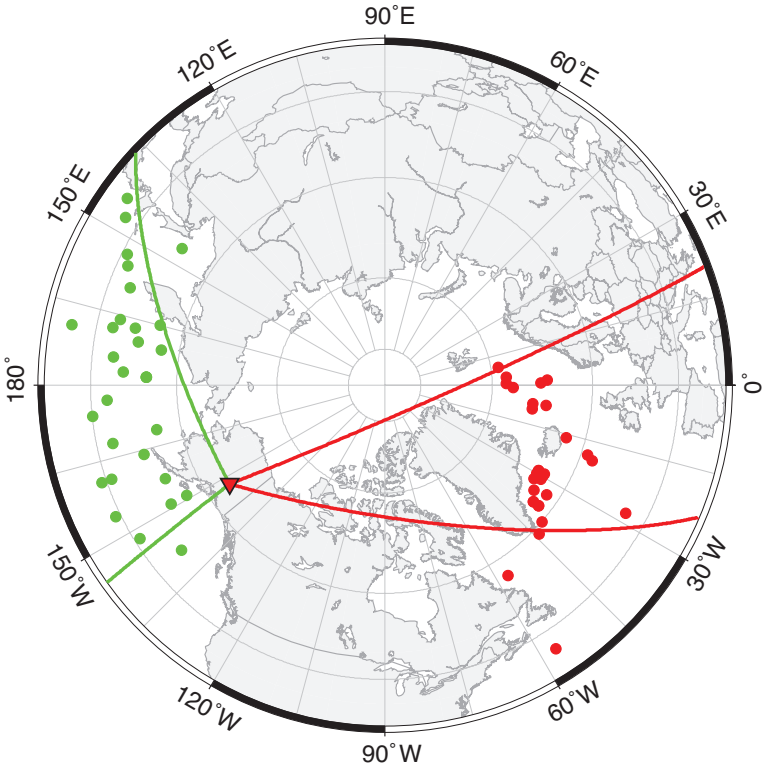


Figure 5.11: *The 62 dominant microbaroms sources in December 2014, selected dependent on strength and distance to the stations (triangle).*

Figure 5.12 shows the same crosscorrelations as in Figure 5.8, but now the estimated delay times are added superimposed accordingly to the simulated source location. The white circles mark the delay times of Pacific sources and the white rhombi mark the delay time of the Atlantic sources. The colorbar on the right indicates the strength of the correlations and the delay time is written on the vertical axis. The orientation of the station pair is shown on the left by the blue line in the polar plot. Note the pole of these orientation plots is not the north pole as in Figure 5.10, but marks the center of the particular station pair. In order to determine how fast the simulated delay times vary the standard deviation (STD) of the delay times is calculated. The average and the STD of the simulated delay times are listed in Table 5.4. In general these STD's are relatively large, because of the high variability of the source locations, which cause a high variability of the DOA (cf. Figure 5.11). According to the STD the simulated delay times of the Pacific sources are varying more than the simulated delay times of the Atlantic sources with three exceptions. The delay times of the Atlantic sources between RC01 – HOM, RC01 – M24K, and K27K – HDA has a bigger STD than the delay times of the Pacific sources. The station orientation has influence on the STD. Due to the simulated source locations the general range of DOA is known. The delay times of the station pairs oriented orthogonal to the DOA show bigger STD than the station pairs parallel to the DOA.

Station pair	Pacific sources average simulations ± standard deviation (s)	Atlantic sources average simulations ± standard deviation (s)
RC01 — CUT	+88.1 s ± 249.7 s	–360.8 s ± 219.9 s
M24K — L26K	+551.9 s ± 207.6 s	–582.7 s ± 151.8 s
RC01 — HOM	–445.1 s ± 266.0 s	+784.4 s ± 271.4 s
M24K — CUT	–606.2 s ± 312.2 s	+185.1 s ± 309.1 s
O22K — CUT	+127.7 s ± 378.0 s	–543.9 s ± 306.0 s
RC01 — M24K	+694.3 s ± 181.9 s	–560.1 s ± 268.9 s
Q23K — O22K	–448.0 s ± 342.7 s	–146.8 s ± 228.8 s
L26K — HDA	–365.9 s ± 336.8 s	–147.3 s ± 252.9 s
K27K — HDA	–660.3 s ± 278.1 s	287.4 s ± 342.2 s
NEA2 — CUT	–508.1 s ± 256.7 s	799.9 s ± 176.6 s

Table 5.4: *Average and standard deviation of the simulated delay times. The left column lists the delay times of Pacific sources and the right column the delay times of Atlantic sources.*

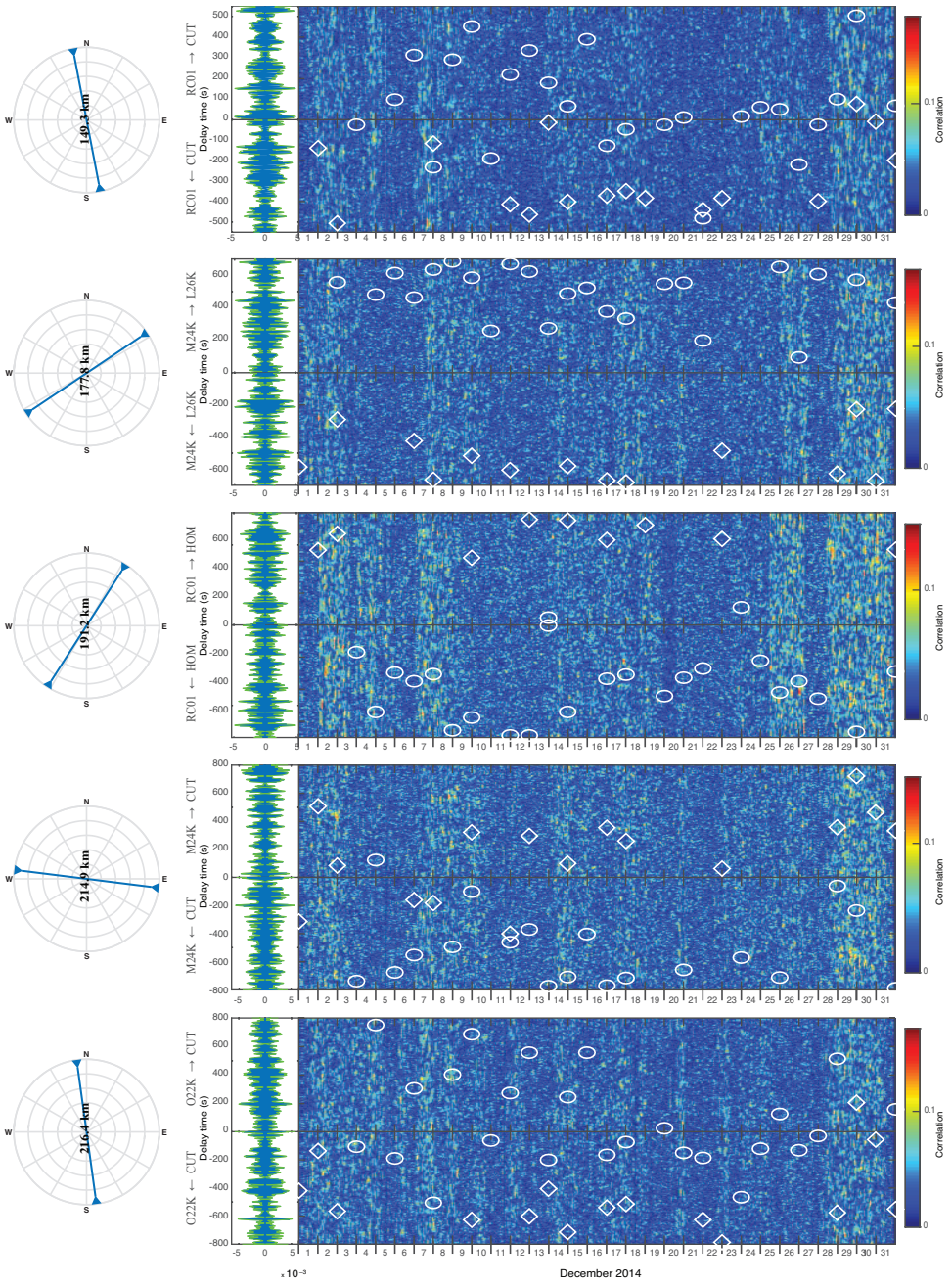


Figure 5.12: ***a)*** *The same crosscorrelations as in Figure 5.8a with estimated delay times. The white circles mark the delay times of Pacific sources and the white rhombi mark the delay time of the Atlantic sources. The orientation is indicated by the blue line on the left. Inter–station distances from 149.3 km to 216.4 km.*

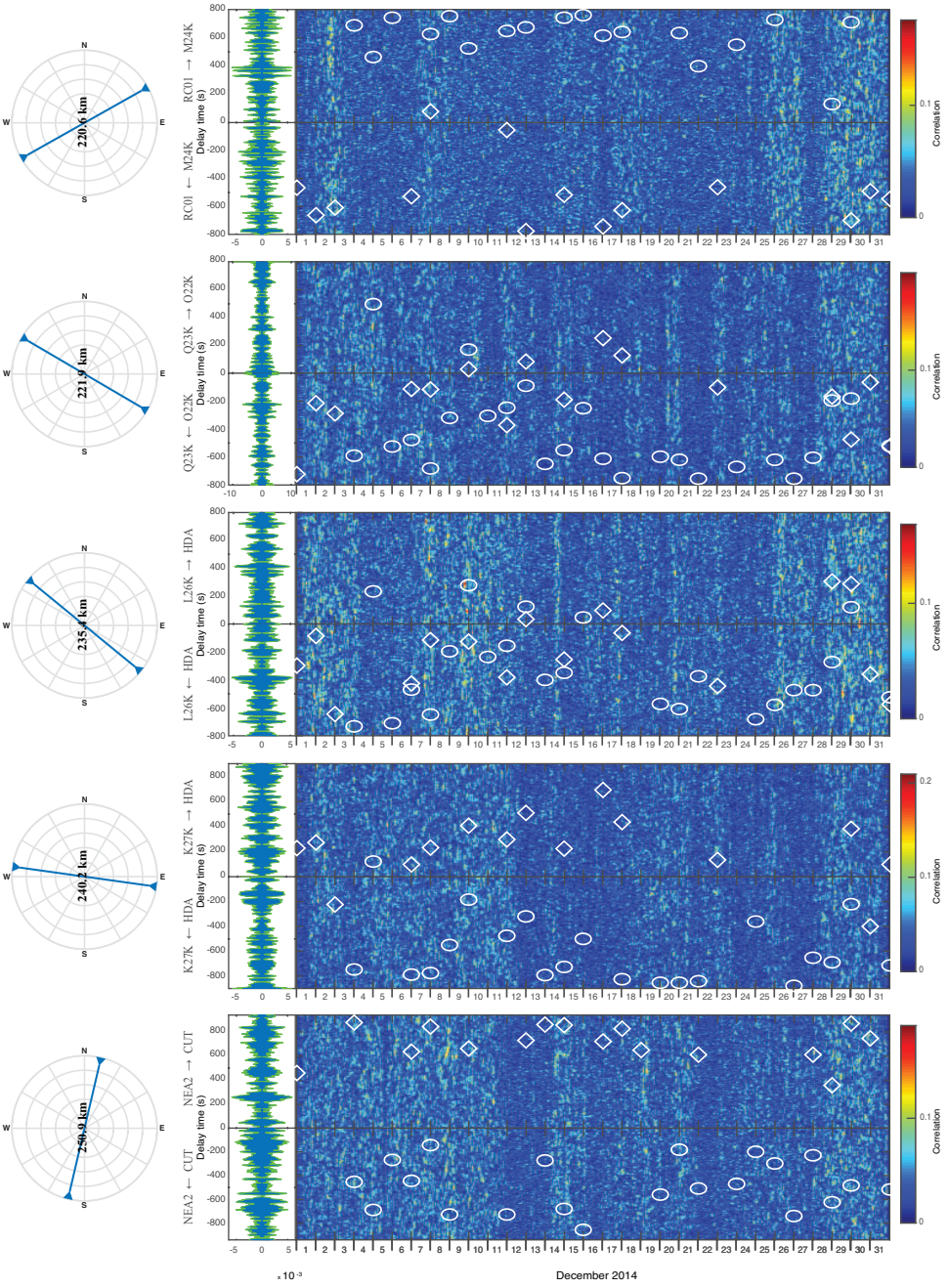


Figure 5.12: ***b)*** *The same crosscorrelations as in Figure 5.8b with estimated delay times. The white circles mark the delay times of Pacific sources and the white rhombi mark the delay time of the Atlantic sources. The orientation is indicated by the blue line on the left. Inter–station distances from 220.6 km to 250.9 km.*

5.4 Discussion

■ 5.4.1 Tropospheric crosscorrelations

Tropospheric microbarom propagation between POKR and TCOL is possible if the atmospheric conditions force the microbaroms to stay in the troposphere, i.e., either the microbaroms propagate parallel to the ground or they are refracted back to the ground within the troposphere. Refraction occurs, if a tropospheric layer has a higher sound speed than the layer on the ground (cf. Section 2.1.1). In Figure 5.6, the effective sound speed on the ground is marked by the vertical yellow lines. All sound speed values larger than the yellow line can cause refraction back to the ground. The three strongest correlation peaks in Figure 5.6a, b, and c occur in the direction from POKR to TCOL, i.e., the microbarom sources of these correlation peaks are located in the North Atlantic. The corresponding sound speed profiles show a higher effective sound speed within the first kilometer than on the ground, which allows tropospheric microbarom propagation within one kilometer altitude. This estimation agrees with the refraction altitude of 770 m (see Table 5.2) obtained from the correlation peak. Also all other profiles would allow refraction or propagation in the direction from POKR to TCOL below one kilometer altitude. For the correlation peaks at 28 November and 13 November in Figure 5.6b and c, this agrees with the estimated refraction altitudes listed in Table 5.2 of 750 m and 390 m. In Figure 5.6d – g the strongest correlation peak occurred in the opposite direction from TCOL to POKR. These refractive sound speed profiles might explain the less strong peaks in direction, i.e., in the direction from POKR to TCOL, e.g. in Figure 5.6d at +100 s at 29 January, 16:00h or in Figure 5.6e at +100 s at 5 January, around 3:00h.

In the direction from TCOL to POKR, one can expect, according to the sound speed profiles, microbarom propagation within 1.5 km altitude at all dates, except at 29 December (Figure 5.6a). At 29 December only microbarom propagation and refraction in the direction from POKR to TCOL is possible, which gives a possible explanation for the much higher correlation coefficient at 29 December than at the other dates. This clear directivity of the effective sound speed is caused by the wind, which was strong at 29 December. The strong wind at this date can also be found in the spectrogram of POKR and TCOL in Figure 5.2. The possible microbarom propagation in the direction from TCOL to POKR in Figure 5.6b and c could explain the much weaker correlation peaks occurring around −100 s, e.g., at 28 November, 12:00h – 21:00h.

The crosscorrelations in Figure 5.6d – g show a correlation peak in the direction from TCOL to POKR, i.e., the microbarom sources are located in the North Pacific. The sound speed profiles allow microbarom propagation within two kilometer altitude, with the exception of the profile in Figure 5.6f, which allows propagation below one kilometer altitude. The refraction altitudes obtained by applying the trace–velocity principle are within a reasonable range with exception of 29 January, 12:00h. At this date the celerity is much lower than any effective sound speed of the profile. This outlier may be explained by the time difference between sound speed profile (12:00h) and correlation peak (15:20h). In these three hours the atmosphere might have changed too much for a comparison between correlation peak and sound speed

profile. Next to these temporal variations, lateral variations of the atmosphere are also not accounted for, because the trace–velocity matching only applies for a stratified atmosphere without lateral changes. Also the outlier of the refraction altitude in Figure 5.6d may be caused by the lateral variations of the atmosphere. Also a deviation of the direction of arrival (DOA) from the station orientation can cause a distortion of the refraction altitude estimation, since the trace–velocity principle only applies if the station pair is oriented parallel to the DOA.

A general observation is that the microbaroms arriving from the Atlantic Ocean show a higher peak in the crosscorrelations than the microbaroms arriving from the Pacific Ocean, even though the Pacific Ocean is closer. The higher correlation peaks of the Atlantic microbaroms may explained by:

- The coherence of the wave fronts. The wave fronts of the distant Atlantic sources are probably more coherent than the wave fronts of Pacific sources. Since the Pacific sources are closer, also weaker microbaroms of the same source, but propagating on several different paths, can reach the stations, which leads to a superposition of several wave fronts.

- The scattered direction of arrival (DOA). The DOA of the closer Pacific sources is more scattered, because the source locations are scattered over a wide area (see Figure 5.11), i.e., the Pacific microbarom source is more diffuse. The simulations of delay times in the previous section also showed that the DOA of the Pacific sources is varying more that the DOA of the Atlantic sources.

5.4.2 Stratospheric crosscorrelations

As mentioned, Figure 5.8 and Figure 5.9 show that the correlation peaks are distributed rather randomly over all delay times in the period from 28 until 31 December as well as from 7 until 8 December. Also the maxima of the average in Figure 5.9 and the corresponding celerities in Table 5.3 are randomly distributed. The simulated delay times in Figure 5.12 are not consistent with correlation peaks in the crosscorrelations. The randomly scattered correlation peaks may be explained by:

- A fast variation of the direction of arrival (DOA). The fast change in time of the DOA causes a fast change of the delay time. This makes it difficult to determine a continuous delay time in the crosscorrelations. The DOA might even vary within the crosscorrelation window, which would prevent clear correlation peaks. This explanation is supported by the large variance of the simulated delay times (see Table 5.4), which indicates a high variability of the source location and the atmospheric conditions.

- A loss of coherence on the long stratospheric path between the stations. Coherence loss as a function of inter–station distance [*Mack and Flinn*, 1971] was already found in *Fricke et al.* [2014] (Chapter 4). The coherence loss is caused by sound speed scatter and angular scatter (cf. Equation 4.3). Sound speed scatter and angular scatter can result in several superimposed correlation peaks at different delay times in the same crosscorrelation. For the stratospheric path a smaller loss of coherence and thereby clearer crosscorrelation results were expected, because the stratosphere is more homogeneous than the troposphere, i.e., there are less wind turbulences in the stratosphere. A more homogeneous stratosphere does not exclude wind turbulences at the stations in the troposphere, which leads us to the next explanation.

- Too low signal–to–noise–ratios (SNR) of the stations. Since no analog noise reduction by spatial filters is applied to the sensors, the noise levels due to wind turbulence are rather high. In the numerical experiments in *Fricke et al.* [2013] (Chapter 3) it was shown that it is hardly possible to resolve the delay time from crosscorrelations, if the SNR is below 0.2. Probably the SNR between microbaroms and wind noise is lower than this value. The amplitudes of wind turbulences are usually much larger than the amplitudes of microbaroms. This explanation is consistent with the observation that in almost all spectrograms in Figure 5.2 wind turbulences can be found in the period from 28 until 31 December as well as from 7 until 8 December. Since the crosscorrelations are not normalized, the high amplitudes of wind noise cause a higher average of the whole crosscorrelation. The increased average can lead to the high correlation coefficients over all delay times in the period from 28 until 31 December and from 7 until 8 December.

5.5 Conclusions

In this chapter, it was attempted to retrieve the stratospheric paths between two receivers. Based on the interferometric principles, crosscorrelations between pairs of stations were calculated in order to obtain the delay time associated with refractions around the stratopause. As in Chapter 4 infrasonic interferometry was again successfully applied to tropospheric microbaroms. In the first stage of this study, the delay time between two stations of, respectively, the transportable USArray (TA) and the Alaskan regional array (AK) was determined by crosscorrelations. For the first time, correlation peaks of microbaroms propagating in two opposite directions were detected in the crosscorrelations, i.e., a causal (positive) delay time and a acausal (negative) delay time were detected. The orientation of the station pair (POKR – TCOL) indicates that the source areas of the microbaroms are in the Atlantic Ocean and the Pacific Ocean. It is shown that the distant Atlantic sources yield higher correlation coefficients than the closer Pacific sources. The different correlation coefficients are explained by the broader scatter of the direction of arrival (DOA) for the Pacific sources. Based on the retrieved delay times and the sound speed profiles of ECMWF, the altitudes of the tropospheric refractions are determined according to the trace–velocity principle. Differences in the modeled and observed altitudes are explained by temporal and lateral variations in the atmosphere, which is not accounted for in the modeling.

In the search for peaks in the crosscorrelations of stratospherically propagating microbaroms, the crosscorrelations between all station pairs with an inter–station distance between 149.3 km and 250.9 km were calculated. This range of distances was selected to bridge the shadow zone and allow stratospheric refractions between the stations. The analysis of the stratospheric crosscorrelations is structured in two possible scenarios. In the first scenario, it was assumed that the microbarom sources are surrounding the stations and that the delay time manifests itself as a peak at the stationary phase. The second scenario takes the varying source location and the varying atmospheric wind and temperature into account. For this purpose, the source locations and the propagation paths are simulated based on Ocean state and atmospheric conditions. With this approach the most likely delay time of the microbaroms is determined for each day of December 2014.

Neither correlation peaks are detected concentrated around the stationary phase in the first scenario, nor around the simulated delay times resolved in the second scenario. The highest correlation coefficients are scattered randomly over all delay times at days with a strong wind occurrence.

Three possible interpretations for the randomly scattered correlation peaks are given. The first explanation assumes that the DOA varies too fast to determine a continuous delay time and might even vary within a crosscorrelation window. According to the second explanation the coherence between the station pairs diminishes too much on the long stratospheric inter–station path. The third interpretation of the results explains the randomly scattered correlation peaks by a too low signal–to–noise–ratio (SNR) caused by wind turbulences at the stations. The high noise conditions near the sensors lead to an increase in the infrasonic energy measured.

The crosscorrelation are not normalized, i.e., the high amplitudes of wind noise cause a higher average of the whole crosscorrelation.

For future experiments the SNR might be increased through analog noise reduction by spatial filtering in order to improve the results of the crosscorrelations. Another recommended option is to deploy an array rather than a single station. By deploying an array, the infrasound measurements could be focused by beamforming on the interesting DOA of interest prior to crosscorrelation, i.e., a directional filter would be added to the other preprocessing steps.

6

Conclusions and outlook

6.1 Conclusions

6.1.1 Introduction

This thesis is a study about the applicability of interferometry to infrasonic ambient noise in order to probe the atmosphere, up to the stratosphere. Interferometry was successfully applied to noise fields in several other research domains, e.g., in oceanography, in seismology, and in ultrasonic applications. Haney applied interferometry to the infrasonic ambient noise field in the atmosphere in 2009 on a short range in the troposphere [*Haney*, 2009]. The infrasonic ambient noise field consists mainly of microbaroms, which are caused by the nonlinear interaction of the oceanic waves. The application of interferometry to infrasound is called infrasonic interferometry. This thesis extends the application of infrasonic interferometry to a larger scale, up to stratospheric altitudes.

6.1.2 Conclusions from Chapter 2

Chapter 2 describes the theory this thesis is based on. The theory chapter is divided in two parts. The first part describes the theory of infrasound propagation in the atmosphere and how the propagation can be implemented in a model. The model allows us to generate synthetic recordings at an arbitrary receiver location by combining a raytracer with an implementation of amplitude attenuation. Furthermore, the phase shift of the simulated recording due to caustics is taken into account. The amplitude is attenuated by geometrical spreading and by absorption of the atmosphere. In the second part of Chapter 2, the theory of interferometry is stepwise developed from a simple one–dimensional case to the application of interferometry to waves in a nonreciprocal moving medium like the atmosphere. This chapter shows that in theory infrasonic interferometry can be applied probing the atmosphere.

6.1.3 Conclusions from Chapter 3 on the feasibility

Chapter 3 verified the theory of infrasonic interferometry in numerical experiments. It was shown that infrasonic interferometry can be used to estimate the delay times between two receivers of stratospherically refracted waves. Synthetic time signals were generated by using the raytracing model and by taking into account atmospheric attenuation, geometrical spreading, phase shifts and caustics. Two types of sources were implemented for the numerical experiments: blast waves and microbaroms. An array of sources and two receivers were simulated. In the simulation the receivers were reached by eigenrays refracted at 30 km and 40 km altitude. In the first experiment with the blast wave, it became possible to estimate the delay time between the receivers of the 30 km refraction. The delay time of the second refraction was found less clearly, probably because the velocity gradient at 40 km altitude was less strong. In the experiment with microbaroms, the delay time of the first arrival was recovered as well, but the delay time of the second raypath could not be detected, for the same reason. The results might be improved by including more sources. Nevertheless, the delay time of the 30 km refraction can be well estimated above a signal–to–noise–ratio of 0.5 using infrasonic interferometry. The numerical experiments verified that microbaroms can be used in practice to obtain the delay times of infrasound propagating through the stratosphere. It depends on the wind and temperature profile which parts of the stratosphere are sampled.

6.1.4 Conclusions from Chapter 4 on the tropospheric application

In Chapter 4 infrasonic interferometry was successfully applied to measured microbaroms. The delay time of the microbaroms between two stations is determined through cross correlating the corresponding recordings. This calculation for all 55 station pairs of the "Large Aperture Infrasound Array" (LAIA, situated in the north of the Netherlands) gives the delay time of microbaroms up to a distance of 40.6 km, i.e., on a direct path the infrasonic wave of the microbaroms is coherent up to this distance. The derived delay times were used to estimate the direction of arrival (DOA), which corresponds to the known microbarom sources in the north Atlantic Ocean. The study of the influence of the station orientation on the coherence showed that the coherence between station pairs oriented parallel to the DOA is higher than the coherence of those oriented orthogonal to the DOA. By curve fitting of the coherence, the sound speed scatter ($\Delta c = \pm 5.9\,\mathrm{m/s}$) and the scatter of the direction of arrival ($\Delta\theta = \pm 1.7°$) were determined. These results extend *Mack and Flinn* [1971]'s results to higher frequencies around 0.2 Hz. The scattering of the sound speed lies within what can be assumed to be the range of sound speed variations caused by moderate winds of a few meters per second.

By comparing the change of the wind speed with the crosscorrelation strength as a function of time, it was shown that in the data set a strong meridional wind at the ground disturbs the delay time estimation. This can be explained by the higher noise levels due to the meridional wind in this specific case. Furthermore, uncertainties in the derived wind can arise due to possible refractions, instead of direct paths.

Not only the meridional wind variations were compared with the results of the crosscorrelations, but also the changes of zonal wind and temperature were compared. The comparison shows that the infrasound propagation over the array is correlated to tropospheric temperature and wind. There is no correlation between the changes of stratospheric conditions and the changes of the crosscorrelation peaks. These results indicate that the microbaroms propagated in the troposphere over the array.

Based on the crosscorrelation peaks between three closest stations as a function of time, we are able to estimate the effective sound speed and the wind speed as a function of time. Hence, Chapter 4 proved that infrasonic interferometry can be applied to tropospherically propagating microbaroms in probing the lower atmosphere.

■ 6.1.5 Conclusions from Chapter 5 on the stratospheric application

In Chapter 5 it is attempted to retrieve the stratospheric paths between two receivers. Based on the interferometric principles, crosscorrelations between pairs of sensors were calculated in order to obtain the delay time associated with refractions around the stratopause. As in Chapter 4 infrasonic interferometry was again successfully applied to tropospheric microbaroms. In the first stage of this study, the delay time between two stations of the transportable USArray (TA) and the Alaskan regional array (AK) was determined by crosscorrelations. For the first time, correlation peaks of microbaroms propagating in two opposite directions were detected in the crosscorrelations, i.e., a causal (positive) delay time and a acausal (negative) delay time were detected. The orientation of the station pair (POKR – TCOL) indicates that the source areas of the microbaroms are in the Atlantic Ocean and the Pacific Ocean. It is shown that the distant Atlantic sources yield higher correlation coefficients than the nearby Pacific sources. The different correlation coefficients are explained by the broader scatter of the direction of arrival (DOA) for the Pacific sources. Based on the retrieved delay times and the sound speed profiles of ECMWF (European Centre for Medium–Range Weather Forecasts), the altitudes of the tropospheric refractions are determined according to the trace–velocity principle. Differences in the modeled and observed altitudes are explained by temporal and lateral variations in the atmosphere, which is not accounted for in the modeling.

In the search for peaks in the crosscorrelations of stratospherically propagating microbaroms, the crosscorrelations between all station pairs with an inter–station distance between 149.3 km and 250.9 km were calculated. This range of distances was selected to bridge the shadow zone and allows stratospheric refractions between the stations. The analysis of the stratospheric crosscorrelations is structured in two possible scenarios. In the first scenario, it was assumed that the microbarom sources are surrounding the stations and that the delay time manifests itself as a peak at the stationary phase. The second scenario takes the varying source location and the varying atmospheric wind and temperature into account. For this purpose, the source locations and the propagation paths are simulated, based on ocean state and atmospheric conditions. With this approach the most likely delay time of the microbaroms is determined for each day of December 2014.

Neither correlation peaks are detected concentrated around the stationary phase in the first scenario, nor around the simulated delay times resolved in the second scenario. The highest correlation coefficients are scattered randomly over all delay times at days with a strong wind occurrence.

Three possible interpretations for the randomly scattered correlation peaks are given. The first explanation assumes that the DOA varies too fast to determine a continuous delay time and might even vary within a crosscorrelation window. According to the second explanation the coherence between the station pairs diminishes too much on the long stratospheric inter–station path. The third interpretation of the results explains the randomly scattered correlation peaks by a too low signal–to–noise–ratio (SNR) due to wind turbulences at the stations. The high noise conditions near the sensors lead to an increase in the infrasonic energy measured.

6.2 Outlook

This thesis applies infrasonic interferometry to microbaroms propagating through troposphere and stratosphere. Since it is the first study on stratospherically refracted microbaroms, there remains a lot of room for further research in this field. The successful application of infrasonic interferometry to stratospherically propagating microbaroms remains a challenge for the future. The tropospheric application of infrasonic interferometry was successfully realized in this thesis, but also in the tropospheric application still a lot of room for extensive research remains.

The preprocessing of the infrasound recordings appeared to be the essential measure to improve the quality of the crosscorrelations. The preprocessing of the recorded ambient noise aims at focusing on the microbaroms.

There are digital and analog measures to enhance the signal–to–noise–ratio SNR of the microbaroms. The first part of the outlook focuses on the improvement of the SNR.

The measures to improve the SNR are applicable to the stratospheric and to the tropospheric remote sensing. The second part of the outlook discusses the potentials of further tropospheric applications of infrasonic interferometry.

■ 6.2.1 Improvement of the signal–to–noise–ratio

There are several infrasonic signals, which can distort the microbaroms of interest. The main causes of the disturbing signals are other infrasound sources, wind and turbulence. The infrasound sources, which are not of interest often arrive from another direction than the microbaroms of interest. In order to separate the interesting microbaroms from unwanted sources arriving from other directions, we propose to deploy arrays. Arrays with an aperture of around one kilometer can focus on certain incident angles by beamforming, i.e., an array allows for directional filtering which suppresses unwanted sources from other directions. This way it becomes possible to crosscorrelate only the bundle of beams which point in the direction of interest.

The deployment of arrays is already well established in ambient noise interferometry of the oceans [*Leroy et al.*, 2012; *Carrière et al.*, 2014], which is also a fast

varying medium like the atmosphere.

Another measure to increase the SNR is the analog noise reduction with acoustic filters like porous hoses or pipe arrays. In the tropospheric studies in Chapter 4 the analog noise reduction of LAIA sufficiently suppressed distortions caused by wind turbulences, but in the stratospheric studies no analog noise reduction was applied to the sensors of the transportable USArray. For the application of infrasonic interferometry to stratospherically propagating microbaroms this measure will improve the results of the crosscorrelations.

6.2.2 Tropospheric applications of infrasonic interferometry

The tropospheric studies in Chapter 4 and Chapter 5 show that the coherence of infrasonic waves remains sufficiently high for infrasonic interferometry over distances of tens of kilometers. In Chapter 4, we showed that infrasonic interferometry works for the troposphere. The tropospheric remote sensing with infrasonic interferometry has a high temporal and spatial resolution. The temporal resolution of infrasonic interferometry is limited by the window length of the crosscorrelations and the spatial resolution is limited by the inter–station distance. Therefore, infrasonic interferometry offers a very useful addition to existing tropospheric observation methods.

The tropospheric remote sensing, described in Chapter 4 of this thesis, determines the absolute strength of the wind vector between three stations. In the future this approach can be extended and include more stations. This way it becomes possible to apply acoustic tomography of the troposphere in order to retrieve wind and temperature. In further studies non–acoustic phenomena like turbulences, gravity waves and convection can be quantified. Such studies can contribute to the understanding of processes in the atmospheric boundary layer. The stability of the boundary layer plays an important role in weather and climate models. Gravity waves are often parameterized in a model. Infrasonic remote sensing can give actual observation of this gravity wave activity.

A

List of Symbols and Abbreviations

A.1 Symbols

The symbols used in this thesis are alphabetically listed. Greek symbols are listed under the first letter of the transcription.

Symbol	Unit	Explanation
$\otimes$	–	Correlation
$*$	–	Convolution
α_{abs}	–	Atmospheric absorption coefficient of the total loss
α_{cl}	–	Atmospheric absorption coefficient of the viscosity loss
α_{dif}	–	Atmospheric absorption coefficient of the diffusion loss
$\alpha_{max,i}$	–	Maximum loss per wavelength from
α_{rot}	–	Atmospheric absorption coefficient of the rotational loss
α_{vb}	–	Atmospheric absorption coefficient of the vibrational relaxation loss vibrational relaxation of molecule species ($i = O_2$, N_2, etc)
$A_{\mathbf{x}}$	m^2	Surface spanned by a spreading ray at the location $\mathbf{x}$

Symbol	Unit	Explanation
β_{spr}	–	Coefficient which describes the geometrical spreading
χ_i	–	Molar fraction of i: concentration of molecular species ($i = O_2$, N_2, etc)
c	m/s	Speed of sound
c_c	m/s	Celerity, the celerity is calculated by dividing the distance between a station pair by the delay time of the particular correlation peak.
c_{ef}	m/s	Effective speed of sound, the effective sound speed takes the wind $\vec{u}$ into account: $c_{ef} = c_T + \hat{n} \cdot \vec{u}$
c_T	m/s	Adiabatic speed of sound, $c_T = \sqrt{\gamma_g RT}$
Δc	m/s	Sound speed scatter, also referred to as velocity scatter
$C(t)$	–	Crosscorrelation coefficient
C_i	J/K	Relaxing specific heat for the gas $i = O_2$, N_2, etc
CO_2	–	Carbon dioxide
C_P	J/K	Specific heat at constant pressure
$C_{P,\infty}$	J/K	Specific heat at constant pressure at frequencies above the vibrational relaxation effects
C_V	J/K	Specific heat at constant volume
$C_{V,\infty}$	J/K	Specific heat at constant volume at frequencies above the vibrational relaxation effects
δ	–	Dirac impulse
$\frac{\partial}{\partial t}$	1/s	Partial derivative, in this case with respect to t
D	m/s	Jacobian equation along the raypath
f	Hz	Frequency
$f_{vb,i}$	Hz	Vibrational relaxation frequency

Symbol	Unit	Explanation
		of molecule species ($i = O_2$, N_2, etc)
γ	–	Ratio of specific heats $\gamma = \frac{C_P}{C_V}$
$G(\mathbf{x}_B, \mathbf{x}_A)$	–	Green's function from location $\mathbf{x_A}$ to location $\mathbf{x_B}$, it is an impulse response at $\mathbf{x_B}$ to an impulsive source at $\mathbf{x_A}$
j		Complex number $j = \sqrt{-1}$
$\varkappa$	–	Modified non-dimensional frequency
κ	1/Pa	Compressibility of the medium $\kappa = \frac{1}{\rho c^2}$
λ	m	Wavelength
Δ	$1/m^2$	Laplace operator $\Delta = \nabla^2$
μ	kg/ms	(Dynamic) viscosity
μ_0	kg/ms	Reference viscosity at the ground for a temperature of $T_0 = 293.15\,\mathrm{K}$ ($20°C$)
M_0	kg/kmol	Molecular weight
∇	1/m	Nabla operator for all spatial derivatives $\nabla = \left(\frac{\partial}{\partial x}, \frac{\partial}{\partial y}, \frac{\partial}{\partial z}\right)$
ν	–	Non–dimensional frequency
N	–	Autocorrelation
N_2	–	Nitrogen
$\hat{n}$	–	Normal vector of the wave front, parallel to slowness vector $\vec{s}$
n_k		Component k of the normal vector $\hat{n}$
ω	1/s	Angular frequency $\omega = 2\pi f$
O_2	–	Oxygen
O_3	–	Ozon
ϕ	–	Elevation angle
p	$\mathrm{Pa} = \mathrm{kg/ms^2}$	Pressure

Symbol	Unit	Explanation
p_b	$\mathrm{Pa} = \mathrm{kg/ms^2}$	Atmospheric background pressure
p_r	$\mathrm{Pa} = \mathrm{kg/ms^2}$	Reference pressure at the ground for a temperature of $T_0 = 293.15\,\mathrm{K}$ $(20°C)$
π	–	Pi $\pi = 3.14...$
q	$1/\mathrm{s}$	Distribution of sources
ρ	$\mathrm{kg/m^3}$	Density of the medium
ρ_0	$\mathrm{kg/m^3}$	Density of the medium at the ground
R_s	$\mathrm{J/kg\,K}$	Specific gas constant
R_u	$\mathrm{J/mol\,K}$	Universal gas constant $R_u = \frac{R_s}{M_0} = 8.314\,510\,\mathrm{J/mol\,K}$
σ	–	σ characterizes the structure of the gas due to the ratio $\sigma = \frac{c_\infty}{c_0} = \frac{5}{\sqrt{21}}$
$S(t)$	Pa	Source wavelet
$S_N(t)$	Pa	Noise source
$\vec{s}$	s/m	Slowness vector, $\vec{s} = \begin{pmatrix} s_x \\ s_y \\ s_z \end{pmatrix}$
$\vec{s}_0$	s/m	Initial slowness vector at the source, $\vec{s}_0 = \begin{pmatrix} s_{x,0} \\ s_{y,0} \\ s_{z,0} \end{pmatrix}$
τ	s	Travel time of the wave front
θ		Azimuth angle
$\Delta\theta$		Azimuth angle
T	K	Temperature
T_0	K	Reference temperature $T_0 = 293.15\,\mathrm{K}$ $(20°C)$
t	s	Time
t_A,t_B	s	Travel time to receiver A respectively receiver B
$\vec{u}$	m/s	Wind vector, $\vec{u} = \begin{pmatrix} u_x \\ u_y \\ u_z \end{pmatrix}$
$\vec{u}_0$	m/s	Initial wind vector, $\vec{u}_0 = \begin{pmatrix} u_{x,0} \\ u_{y,0} \\ u_{z,0} \end{pmatrix}$
$\vec{v}$	m/s	Particle velocity, $\vec{v} = \begin{pmatrix} v_x \\ v_y \\ v_z \end{pmatrix}$
$\mathbf{x}$	m	Spatial coordinates, $\mathbf{x} = (x, y, z)$

Symbol	Unit	Explanation
$\mathbf{x}_0$	m	Initial coordinates, usually $\mathbf{x}_0 = (0, 0, 0)$
$\mathbf{x}_A$,$\mathbf{x}_B$	m	Spatial coordinates of receiver A respectively of receiver B
Z_{rot}		Rotational collision number of air

A.2 Abbreviations

Abbrivation	Explanation
2DFD	Two–Dimensional Wave Spectra
ANSI	American National Standards Institute
CTBT	Comprehensive Nuclear–Test–Ban Treaty
CTBTO	Comprehensive Nuclear–Test–Ban Treaty Organization
DOA	Direction Of Arrival
DTS	Deterministic Transient Signal
ECMWF	European Centre for Medium–Range Weather Forecasts
ECMWF HRES	High spatial Resolution atmospheric model of ECMWF
EOF	Empirical Orthogonal Functions
IRIS	Incorporated Research Institutions for Seismology
ISO	International Organization for Standardization
KNMI	Royal Netherlands Meteorological Institute
LAIA	Large Apertur Infrasound Array
LOFAR	LOw Frequency ARray
NOAA	National Oceanic and Atmospheric Administration
NRLMSISE–00	Naval Research Laboratory Mass Spectrometer and Incoherent Scatter radar Exosphere
NWO	Nederlandse Organisatie voor Wetenschappelijk Onderzoek
PTBT	Partial Test Ban Treaty
RMS	Root mean square
SNR	Signal–to–Noise–Ratio
WAM	Wave Atmosphere Model of ECMWF

B

Appendix Absorption

In Chapter 2 the absorption of infrasound by the atmosphere is described. All parameters, which were not explained in Chapter 2, are discussed in this appendix.

The air consists mostly of oxygen and nitrogen, therefore the rotational collision number of air Z_{rot} is calculated by using the rotational collision number of nitrogen $Z_{rot,\mathrm{N_2}}$ and oxygen $Z_{rot,\mathrm{O_2}}$:

$$Z_{rot} = \frac{1}{\frac{\chi_{\mathrm{N_2}}}{Z_{rot,\mathrm{N_2}}} + \frac{\chi_{\mathrm{O_2}}}{Z_{rot,\mathrm{O_2}}}}, \tag{B.1}$$

where $\chi_{\mathrm{N_2}}$ and $\chi_{\mathrm{O_2}}$ are the altitude dependent mole fractions of nitrogen and oxygen, which we obtain from NRLMSISE-00 (Naval Research Laboratory Mass Spectrometer and Incoherent Scatter Radar exosphere) [*Picone et al.*, 2002]. NRLMSISE-00 is an empirical model of the atmosphere from the ground to lower exosphere (0 km to 1000 km). The rotational collision number of nitrogen $Z_{rot,\mathrm{N_2}}$ and oxygen $Z_{rot,\mathrm{O_2}}$ depend on the temperature:

$$Z_{rot,\mathrm{N_2}} = 63.3e^{-16.7T^{-1/3}}, \tag{B.2a}$$

$$Z_{rot,\mathrm{O_2}} = 54.1e^{-17.3T^{-1/3}}. \tag{B.2b}$$

In the classical absorption (Equation 2.18a), σ characterizes the structure of the gas as the ratio of the speed of sound c at infinite frequency to that at zero frequency:

$$\sigma = \frac{c_\infty}{c_0} = \sqrt{\frac{\gamma_\infty}{\gamma_0}} = \sqrt{\frac{C_{p,\infty}/C_{V,\infty}}{C_{p,0}/C_{V,0}}} = \frac{5}{\sqrt{21}}, \tag{B.3}$$

where the index ∞ denotes a frequency well above the rotational relaxation frequency, the index 0 denotes a frequency well below rotational relaxation frequency, C_p is the specific heat at constant pressure, and C_V is the specific heat at constant volume. We assumed the following values $C_{p,\infty} = (5/2)\, R_u$, $C_{V,\infty} = (3/2)\, R_u$, $C_{p,0} = (7/2)\, R_u$, and $C_{V,0} = (5/2)\, R_u$ (cf. Table B.1), where R_u is the universal gas constant.

The rotational absorption α_{rot} (Eq. 2.18b) depends on the same parameters as the classical absorption α_{cl} (Eq. 2.18a), but contains additionally the mole fractions of oxygen χ_{O_2} and nitrogen χ_{N_2} in an additional parameter.

$$\chi_{O,N} = \frac{\chi_{O_2} + \chi_{N_2}}{0.9903}, \tag{B.4}$$

where 0.9903 is the sum of the mole fractions for oxygen $\chi_{O_2}(z = 0)$ and nitrogen $\chi_{N_2}(z = 0)$ at sea level (cf. Table B.1).

The vibrational relaxation loss α_{vb} in Equation 2.18d depends on the maximum loss per wave length $\alpha_{max,i}$, and the vibration frequency $f_{vb,i}$. The i in index indicates molecular components oxygen O_2, nitrogen N_2, carbon dioxide CO_2, and ozone O_3 of the atmosphere. The maximum loss per wave length $\alpha_{max,i}$ is calculated using:

$$\alpha_{max,i} = \chi_i(z = 0)\, \frac{\pi}{2} \frac{\frac{C_i}{R_u}}{\frac{C_{p,\infty}}{R_u}\left(\frac{C_{V,\infty}}{R_u} + \frac{C_i}{R_u}\right)}, \tag{B.5}$$

where $R_u = 8314.48\,\mathrm{J/kmol}$ is the universal gas constant, χ_i is the mole fraction of the ith atmospheric component at sea level $z = 0$ (cf. Table B.1). C_i is the relaxing specific heat and is given by:

$$\frac{C_i}{R_u} = \left(\frac{T_{vb,i}}{T}\right)^2 \frac{e^{-(T_{vb,i}/T)}}{\left(1 - e^{-(T_{vb,i}/T)}\right)^2}, \tag{B.6}$$

where $T_{vb,i}$ is the characteristic temperature of the atmospheric component. The characteristic temperature $T_{vb,i}$, the mole fraction χ_i at sea level, the normalized

specific heats $C_{p,\infty}$, and $C_{V,\infty}$ are listed in Table B.1.

Component i	$\frac{C_{V,\infty}}{R_u}$	$\frac{C_{p,\infty}}{R_u}$	$T_{vb,i}$(K)	$\chi_i(z=0)$
O_2	5/2	7/2	2239.1	0.209 48
N_2	5/2	7/2	3352	0.780 84
CO_2	3	4	915	$2 \times 0.000\,314$
O_3	3	4	1037	$< 10^{-19}$

Table B.1: *Parameters for the atmospheric main components to calculate the maximum loss per wave length (Eq. B.5) at the vibrational relaxation frequencies (Eq. B.7). $C_{V,\infty}/R_u$ is the normalized specific heat at constant volume, $C_{p,\infty}/R_u$ is the normalized specific heat at constant pressure, $T_{vb,i}$ is the characteristic temperature, and $\chi_i(z=0)$ are the mole fractions of the atmospheric components at sea level. The mole fraction χ_{CO_2} of CO_2 is multiplied by two to account for the double degeneracy of its two orthogonal vibration modes [Sutherland and Bass, 2004].*

The maximum loss per wave length $\alpha_{max,i}$ occurs at the molecular vibration relaxation frequency $f_{vb,i}$ in Equation 2.18d. The vibrational relaxation frequency is estimated by a variation of the ANSI standard [*ISO*, 1993]:

$$\begin{aligned} f_{vb,\mathrm{O_2}} &= \frac{p}{p_0}\frac{\mu_0}{\mu}\Bigg(\left[\chi_{\mathrm{O_2}}+\chi_{\mathrm{N_2}}\right] 24\, e^{-9.16\,T_c} + \left[\chi_{\mathrm{O}}+\chi_{\mathrm{N}}\right] 2400 \\ &\quad + 40\,400\, e^{10\,T_c}\, 100\left[\chi_{\mathrm{H_2O}}+\chi_{\mathrm{O_3}}\right] \\ &\quad \times \left[0.02\, e^{-11.2\,T_c} + 100\,\left(\chi_{\mathrm{H_2O}}+\chi_{\mathrm{O_3}}\right)\right] \\ &\quad \times \left[0.391\, e^{8.41\,T_c} + 100\,\left(\chi_{\mathrm{H_2O}}+\chi_{\mathrm{O_3}}\right)\right]\Bigg), \end{aligned} \tag{B.7a}$$

$$f_{vb,\mathrm{N_2}} = \frac{p}{p_0}\frac{\mu_0}{\mu}\left(9\, e^{-19.9\,T_c} + 60\,000\,\chi_{\mathrm{O_3}} + 28\,000\, e^{-4.17\,T_c}\,\chi_{\mathrm{H_2O}}\right), \tag{B.7b}$$

$$\begin{aligned} f_{vb,\mathrm{CO_2}} &= \frac{p}{p_0}\frac{\mu_0}{\mu}\Bigg(22\,000\, e^{-7.68\,T_c}\,\chi_{\mathrm{CO_2}} + 15\,100\, e^{-10.4\,T_c}\left[\chi_{\mathrm{O_2}}+0.5\chi_{\mathrm{O}}\right] \\ &\quad + 11\,500\, e^{-9.17\,T_c}\left[\chi_{\mathrm{N_2}}+0.5\chi_{\mathrm{N}}\right] \\ &\quad + 8.48\times 10^8\, e^{9.17\,T_c}\left[\chi_{\mathrm{H_2O}}+\chi_{\mathrm{O_3}}\right]\Bigg), \end{aligned} \tag{B.7c}$$

$$f_{vb,\mathrm{O_3}} = \frac{p}{p_0}\frac{\mu_0}{\mu}\left(1.2\times 10^5\, e^{-7.72\,T_c}\right), \tag{B.7d}$$

where $\times$ denotes a multiplication, $T_c = \left[(T/293.15\mathrm{K})^{-1/3}-1\right]$ is a temperature correction factor at a reference temperature of 293.15 Kelvin (20°C), the reference viscosity $\mu_0 = 18.192\times 10^{-6}\,\mathrm{kg/ms}$ is also obtained at 293.15 Kelvin. $\chi(z)$ are the mole fraction dependent on the altitude: $\chi_{\mathrm{O_2}}$ of oxygen, $\chi_{\mathrm{N_2}}$ of nitrogen, χ_{O} of atomic oxygen, χ_{N} of atomic nitrogen, $\chi_{\mathrm{H_2O}}$ of water vapor, $\chi_{\mathrm{O_3}}$ of ozone, $\chi_{\mathrm{CO_2}}$ of carbon dioxide.

As mentioned below Equation B.1, the mole fractions of oxygen and nitrogen were obtained from the NRLMSISE-00 model. The altitude dependent mole fractions of the other components are calculated according to the generic equation:

$$\chi_i \;=\; 10^{\,a_0 + a_1\, z + a_2\, z^2 + a_3\, z^3 + a_4\, z^4 + a_5\, z^5} \tag{B.8}$$

where z is the altitude, the coefficients a_0, a_1, a_2, a_3, a_4, and a_5, are obtained from *Sutherland and Bass* [2004] Table III.

Bibliography

Antier, K., A. Le Pichon, S. Vergniolle, C. Zielinski, and M. Lardy (2007), Multiyear validation of the NRL-G2S wind fields using infrasound from Yasur, *J. Geophys. Res.*, *112*, D23110.

Assink, J. D., R. Waxler, and D. Drob (2012), On the sensitivity of infrasonic traveltimes in the equatorial region to the atmospheric tides, *J. Geophys. Res.*, *117*, D01110.

Assink, J. D., R. Waxler, W. G. Frazier, and J. Lonzaga (2013), The estimation of upper atmospheric wind model updates from infrasound data, *J. Geophys. Res.*, *118*, 10,707–10,724.

Assink, J. D., R. Waxler, P. Smets, and L. G. Evers (2014), Bidirectional infrasonic ducts associated with sudden stratospheric warming events, *J. Geophys. Res.*, *119*, 1140–1153.

Baker, W. E. (1973), *Explosions in air*, University of Texas Press, Austin, TX.

Bedard, A. J., and T. M. Georges (2000), Atmospheric Infrasound, *Physics Today*, *53*, 32–37.

Benioff, H., and B. Gutenberg (1939), Waves and currents recorded by electromagnetic barographs, *Bull. Am. Meteorol. Soc.*, *20*, 412–426.

Bensen, G. D., M. H. Ritzwoller, M. P. Barmin, A. L. Levshin, F. Lin, M. P. Moschetti, N. M. Shapiro, and Y. Yang (2007), Processing seismic ambient noise

data to obtain reliable broad-band surface wave dispersion measurements, *Geophys. J. Int.*, *169*, 1239–1260.

Blom, P., and R. Waxler (2012), Impulse propagation in the nocturnal boundary layer: Analysis of the geometric component, *J. Acoust. Soc. Am.*, *131*, 3680–3690.

Brekhovskikh, L. M., and O. Godin (2010), *Acoustics of layered media II: point sources and bounded beams*, Springer, Berlin.

Brekhovskikh, L. M., V. V. Goncharov, V. M. Kurtepov, and K. A. Naugolnykh (1973), The radiation of infrasound into the atmosphere by surface waves in the ocean, *Izvestiya, Atmos. Oceanic Phys.*, *9*, 899–907.

Carrière, O., P. Gerstoft, and W. S. Hodgkiss (2014), Spatial filtering in ambient noise interferometry, *J. Acoust. Soc. Am.*, *135*, 1186–1196.

Cole, S. P. (1995), Passive seismic and drill-bit experiments using 2-D arrays, Ph.D. thesis, Stanford University.

Cowling, D. H., H. D. Webb, and K. C. Yeh (1971), Group rays of internal gravity waves in a wind-stratified atmosphere, *J. Geophys. Res.*, *76*, 213–220.

Crescenti, G. H. (1997), A look back on two decades of doppler sodar comparison studies, *Bull. Am. Meteor. Soc.*, *78*, 651–673.

Dahlman, O., S. Mykkeltveit, and H. Haak (2009), *Nuclear test ban: converting political visions to reality*, 2009 ed., Springer, Dodrecht.

de Groot-Hedlin, C. D., and M. A. H. Hedlin (2015), A method for detecting and locating geophysical events using groups of arrays, *Geophys. J. Int.*, *203*, 960–971.

Dessa, J. X., J. Virieux, and S. Lambotte (2005), Infrasound modeling in a spherical heterogeneous atmosphere, *Geophys. Res. Lett.*, *32*, L12808.

Donn, W. L., and B. Naini (1973), Sea wave origin of microbaroms and microseisms, *J. Geophys. Res.*, *78*, 4482–4488.

Donn, W. L., and D. Rind (1971), Natural infrasound as an atmospheric probe, *Geophys. J. R. Astr. Soc.*, *26*, 111–133.

Donn, W. L., and D. H. Rind (1972), Microbaroms and the temperature and wind of the upper atmosphere, *J. Atmos. Sci.*, *29*, 156–172.

Donn, W. L., and D. M. Shaw (1967), Exploring the atmosphere with nuclear explosions, *Rev. Geophys.*, *5*, 53–82.

Draganov, D., K. Wapenaar, W. Mulder, J. Singer, and A. Verdel (2007), Retrieval of reflections from seismic background-noise measurements, *Geophys. Res. Lett.*, *34*, L04305.

Drob, D. P., R. R. Meier, J. M. Picone, and M. M. Garcés (2010), Inversion of infrasound signals for passive atmospheric remote sensing, in *Infrasound Monitoring for Atmospheric Studies*, pp. 701–731, Springer Netherlands, Dordrecht.

Drob, D. P., D. Broutman, M. A. Hedlin, N. W. Winslow, and R. G. Gibson (2013), A method for specifying atmospheric gravity wavefields for long-range infrasound propagation calculations, *J. Geophys. Res.*, *118*, 3933–3943.

Evers, L. G., and H. W. Haak (2001), Listening to sounds from an exploding meteor and oceanic waves, *Geophys. Res. Lett.*, *28*, 41–44.

Evers, L. G., and H. W. Haak (2005), The detectability of infrasound in The Netherlands from the Italian volcano Mt. Etna, *J. Atmos. Sol.-Terr. Phys.*, *67*, 259–268.

Evers, L. G., and H. W. Haak (2007), Infrasonic forerunners: Exceptionally fast acoustic phases, *Geophys. Res. Lett.*, *34*, L10806.

Evers, L. G., and P. Siegmund (2009), Infrasonic signature of the 2009 major sudden stratospheric warming, *Geophys. Res. Lett.*, *36*, L23808.

Evers, L. G., A. R. J. van Geyt, P. Smets, and J. T. Fricke (2012), Anomalous infrasound propagation in a hot stratosphere and the existence of extremely small shadow zones, *J. Geophys. Res.*, *117*, D06120.

Fricke, J. T., N. E. Allouche, D. G. Simons, E. N. Ruigrok, K. Wapenaar, and L. G. Evers (2013), Infrasonic interferometry of stratospherically refracted microbaroms —A numerical study, *J. Acoust. Soc. Am.*, *134*, 2660–2668.

Fricke, J. T., L. G. Evers, P. S. M. Smets, K. Wapenaar, and D. G. Simons (2014), Infrasonic interferometry applied to microbaroms observed at the Large Aperture Infrasound Array in the Netherlands, *J. Geophys. Res.*, *119*, 9654–9665.

Georges, T. M. (1971), *A program for calculating three-dimensional acoustic-gravity ray paths in the atmosphere*, National Oceanic and Atmospheric Administration, Boulder, CO.

Georges, T. M. (1972), 3D ray tracing for acoustic-gravity waves, *J. Acoust. Soc. Am.*, *51*, 147.

Gilmore, R. (1993), *Catastrophe theory for scientists and engineers*, Dover Publications, Dover.

Godin, O. (2006), Recovering the acoustic green's function from ambient noise cross correlation in an inhomogeneous moving medium, *Phys. Rev. Lett.*, *97*, 054301.

Godin, O. A., V. G. Irisov, and M. I. Charnotskii (2014), Passive acoustic measurements of wind velocity and sound speed in air, *J. Acoust. Soc. Am.*, *135*, EL68–EL74.

Gossard, E. E., and W. H. Hooke (1975), *Waves in the atmosphere: Atmospheric infrasound and gravity waves - Their generation and propagation*, *Developments in Atmospheric Science*, Elsevier Scientific Pub. Co., Amsterdam.

Green, D. N., R. S. Matoza, J. Vergoz, and A. Le Pichon (2012), Infrasonic propagation from the 2010 Eyjafjallajökull eruption: Investigating the influence of stratospheric solar tides, *J. Geophys. Res.*, *117*, D21202.

Gutenberg, B. (1939), The velocity of sound waves and the temperature in the stratosphere above Southern California, *Bull. Am. Meteorol. Soc.*, *20*, 192–201.

Haak, H., and L. G. Evers (2002), Infrasound as a tool for CTBT verification, in *Verification yearbook 2002*, edited by T. Findlay and Trevor, pp. 207–221, Verification Research, Training and Information Centre (VERTIC).

Haney, M. M. (2009), Infrasonic ambient noise interferometry from correlations of microbaroms, *Geophys. Res. Lett.*, *36*, L19808.

Hariharan, P. (2012), *Basics of interferometry*, 2 ed., Academic Press, Amsterdam.

Hasselmann, K. (1963), A statistical analysis of the generation of microseisms, *Rev. Geophys.*, *1*, 177–210.

Haubrich, R. A. (1968), Array design, *Bull. Seism. Soc. Am.*, *58*, 977–991.

Havelock, D. I., S. Kuwano, and M. Vorländer (2008), *Handbook of signal processing in acoustics*, 1 ed., Springer, New York.

Hedlin, M. A. H., M. A. Garcés, H. Bass, C. Hayward, G. Herrin, J. Olson, and C. Wilson (2002), Listening to the secret sounds of earth's atmosphere, *Eos Trans. AGU*, *83*, 557–565.

Holton, J. R. (2004), *An introduction to dynamic meteorology*, Academic Press, London.

ISO (1993), 9613–1: 1993. Acoustics. Attenuation of sound during propagation outdoors. Part 1: Calculation of the absorption of sound by the atmosphere, *International Organization for Standardization, Geneva*.

Johnson, J. B., J. Anderson, O. Marcillo, and S. Arrowsmith (2012), Probing local wind and temperature structure using infrasound from Volcan Villarrica (Chile), *J. Geophys. Res.*, *117*, D17107.

Jones, R., J. P. Riley, and T. M. Georges (1986), HARPA: A versatile three-dimensional Hamiltonian ray-tracing program for acoustic waves in the atmosphere above irregular terrain, special report, National Oceanic and Atmospheric Administration, Boulder, CO, pp. 1–410.

Kedar, S., M. Longuet-Higgins, F. Webb, N. Graham, R. Clayton, and C. Jones (2008), The origin of deep ocean microseisms in the North Atlantic Ocean, *Proc. R. Soc. A*, *464*, 777–793.

Kornhauser, E. T. (1953), Ray theory for moving fluids, *J. Acoust. Soc. Am.*, *25*, 945–949.

Kulichkov, S. N., K. V. Avilov, G. A. Bush, O. E. Popov, O. M. Raspopov, A. K. Baryshnikov, D. R. Velle, and R. W. Whitaker (2004), On anomalously fast infrasonic arrivals at long distances from surface explosions, *Izvestiya, Atmos. Oceanic Phys.*, *40*, 1–9.

Lagarias, J., J. Reeds, M. Wright, and P. Wright (1998), Convergence properties of the Nelder–Mead simplex method in low dimensions, *SIAM J. Optim.*, *9*, 112–147.

Lalande, J.-M., O. Sèbe, M. Landès, P. Blanc-Benon, R. S. Matoza, A. Le Pichon, and E. Blanc (2012), Infrasound data inversion for atmospheric sounding, *Geophys. J. Int.*, *190*, 687–701.

Le Pichon, A., E. Blanc, and D. Drob (2005), Probing high-altitude winds using infrasound, *J. Geophys. Res.*, *110*, D20104.

Leroy, C., S. Lani, K. G. Sabra, W. S. Hodgkiss, W. A. Kuperman, and P. Roux (2012), Enhancing the emergence rate of coherent wavefronts from ocean ambient noise correlations using spatio-temporal filters, *J. Acoust. Soc. Am.*, *132*, 883.

Lindemann, F. A., and G. Dobson (1923), A theory of meteors, and the density and temperature of the outer atmosphere to which it leads, in *Proc. R. Soc. London*, *102*, 411–437.

Lingevitch, J. F., M. D. Collins, D. K. Dacol, D. P. Drob, J. C. W. Rogers, and W. L. Siegmann (2002), A wide angle and high Mach number parabolic equation, *J. Acoust. Soc. Am.*, *111*, 729–734.

Longuet-Higgins, M. S. (1950), A theory of the origin of microseisms, *Phil. Trans. R. Soc. of London*, *243*, 1–35.

Mack, H., and E. A. Flinn (1971), Analysis of the spatial coherence of short-period acoustic-gravity waves in the atmosphere, *Geophys. J. R. Astr. Soc.*, *26*, 255–269.

Marcillo, O., and J. B. Johnson (2010), Tracking near-surface atmospheric conditions using an infrasound network, *J. Acoust. Soc. Am.*, *128*, EL14–EL19.

Mentink, J. H., and L. G. Evers (2011), Frequency response and design parameters for differential microbarometers, *J. Acoust. Soc. Am.*, *130*, 33–41.

Nelder, J. A., and R. Mead (1965), A simplex method for function minimization, *The Computer Journal*, *7*, 308–313.

NOAA, NASA, and USAF (1976), *U.S. standard atmosphere*, 1st ed., U.S. Government Printing Office, Washington D.C.

Picone, J. M., A. E. Hedin, and D. P. Drob (2002), NRLMSISE-00 empirical model of the atmosphere: Statistical comparisons and scientific issues, *J. Geophys. Res.*, *107*, 1–16.

Pierce, A. D. (1989), *Acoustics: An Introduction to its Physical Principles and Applications*, Acoustical Society of America, Melville, USA.

Posmentier, E. S. (1967), A theory of microbaroms, *Geophys. J. R. Astr. Soc.*, *13*, 487–501.

Posmentier, E. S., and W. L. Donn (1969), Probing the atmosphere with infrasound, in *National Academy of Sciences - National Research Council; Panel on Remote Atmospheric Probing*, pp. 681–691, Lamont Geological Observatory Columbia University.

Reynolds, O. (1873), On the refraction of sound by the atmosphere, *Proc. Roy. Soc. London*, *22*, 531–548.

Reynolds, O. (1876), On the refraction of sound by the atmosphere, *Phil. Trans. R. Soc. London*, *166*, 315–324.

Rickett, J., and J. Claerbout (1999), Acoustic daylight imaging via spectral factorization: Helioseismology and reservoir monitoring, *The Leading Edge*, *18*, 957–960.

Rind, D. (1979), Probing the atmosphere with infrasound, *Phys. Teach.*, *17*, 102–108.

Rind, D. H., and W. L. Donn (1978), Infrasound observations of variability during stratospheric warmings, *J. Atmos. Sci.*, *35*, 546–553.

Roux, P., W. A. Kuperman, and t. N. Group (2004), Extracting coherent wave fronts from acoustic ambient noise in the ocean, *J. Acoust. Soc. Am.*, *116*, 1995–2003.

Ruigrok, E., X. Campman, D. Draganov, and K. Wapenaar (2010), High-resolution lithospheric imaging with seismic interferometry, *Geophys. J. Int.*, *183*, 339–357.

Sabra, K. G., P. Gerstoft, P. Roux, W. A. Kuperman, and M. C. Fehler (2005), Extracting time-domain Green's function estimates from ambient seismic noise, *Geophys. Res. Lett.*, *32*, L03310.

Shapiro, N. M., and M. Campillo (2004), Emergence of broadband Rayleigh waves from correlations of the ambient seismic noise, *Geophys. Res. Lett.*, *31*, L07614.

Shaw, W. N., and W. H. Dines (1904), The study of the minor fluctuations of atmospheric pressure, *Q. J. R. Meteorol. Soc.*, *31*, 39–52.

Smets, P. S. M., and L. G. Evers (2014), The life cycle of a sudden stratospheric warming from infrasonic ambient noise observations, *J. Geophys. Res.*, D021905.

Stopa, J. E., K. F. Cheung, M. A. Garcés, and N. Badger (2012), Atmospheric infrasound from nonlinear wave interactions during hurricanes Felicia and Neki of 2009, *J. Geophys. Res.*, *117*, C12017.

Sutherland, L. C., and H. E. Bass (2004), Atmospheric absorption in the atmosphere up to 160 km, *J. Acoust. Soc. Am.*, *115*, 1012–1032.

Symons, G. J. (1888), *The eruption of Krakatoa and subsequent phenomena*, Trübner & Co, London.

Thompson, R. J. (1972), Ray theory for an inhomogeneous moving medium, *J. Acoust. Soc. Am.*, *51*, 1675–1682.

van Haarlem, M. P., et al. (2013), LOFAR: The LOw-Frequency ARray, *Astronomy and Astrophysics*, *556*, 1–56.

Virieux, J., N. Garnier, E. Blanc, and J. X. Dessa (2004), Paraxial ray tracing for atmospheric wave propagation, *Geophys. Res. Lett.*, *31*, L20106.

Walker, K. T. (2012), Evaluating the opposing wave interaction hypothesis for the generation of microbaroms in the eastern North Pacific, *J. Geophys. Res.*, *117*, C12016.

Wapenaar, K. (2006), Nonreciprocal Green's function retrieval by cross correlation, *J. Acoust. Soc. Am.*, *120*, EL7–EL13.

Wapenaar, K., and J. Fokkema (2004), Reciprocity theorems for diffusion, flow, and waves, *J. Appl. Mech.*, *71*, 145–150.

Wapenaar, K., and J. Fokkema (2006), Green's function representations for seismic interferometry, *Geophysics*, *71*, SI33–SI46.

Wapenaar, K., D. Draganov, R. Snieder, X. Campman, and A. Verdel (2010), Tutorial on seismic interferometry: part 1 — basic principles and applications, *Geophysics*, *75*, 195–209.

Waxler, R., and K. E. Gilbert (2006), The radiation of atmospheric microbaroms by ocean waves, *J. Acoust. Soc. Am.*, *119*, 2651–2664.

Waxler, R., K. E. Gilbert, C. L. Talmadge, and C. Hetzer (2007), The effects of finite depth of the ocean on microbarom signals, in *8th International Conference on Theoretical and Computational Acoustics (ICTCA)*, Crete, Greece.

Weaver, R., and O. Lobkis (2001), Ultrasonics without a source: thermal fluctuation correlations at MHz frequencies, *Phys. Rev. Lett.*, *87*, 134301.

Wessel, P., and W. Smith (1991), Free software helps map and display data, *Eos Trans. AGU*, *72*, 441–446.

Whipple, F. J. W. (1923), The high temperature of the upper atmosphere as an explanation of zones of audibility, *Nature*, *111*, 187.

Whipple, F. J. W. (1930), The great Siberian meteor and the waves, seismic and arial, which it produced, *Q. J. R. Meteorol. Soc.*, *56*, 287–304.

Williams, C. R. (1997), Principal component analysis of wind profiler observations, *J. Atmos. Oceanic Technol.*, *14*, 386–395.

Summary

There is a rich world of sound humans are unable to hear, because the frequency is too low. This sound with a frequency below 20 Hz is called infrasound. Ever since the propagation of sound through the atmosphere was studied, a strong dependency on the temperature and wind structure of the atmosphere was observed. Infrasound propagates over distances of hundred to thousand kilometers and each crossed atmospheric layer leaves a certain signature in the infrasonic signal. If this signature can be extracted in an inversion process, the temperature and wind structure of the atmosphere might be revealed. Most of current studies, which use infrasound to remote–sense the atmospheric wind and temperature, rely on deterministic transient signals (DTS). However, DTS have a crucial disadvantage. Events with a known source time and location are rare. Infrasound sensors continuously measure ambient noise. For a long time, this ambient noise was considered as a disturbance and thus neglected. The ambient noise consists mostly of microbaroms. Microbaroms are almost continuously radiated from nonlinear interactions of oceanic waves and typically occur around 0.2 Hz.

In this thesis, the possibilities of infrasonic interferometry for probing the troposphere and stratosphere with microbaroms are explored. Infrasonic interferometry determines the delay time between two sensors by cross correlating their infrasound recordings. The obtained delay time can be used to estimate the Green's function, which is the impulse response of the medium. Until now this approach was applied in other research fields, e.g., oceanography, seismology and ultrasonics, but it was used only occasionally for infrasound studies. In this thesis, the new research field

of infrasonic interferometry is explored from the theoretical basics, via numerical experiments with synthetic data, up to the application to tropospheric and stratospheric microbaroms.

In the theory section, the propagation of infrasound through the medium atmosphere is discussed and how interferometry can be tailored for this moving medium. The infrasound propagation is implemented in a model, which can generate synthetic infrasound recordings by taking into account the geometrical spreading, the absorption and the phase shift due to the atmosphere. According to the theory, infrasonic interferometry applied to atmospheric microbaroms is possible.

Further, the feasibility of infrasonic interferometry is studied in numerical experiments, i.e., interferometry is applied to synthetic recordings. Synthetic recordings are generated by the described model and then crosscorrelated. The numerical experiments show that the infrasonic interferometry can resolve propagation paths through the atmosphere and the corresponding delay times.

After the application to synthetic microbaroms, the next step is the application of infrasonic interferometry to measured microbaroms. The microbaroms are measured using the "Large Aperture Infrasound Array" (LAIA), which has been installed in the Netherlands. By calculating the crosscorrelations between all 55 station pairs of LAIA, the delay times of microbaroms up to an inter–station distance of tens of kilometers can be found. The derived delay times are used to estimate the direction of arrival (DOA). It is also shown that the coherence between station pairs oriented parallel to the DOA is higher than the coherence of those oriented orthogonal to the DOA. Based on the crosscorrelation peaks it is possible to estimate the changes of the tropospheric effective sound speed and the wind speed with time.

After having successfully applied infrasonic interferometry to tropospheric microbaroms, the next step is the application to stratospheric microbaroms. For this purpose, the inter-station distance needs to exceed at least 150 km in order to bridge the shadow zone. Therefore, infrasonic interferometry is applied to microbaroms, which are measured by the transportable USArray and by the Alaskan regional array. In the stratospheric experiments it is not possible to estimate a clear delay time of the microbaroms, because the highest crosscorrelations are scattered over all delay times. Despite the lack of clear stratospheric crosscorrelations, also the stratospheric experiments give new insights. In preparation of the stratospheric experiments, also tropospheric microbaroms are crosscorrelated. These crosscorrelations show for the first time microbaroms arriving from two opposite directions.

Overall, we can state that infrasonic interferometry has been successfully applied

to tropospherically propagating microbaroms. The estimation of stratospheric wind and temperature by using stratospheric microbaroms remains a feasible challenge for the future.

In all experiments with measured microbaroms, the increase of the SNR of the microbaroms appears to be an essential step. For the future, it is proposed to improve the SNR by analog and digital measures. Furthermore, infrasonic interferometry applied to tropospheric microbaroms offers a very useful addition to existing tropospheric observation methods. Therefore an extension of this approach is proposed.

Samenvatting

Er is een wereld van geluiden die wij mensen niet kunnen horen, want ze hebben te lage frequenties. Dit geluid met een frequentie lager dan 20 Hz wordt infrageluid genoemd. Uit historisch onderzoek naar de voortplanting van het geluid in de atmosfeer is gebleken dat de geluidsvoortplanting sterk afhankelijkheid is van de temperatuur– en de windstructuur in de atmosfeer. Infrageluid plant zich voort over honderden tot duizenden kilometers en elke doorkruiste atmosferische laag laat zijn specifieke signatuur in het infrageluid signaal achter. Dit suggereert dat infrageluid mogelijk gebruikt kan worden om informatie over wind en temperatuur te achterhalen via een inversie procedure. Eerdere studies aangaande dit onderwerp zijn gebaseerd op het gebruik van kortdurende signalen (Deterministic Transient Signal, DTS). Echter, DTS hebben cruciale nadelen. Events met een bekende exacte bronlocatie en tijd zijn zeldzaam. Daarentegen, infrageluid sensoren meten permanent het achtergrondruis, dat lange tijd als een verstoring werd beschouwd en dus genegeerd werd. Het achtergrondruis bestaat voornamelijk uit zogenaamde microbaromen. Microbaromen worden veroorzaakt door niet-lineaire interacties van oceaangolven en hebben een frequentie van 0,2 Hz.

In dit proefschrift worden de mogelijkheden van infrasone interferometrie onderzocht voor het sonderen van de troposfeer en de stratosfeer, met gebruik van microbaromen. In het proces van infrasone interferometrie wordt de vertragingstijd van een signaal tussen twee sensoren bepaald, door een kruiscorrelatie van de metingen. Met behulp van de verkregen vertragingstijd kan de Greense functie, d.w.z. de impulsrespons van het medium, geschat worden. Tot nu toe is deze aanpak alleen

gebruikt in andere gebieden van de wetenschap, bijvoorbeeld in oceanografie, seismologie en ultrageluid, maar het is nog niet veel toegepast op infrageluid. In dit proefschrift wordt het nieuwe onderzoeksterrein van infrasone interferometrie onderzocht vanuit de theoretische basis, via numerieke experimenten met synthetische data, tot de toepassing op troposferische en de stratosferische microbaromen.

In het theoriegedeelte wordt de voortplanting van infrageluid door de atmosfeer, het medium, behandeld en hoe interferometrie kan worden aangepast voor dit bewegende medium. Infrageluid voortplanting wordt geïmplementeerd in een model, dat synthetische infrageluid data kan genereren. Hierbij wordt rekening houden met de geometrische spreiding, de geluidsabsorptie en de faseverschuiving door de atmosfeer. Volgens de theorie is het mogelijk infrasone interferometrie op atmosferische microbaromen toe te passen.

Daarnaast wordt de haalbaarheid van infrasone interferometrie in numerieke experimenten onderzocht, d.w.z. interferometrie wordt toegepast op synthetische opnamen. De synthetische opnamen worden gegenereerd door het beschreven model en worden vervolgend gekruiscorreleerd. De numerieke experimenten tonen aan dat de infrasone interferometrie het propagatie pad door de atmosfeer en de bijbehorende vertragingstijd kan oplossen.

Na de toepassing op synthetische microbaromen, is de volgende stap de toepassing van infrasone interferometrie op gemeten microbaromen. De microbaromen worden gemeten met behulp van het "Large Aperture Infrasound Array" (LAIA), dat in Nederland is geïnstalleerd. Door de kruiscorrelatie te berekenen tussen de stationsparen is het mogelijk om de vertragingstijd te bepalen. Dit blijkt mogelijk met stationsparen die onderling tot op enkele tientallen kilometers uit elkaar staan. De afgeleide vertragingstijden worden gebruikt om de richting van aankomst (direction of arrival, DOA) te schatten. Ook wordt aangetoond dat de coherentie tussen stationsparen die parallel georiënteerd zijn met de DOA hoger is dan de coherentie tussen de paren die loodrecht georiënteerd staan op de DOA. Op basis van de kruiscorrelatie maxima is het mogelijk om de temporele veranderingen van de effectieve geluidssnelheid en de windsnelheid in de troposfeer te schatten.

Vervolgens wordt de techniek op stratosferische microbaromen toegepast. De afstand tussen stationsparen moet ten minste 150 km bedragen om de schaduwzone van stratosferische propagatie te overbruggen. Daarom wordt infrasone interferometrie toegepast op microbaromen die door het mobiele USArray en het Alaskan regional array worden gemeten. In de stratosferische experimenten bleek het niet mogelijk een duidelijke vertragingstijd van de microbaromen te schatten.

De maxima van de kruiscorrelaties zijn te variabel over de mogelijke vertragingstijden. Ondanks het ontbreken van duidelijke stratosferische kruis correlaties, geven de stratosferische experimenten toch nieuwe inzichten. Ter voorbereiding van de stratosferische experimenten, worden ook troposferische microbaromen gekruiscorreleerd. Deze kruiscorrelaties tonen voor de eerste keer microbaromen van twee tegengestelde invalsrichtingen aan.

Over het algemeen kunnen we stellen dat infrasone interferometrie met succes is toegepast op troposferisch propagerende microbaromen. De schatting van de stratosferische wind en de temperatuur met behulp van de stratosferische microbaromen blijft een wetenschappelijke uitdaging voor de toekomst. Uit dit promotieonderzoek is gebleken dat de signaal-ruis verhouding (SNR) van de gemeten microbaromen een essentiële factor is. Suggesties voor zowel de analoge als digitale verbetering van de SNR worden geopperd. Verder blijkt uit dit onderzoek dat interferometrie een zeer nuttige toevoeging is voor observaties in de troposfeer.

Zusammenfassung

Es gibt eine Welt voller Geräusche, die wir Menschen nicht hören können, weil sie zu tiefe Frequenzen haben. Diese Geräusche mit einer Frequenz unterhalb von 20 Hz werden als Infraschall bezeichnet. Seit die Ausbreitung von Schall in der Atmosphäre untersucht wird, zeigte sich eine starke Abhängigkeit der Schallausbreitung von der Temperatur– und Wind–Struktur der Atmosphäre. Infraschall breitet sich über Hunderte bis Tausende von Kilometern aus und jede dabei durchquerte Atmosphärenschicht hinterlässt ihre spezifische Signatur im Infraschall–Signal. Könnte diese Signatur in einem Inversionsverfahren entschlüsselt werden, so wäre es möglich, mit Infraschall die Temperatur– und Wind–Struktur der Atmosphäre zu erkunden. Nahezu alle gegenwärtigen Studien, die Infraschall zur Fernerkundung von Wind und Temperatur verwenden, sind auf deterministische transiente Signale (DTS) angewiesen. DTS haben jedoch einen entscheidenden Nachteile: Ereignisse, deren Ursprungs–Ort und Zeitpunkt genau bekannt sind, sind sehr selten. Infraschall–Sensoren messen kontinuierlich das Hintergrundrauschen, das lange Zeit als Störung angesehen und deswegen nicht beachtet wurde. Das Hintergrundrauschen besteht vor allem aus sogenannten Mikrobaromen. Mikrobarome entstehen durch nichtlineare Interaktionen von Ozeanwellen und haben eine Frequenz um 0,2 Hz.

In dieser Doktorarbeit werden die Möglichkeiten der Infraschall–Interferometrie zur Fernerkundung der Troposphäre und der Stratosphäre mit Hilfe von Mikrobaromen untersucht. Infraschall–Interferometrie bestimmt die Verzögerungszeit zwischen zwei Sensoren durch Kreuzkorrelation ihrer Infraschall–Aufzeichungen. Mit Hilfe dieser Verzögerungszeit kann die Greensche Funktion, also die Impulsantwort

des Mediums bestimmt werden. Bisher wurde dieser Ansatz nur in anderen Wissenschaftsbereichen eingesetzt, beispielsweise in der Ozeanographie, der Seismologie und im Ultraschall, aber nur gelegentlich im Bereich von Infraschall. In dieser Doktorarbeit wird der neuartige Ansatz der Infraschall–Interferometrie von den theoretischen Grundlagen, über numerische Experimente mit synthetischen Daten bis zur Anwendung auf troposphärischer und stratosphärischer Mikrobarome untersucht.

Im Theorieteil wird die Ausbreitung von Infraschall im Medium Atmosphäre diskutiert und untersucht, wie Interferometrie auf dieses bewegte Medium maßgeschneidert werden kann. Die Infraschall–Ausbreitung wird in einem Modell implementiert, welches synthetische Infraschall–Aufzeichnungen unter Berücksichtigung von geometrischer Streuung, von Absorption und von Phasenlage generieren kann. Folgt man der Theorie, so ist es möglich Infraschall–Interferometrie auf atmosphärische Mikrobarome anzuwenden.

Des Weiteren werden die Möglichkeiten und Grenzen von Infraschall–Interferometrie in numerischen Studien untersucht, d.h., Infraschall–Interferometrie wird auf synthetische Aufzeichnungen angewandt. Die synthetischen Aufzeichnungen werden durch das beschriebene Modell generiert und dann kreuzkorreliert. Die numerischen Experimente zeigen, dass Infraschall–Interferometrie den Ausbreitungsweg von Infraschall durch die Atmosphäre ermitteln kann.

Nach der Anwendung von Infraschall–Interferometrie auf synthetische Mikrobarome ist der nächste Schritt die Anwendung auf gemessene Mikrobarome. Die Mikrobarome wurden mit dem "Large Aperture Infrasound Array" (LAIA) gemessen, das im Norden der Niederlande installiert wurde. Durch die Berechnung von Kreuzkorrelationen zwischen allen 55 Stationspaaren von LAIA kann die Verzögerungszeit der Mikrobarome bis zu einem Stationsabstand im zweistelligen Kilometerbereich bestimmt werden. Diese Verzögerungszeiten werden verwendet um die Einfallsrichtung (direction of arrival, DOA) zu ermitteln. Zudem wird gezeigt, dass die Kohärenz zwischen Stationspaaren parallel zur Einfallsrichtung höher ist als zwischen Stationspaaren im rechten Winkel zur Einfallsrichtung. Basierend auf den Maximalwerten der Kreuzkorrelationen ist es möglich, die effektive Schallgeschwindigkeit und Windstärke in der Troposphäre abhängig von der Zeit zu schätzen.

Nach der erfolgreichen Anwendung der Infraschall–Interferometrie auf troposphärische Mikrobarome, ist der nächste Schritt die Anwendung auf stratosphärische Mikrobarome. Zu diesem Zweck muss der Abstand zwischen den Sensoren größer als 150 km sein, um die akustische Schattenzone zu überbrücken. Aus diesem

Grund wird die Infraschall–Interferometrie auf Mikrobarome angewandt, die von dem mobilen USArray und von dem Alaskan regional array gemessen wurden. Aus den stratosphärischen Experimenten konnte keine eindeutige Verzögerungszeit der Mikrobarome ermittelt werden, da die Maximalwerte der Kreuzkorrelationen über alle Verzögerungszeiten verteilt sind.

Trotz Fehlens eindeutiger stratosphärischer Kreuzkorrelationen, geben auch diese Experimente neue Einblicke. In Vorbereitung der stratosphärischen Experimente wurden auch troposphärische Mikrobarome kreuzkorreliert. Diese Kreuzkorrelationen zeigen zum ersten mal Mikrobarome aus zwei entgegengesetzten Einfallsrichtungen.

Im Allgemeinen lässt sich festhalten, dass die Infraschall–Interferometrie im Rahmen dieser Arbeit erfolgreich auf sich troposphärisch ausbreitende Mikrobarome angewandt wurde. Die Bestimmung von stratosphärischem Wind und Temperatur bleiben auch in Zukunft eine realistische Herausforderungen.

In allen Experimenten mit gemessenen Mikrobaromen stellte sich ein hohes Signal–zu–Rausch–Verhältnis (SNR) als entscheidender Faktor heraus. Für die Zukunft empfiehlt es sich daher das SNR durch analoge und digitale Maßnahmen zu vergrößern. Die troposphärische Anwendung von Infraschall–Interferometrie bietet eine nützliche Ergänzung zu den existierenden Observationsmethoden in der Troposphäre. Aus diesem Grund empfiehlt sich weitere Forschung in diesem Bereich.

Curriculum Vitae

Julius Tobias Fricke was born in Lemgo, Germany on 25 October 1976. He attended secondary school at the Rudolf Steiner school in Detmold, where he received the general qualification for university entrance in 1996. In 1997, he started the study of Media technology at the Ilmenau University of Technology (TU Ilmenau), Germany. He specialized in Audio and Visual Techniques and received his diploma thesis in 2009. His diploma thesis in Media technology was prepared in collaboration with Microflown Technologies in Arnhem on source localization using particle velocity probes and pressure receivers (Untersuchung von Quellenlokalisationsverfahren unter Nutzung von Schnelle– und Druckempfängern).

At the end of 2009, Julius began his doctoral research on infrasonic interferometry in the department Seismology and Acoustics of the Royal Netherlands Meteorological Institute (KNMI) in cooperation with the Delft University of Technology (TU Delft). At the Delft University of Technology Julius carried out his research in the section Aircraft Noise and Climate Effects of the faculty of Aerospace Engineering and in the section Applied Geophysics and Petrophysics of the faculty Civil Engineering and Geoscience.

Peer–reviewed publications

[3] **Fricke, J.T.**, L.G. Evers, P.S.M. Smets, K. Wapenaar, D.G. Simons (2014), *Infrasonic interferometry applied to microbaroms observed at the Large Aperture Infrasound Array in the Netherlands*, J. Geophys. Res., 119, 9654–9665.

[2] **Fricke, J.T**., N.E. Allouche, D.G. Simons, E.N. Ruigrok, K. Wapenaar, and L.G. Evers (2013), *Infrasonic interferometry of stratospherically refracted microbaroms —A numerical study*, J. Acoust. Soc. Am., 134, 2660–2668.

[1] Evers, L.G., A.R.J. Van Geyt, P. Smets, and **J.T. Fricke** (2012), *Anomalous infrasound propagation in a hot stratosphere and the existence of extremely small shadow zones*, J. Geophys. Res., 117, D06120.

Conferences

[15] **J. Fricke**, L. Evers, K. Wapenaar, and D. Simons (2013), *Interferometry applied to the large aperture infrasound array in the Netherlands*, J. Acoust. Soc. Am., 134, 4224–4224

[14] **Fricke, J.T.**, L.G. Evers, E. Ruigrok, K. Wapenaar, and D.G. Simons (2013), *Infrasonic interferometry applied to synthetic and measured data*, European Geoscience Union, General Assembly 2013, Vienna, Austria.

[13] **Fricke, J.T.**, E.N. Ruigrok, L.G. Evers, N. El Allouche, D. Simons, and C.A. Wapenaar (2012), *Infrasound interferometry for active and passive sources: a synthetic example for waves refracted in the stratosphere*, American Geophysical Union, Fall Meeting 2012, San Francisco, USA.

[12] **Fricke, J.T.**, E.N. Ruigrok, L.G. Evers, D.G. Simons, and K. Wapenaar (2012), *Results of infrasound interferometry in Netherlands*, European Geoscience Union, General Assembly 2012, Vienna, Austria.

[11] Smets, P., Evers L.G., A. Van Geyt, and **J. Fricke** (2012), *Anomalous infrasound propagation in a hot stratosphere and the existence of extremely small shadow zones*, European Geoscience Union, General Assembly 2012, Vienna, Austria.

[10] **Fricke, J.T.**, E.N. Ruigrok, L.G. Evers, D.G. Simons, K. Wapenaar (2012), *Results of infrasound interferometry in Netherlands*, Nederlands Aardwetenschappelijk Congres (NAC11) 2012, Veldhoven, The Netherlands.

[9] Evers L.G., A. Van Geyt, P. Smets, and **J. Fricke** (2011), *Stratospheric returns from explosions*, American Geophysical Union, Fall Meeting 2011, San Francisco, USA.

[8] **Fricke, J.T.**, E. Ruigrok, L.G. Evers, D.G. Simons, and K. Wapenaar (2011), *The first results of infrasound interferometry*, CTBTO Infrasound Technology Workshop 2011, Dead Sea, Jordan.

[7] **Fricke, J.**, E. Ruigrok, L. Evers, D. Simons, and K. Wapenaar (2011), *LAIA – A Large Aperture Infrasound Array for interferometric studies*, European Geoscience Union, General Assembly 2011, Vienna, Austria.

[6] Haney, M.M., L.G. Evers, and **J. Fricke** (2010), *Probing atmospheric structure with infrasonic ambient noise interferometry*, American Geophysical Union, Fall Meeting 2010, San Francisco, USA.

[5] **Fricke, J.T.**, L.G. Evers, D.G. Simons, K. Wapenaar, and P. Blom (2010), *A Large Aperture Infrasound Array in the Netherlands for interferometric studies*, CTBTO Infrasound Technology Workshop 2010, Tunis, Tunisia.

[4] **Fricke, J.**, L. Evers, D. Simons, and K. Wapenaar (2010), *A Large Aperture Infrasound Array in the Netherlands for interferometric studies*, European Geoscience Union, General Assembly 2010, Vienna, Austria.

[3] **Fricke, J.T.**, H.-E. De Bree, A. Siegel, and H.-P.. Schade (2009), *Source localization with acoustic vector sensors*, ACOUSTICS High Tatras 2009, Zvolen, Slovakia.

[2] **Fricke, J.T.**, H.-E. De Bree, and A. Siegel (2009), *Source localization with acoustic vector sensors*, Ilmenau Scientific Colloquium (IWK) 2009, Ilmenau, Germany.

[1] Schlesinger, A., **J. Fricke**, P.-N. Klink, A. Siegel, and D. De Vries (2008), *Volumetric reconstruction of sound intensity in room acoustics*, Progresses of acoustics (DAGA) 2008, Dresden, Germany

Acknowledgements

This thesis is only possible due to the support of my supervisor Läslo Evers. He always had good advice when I did not know how to continue my research. Läslo encouraged me to present my research at many interesting conferences. He always managed to motivate me with a few funny comments or encouraging words. Läslo patiently supported my writing process, by reading every single sentence. In a similar manner Kees Wapenaar supported me, who also helped as well. His clear comments, constructive feedback, and joy over new results often motivated me in my research. Furthermore, Kees checked every equation thoroughly and found all of my mistakes.

Deriving these equations, Anton van Geyt helped me a lot with his solid knowledge about physics. He helped to derive the Hamiltonian equations of the raytracer and also in other questions about mathematical problems he was of great support.

In many discussions Elmer Ruigrok helped me a lot in understanding the theory of interferometry. He also assisted me with the implementation of this theory into MATLAB coding. Also Matt Haney supported me a great deal in implementing the theory of infrasonic interferometry into code.

Dick Simons was always very helpful especially with coordinating the formalities of the Ph.D.. He supported the writing process by arranging the assistance of Nihed El Allouche. At gray dutch days Nihed understood to cheer me up with her irrepressible high spirits.

At the Royal Netherlands Meteorological Institute (KNMI) my room mate Pieter Smets supported me with his software contributions and in detailed scientific dis-

cussions. Also with Jelle Assink I had several fruitful discussion about my research.

Of course I also want to thank my family and my friends for their support. Although, I cannot list all, I want to mention the help of Clara Blad and Cornelia Blaga, who polished my english texts. When I started to compose a German summary of my Ph.D., I realized that I had forgotten a lot of the German language. At this point, Christoph Pilger, Manuel Merz and Sascha Rißmann were of great help by correcting my German phrases. Sascha Rißmann also allowed me to escape the world (and the Ph.D.) at his place in Munich, when I needed a break. At the TU Delft, my office mates Dimitrios Eleftherakis and Kerstin Siemes always managed to cheer me up.

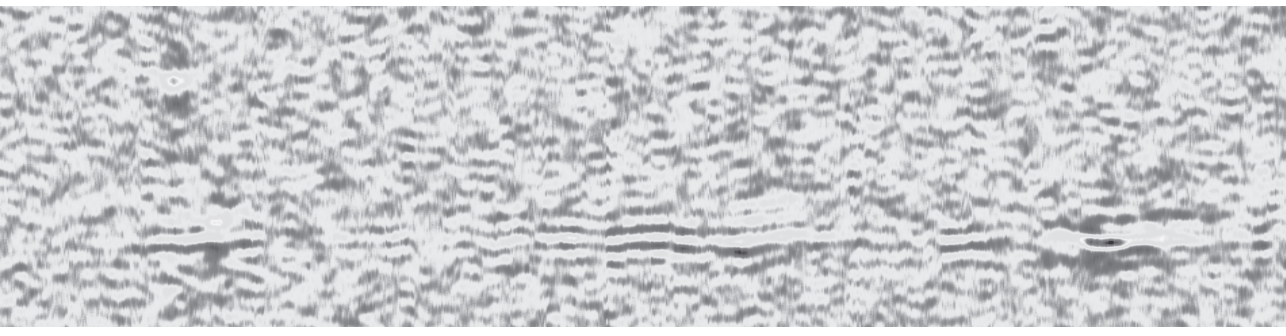
In several entertaining lunch breaks Sara Dal Gallo, Alessandro Spinuso, Jonas Matser, Iris Manola, Luca Trani, Lucinda Rasmijn, Martin Roth, and Martina Weiß prevented me from becoming obsessed or lost in details.

For my never–ending installations of the "Large Aperture Infrasound Array" (LAIA) in the framework of the radio–astronomical "LOw Frequency Array" (LOFAR), I received the support of Marchel Gerbers, Albert De Jong, and Klaas Stuurwold of Astron in Dwingeloo.

Furthermore, I express my gratitude to Alex Koers of Microflown Technologies in Arnhem. He encouraged me to come to the Netherlands and start my Ph.D. at the KNMI.

Figures 4.1, 4.5.1, 4.8, 5.1, 5.10, 5.11 of this book were made by using the Generic Mapping Tools [*Wessel and Smith*, 1991].

This thesis was funded by the Netherlands Organization for Scientific Research (NWO).



ISBN 978-94-6186-736-0